©Copyright 2014 Éder Marinho Sousa

A Blended Finite Element Method for Multi-Fluid Plasma Modeling

Éder Marinho Sousa

A dissertation submitted in partial fulfillment of the requirements for the degree of

Doctor of Philosophy

University of Washington

2014

Reading Committee:

Dr. Uri Shumlak, Chair

Dr. Settivoine You

Dr. Richard Milroy

Program Authorized to Offer Degree: Aeronautics and Astronautics

University of Washington

Abstract

A Blended Finite Element Method for Multi-Fluid Plasma Modeling

Éder Marinho Sousa

Chair of the Supervisory Committee: Professor and Acting Chair Dr. Uri Shumlak Aeronautics and Astronautics Department

In a multi-fluid plasma model electrons and ions are represented as separate fluids that interact through collisions and electromagnetic fields. The model encapsulates physics that spans a vast range of temporal and spatial scales, which renders the model stiff and consequently difficult to solve numerically. To address the large range of time scales, a blended continuous and discontinuous Galerkin method is proposed, where ions are modeled using an explicit Runge-Kutta discontinuous Galerkin method while the electrons and electromagnetic fields are modeled using an implicit continuous Galerkin method. This approach is able to capture large-gradient ion physics like shock formation, while resolving high-frequency electron dynamics in a computationally efficient manner. The convergence properties of the method are analyzed and the method is tested on an electromagnetic shock problem. The numerical method produces results comparable with current state-of-the-art finite volume and discontinuous Galerkin methods, while decreasing the computational time for cases where realistic ion-to-electron mass ratios are used, and realistic speed-of-light to thermal speed ratios are needed. The method is used to study Inertial Confinement Fusion (ICF) fuel species separation where multi-fluid effects are relevant, and the high pressure gradient experienced by the ions causes them to shock, separate, and generate large electric fields. In addition, it is shown that single-fluid plasma codes can overestimate the neutron yield in ICF. For validation purposes, simulation results are compared with experimental data. A meaningful comparison requires the quantification of uncertainties in simulations. The un-

certainties in the method are quantified using the multi-level Monte Carlo (MMC) method. The method reduces the computational cost over the standard Monte Carlo method by using multiple levels of discretization to calculate the statistical information of a given model. The MMC method is applied to the Geospace Environment Modeling (GEM) magnetic reconnection challenge problem, in which a reconnected flux is calculated for a given set of initial conditions. A reconnection flux variation envelope is provided, which provides a more rigorous approach to comparing simulation results to from different plasma models. In addition, unbounded domains necessary to allow material and fields to leave the computational domain are modeled using a combined lacuna-based open boundary conditions (LOBC) and perfectly matched layers (PML). This combined method is applied to the electromagnetic wave-pulse, and is shown to considerably reduce reflections from the boundaries. Combining this work addresses some the challenges of high-fidelity modeling of plasmas, and demonstrates the utility of novel numerical techniques that allow for simulation of experimentally-relevant physics over a large range of scales.

TABLE OF CONTENTS

		Page
List of I	Figures	. iv
List of	Γables	. ix
Chapter	1: Introduction	. 1
1.1	The Multi-Fluid Plasma Model	. 2
1.2	The Blended Finite Element Method	. 3
1.3	Inertial Confinement Fusion Fuel Species Separation	. 4
1.4	Uncertainty Quantification using the Multi-level Monte Carlo Method	. 5
1.5	Lacuna-based Open Boundary Conditions	. 6
1.6	Objective	. 6
Chapter	· 2: The Multi-Fluid Plasma Model	. 8
2.1	Introduction	
2.2	Derivation of the multi-fluid plasma model equations	
2.3	Maxwell's equations	
2.4	Normalized multi-fluid equations	
2.5	Ideal Multi-Fluid Plasma Model	
2.6	Numerical properties of the Multi-Fluid Plasma Model	
2.7	Summary	
Chapter	3: A Blended Finite Element Method	. 19
3.1	Prior and foundational work	. 19
3.2	Description of the Numerical Method	. 22
3.3	Continuous Galerkin Finite Element Method	
3.4	Discontinuous Galerkin Method	
3.5	Implicit Theta-method Time Integration	
3.6	Explicit Runge-Kutta Time Integration	
3.7	Continuous and Discontinuous Galerkin Couple Through Source Terms	

3.8	General Implementation Details	31
3.9	Summary	35
Chapter	4: Validation and Verification of the Blended Finite Element Method	36
4.1	1-D Advection Equation: Convergence Studies	36
4.2	Two-Fluid Plasma Soliton in 1-D: Accuracy and Timing Studies	38
4.3	The Electromagnetic Plasma Shock Problem	41
4.4	Summary	49
Chapter	5: Inertial Confinement Fusion Fuel Species Separation	51
5.1	$Introduction \dots \dots$	51
5.2	Planar Geometry Results	53
5.3	Spherical Geometry Results	56
5.4	Summary	65
Chapter	6: Uncertainty Quantification of the GEM Challenge Magnetic Reconnection Problem Using the Multilevel Monte Carlo Method	67
6.1	Prior and Foundational Work	67
6.2	Plasma Models for Uncertainty Quantification Study	69
6.3	Standard Monte Carlo Method	71
6.4	Multilevel Monte Carlo Method	72
6.5	Numerical Results	75
6.6	Discussion	81
6.7	Summary	84
Chapter	7: Open Boundary Conditions	85
7.1	Prior and Foundational Work	85
7.2	The Lacuna-based Open Boundary Condition (LOBC)	87
7.3	Application of the LOBCs to Maxwell Equations	90
7.4	Combined Application of PMLs and LOBCs to Maxwell's Equations	94
7.5	Summary	95
Chapter	8: Conclusion	98
8.1	Suggested Future Work	100
Diblicon	an har	101

Appendix A:	Probabilistic Collocation Method	113
Appendix B:	WARPX Description	115
Appendix C:	Species Separation Input File	117

LIST OF FIGURES

Figure Number		Page
element, and the s the derivatives in second order repre	are shown. The blue curves are the solution within each solution is continuous at element boundaries even though not. The black dots are the location of the nodes for a esentation, where adjacent element share one node. The ion of the quadrature points	. 23
ement, and the solthe location of the	are shown. The blue curves are the solution within each elution is discontinuous at element boundaries. The stars are e quadrature points. Note that the location of quadrature method coincide with the ones of the CG method	. 26
problem using a fit 5 for the CG and t 10^{-7} . The linear p	we L_2 -norm as a function of Δx for the linear advection axed time step of $\Delta t = 0.00125$ and spatial orders 3, 4, and the DG schemes. The κ value for the artificial dissipation is ortion of each line has a slope that corresponds to the order numerical method. Both methods converge as expected.	. 37
problem using a fix the DG schemes. I lines have a slope	the L_2 -norm as a function of Δx for the linear advection axed $CFL = 1$ and spatial orders 2, 3, and 4 for the CG and The κ value for the artificial dissipation is 10^{-7} . All of the of two corresponding to the temporal order of accuracy of DG section of the BFEM method	. 38
boundaries. The I are compared to a Both methods reso	tions propagate from the center of the domain towards the DG and BFEM solutions using 512 second-order elements a converged finite volume solution of 5,000 cells at $t = 40$. Elve the oscillations of the problem, but there is some phase with the BFEM	. 40
norm is lower than	the DG and the BFEM over time. The DG method error in the BFEM one, but the error is only about 1.5% of the in	. 41
1. The DG and BI	he DG and the BFEM over time for a case where $m_i/m_e =$ FEM L_2 -norms are the same because both simulations have and the electron plasma frequency is resolved	. 42

4.6	The features of the electromagnetic plasma shock are a fast rarefaction wave (FR), a slow compound wave (SC), a contact discontinuity (CD), a slow shock (SS), and another fast rarefaction wave (FR). The solution also shows fast electromagnetic waves that propagate faster than MHD waves[1]	43
4.7	The total mass density is plotted for the electromagnetic plasma shock prob- lem at $t=0.05\tau_c$. The main features of the problem are captured by all three methods, but the BFEM does not resolve the EM waves properly, which maybe due to the artificial dissipation in the method	45
4.8	The total mass density is plotted for the electromagnetic plasma shock prob- lem at $t=0.05\tau_c$. The results were obtained using different Δt . Δt_{max} corresponds to the maximum value allowed for an explicit methods and for this problem $\Delta t=42.9\Delta t_{max}$ is the maximum value allowed by the semi- implicit BFEM, where the ion dynamics restricts the time-step	46
4.9	Mass density plot comparing two cases where the electron fluid artificial dissipation, κ_e , is decreased by a factor of 10, with the DG method. The solution for the lower artificial dissipation captures the wave-like behavior better. The compound wave spikes up in amplitude, and the right rarefaction wave is not visible	48
4.10	Mass density solution comparing two BFEM cases where the electromagnetic fields artificial dissipation is decreased by a factor of 10. The reduced dissipation solution agrees better with DG solution, reinforcing the point that the wave-like behavior arises from the interaction of the electron fluid with the electromagnetic fields	48
5.1	Density plots at $t=150ps$, for two ion species for $\delta_i=1.2, c/v_o=3,065$ and $\mathrm{Kn}_i=0.8$. Z is the ionization level and μ is the ratio of the ion mass to a proton mass. Plot (b) shows the decrease in separation with an increase in the ionization level. Plot (c) is the case more relevant for ICF, and it shows that there is less separation compared to (a) and (b). In plot (d) $\mathrm{Kn}_i=0.008$ showing that for high collisionality the solution converges to a single fluid averaged atom for a $\mu=6$	55
5.2	Plot for a spherical imploding DT plasma for $c/v_o = 1120$, $\delta = 5.37 \times 10^{-3}$, $\mathrm{Kn}_i = 1.07 \times 10^{-2}$, $\mathrm{Kn}_e = 8.3 \times 10^{-3}$, and $f = 0.06$. Shown are the number density, temperature and radial electric field at $t = 1.375$ ns. As the compression evolves and the fluids approach the center the density and temperature increase. The charge separation between the ions and the electron generate radial electric fields which peak at regions of large density and temperature gradients.	57

5.3	Relative difference between the deuterium and the tritium number densities as a function of radius and time. Regions where the deuterium percentage is larger are in red, and blue where the tritium is larger. The deuterium separates from the tritium from the beginning and the separation increases as time progresses. A 0.35 ns interval separates the deuterium and the tritium shocks reaching the center.	8
5.4	(a) Plots the normalized maximum values of the deuterium pressure gradient, electric, and frictional forces for the time interval before the deuterium reaches the center of the capsule. The pressure gradient and the electric force cause the separation and are orders of magnitude larger than the frictional force which resists the separation. (b) For the same time interval the largest value of the mean free path and the corresponding Knudsen number are plotted. This shows that for the majority of the time $\mathrm{Kn} < 10^{-2}$, so a fluid description of the plasma is valid. (c) and (d) show the Kn_{dd} and Kn_{tt} respectively, and as these fluid approach the center of the imploding capsule, the deuterium-deuterium and tritium-tritium collisions decrease 6	i C
5.5	Comparison of the variables used when calculating the neutron yield for the three-fluid and two-fluid cases. Comparison of the ratio of the density product $n_d n_t$ in the three-fluid simulation with the square of the density of the two-fluid simulation. The density product for the two-fluid case is larger then the three-fluid case where the ions have separated, therefore the first term in the yield calculation is larger for the two-fluid simulation 6	15
5.6	Temperature and DT reactivity at $r=0$ for the three-fluid and two-fluid simulations are plotted over time. In the three-fluid simulation ions reach the center earlier causing an increase in the temperature and the reactivity a few nanoseconds before the two-fluid ions reach the center. Although the temperature is initially larger for the three-fluid case, after the two-fluid case reaches the center its temperature remains steadily higher 6	i 4
5.7	Maximum electric field plotted over time. The two-fluid case produces a larger peak electric field than the three-fluid simulation by a factor of two. However, gigavolt per meter electric fields produce forces that are still too small compared to the plasma pressures in the problem 6	E
6.1	L_2 -norm error for the mean and variance as a function of computational time using the quasi-neutral ion cyclotron wave test problem. With $c_s = \sqrt{1.4}$, $\omega_c = 10.0$, $B_z = 1.0$, $m_i = 1.0$ and $q = 10.0$ and initial values of $\rho = 1.0$ and $p = 1.0$. The rates of convergence for the mean using the MC and MMC methods are similar. The rate of convergence for the variance using the MMC method is faster than the MC method	~

6.2	Mean (top) and variance (bottom) of the reconnected flux for varying ion-to-electron mass ratio ranging from 25 to 100, for the MMC, MC, and PC methods.	79
6.3	Mean (top) and variance (bottom) of the reconnected flux for varying speed of light to Alfvén speed ratio ranging from 10 to 20, for the MMC, standard MC, and PC method	80
6.4	Mean (top) and variance (bottom) of the reconnected flux for varying amplitude of the magnetic flux perturbation ranging from [0.085, 0.115], for the MMC, standard MC, and PC method	81
6.5	Ion density and magnetic field vectors showing the formation of a second smaller magnetic island at the center and as a result the reconnected flux in these cases is slightly higher because there are no asymmetries in the grid and during the solution the smaller island will remain at the center of the grid. However if some numerical asymmetry develops the island will move to the right or the left. $\omega_{ci}t=38$ and $m_i/m_e=25$	82
6.6	Reconnected flux plotted versus time for different plasma models used in the GEM challenge paper [2] compared to two-fluid model. The error bars represent the uncertainty due to the sensitivity in the c/v_A as measured using the MMC method in Fig. 6.3. The Two-fluid region of certainty encompass the full particle case and most of the hybrid reconnected flux, while the Hall-MHD case is almost completely outside the region of confidence	83
7.1	Lacuna are still regions present in wave-like solutions on odd-dimension spaces.	86
7.2	The transition function $\mu(x)$ varies from zero in the interior domain to one in the exterior domain and is C_o and C_1 continuous	88
7.3	A cylindrical pulse propagates through free space, plot of the $\log B_z $. The black dashed lines show the limit of the interior domain and the purple dashed lines delimit the auxiliary domain. The top and right side boundary conditions are conducting walls. There are no reflections from the boundaries	91
7.4	Plot of $\log B_z $ at $t = 1.168$. In the ZNG there are considerably large reflections from the boundaries while the LOBC the reflections extremely small, in the other of 10^{-16}	92
7.5	The logarithm of maximum value of the magnetic field magnitude is plotted versus the elapsed simulation time. The ZNG method produces reflection when the pulse reaches the boundaries while the LOBC does not	93
7.6	A combined PML-LOBC is applied to the left boundary while a PML-only BC is used to the right boundary. The region in gray is the exterior domain of the LOBC, and both region in magenta represent the PMLs. The domain of interest is in blue with the initialization in orange. Top and bottom BCs	
	are reflecting walls.	95

7.7	Plot of $\log H_z $. Top and bottom boundary conditions are reflecting. The
	right BC is a simple PML and the left BC are a mixed PML and Lacuna.
	(a) Shows that the PML has become unstable in the right boundary, while
	at the left boundary the reintegration of the auxiliary domain has reset the
	PML, removing the instability. (b) The PML instability has contaminated
	the computational domain on the right boundary, while the left boundary
	still behaves as intended with no reflections nor instabilities
B.1	Structure of a WARPX input file for any PDE type

LIST OF TABLES

Table N	Tumber H	Page
4.1	Total computing time elapsed and time savings for a simulations using a fully DG method, compared to one using the BFEM for different values of electron-to-ion mass ratio and the speed-of-light to the ion sound speed	39
4.2	Characteristic speeds and frequencies for the electromagnetic shock problem.	47
5.1	Parameter used in Eq. (5.6) for the calculation of the DT reactivity as a function of the ions temperature[3]	61

ACKNOWLEDGMENTS

I wish to express sincere appreciation to the Aeronautics and Astronautics Department staff and faculty, and especially to my committee chair, and advisor Professor Uri Shumlak, for both financial and moral support. His guidance during the course of my graduate career has been indispensable, from helping me choose classes, to homework help, and even his help suggesting my name for my current position. I would like to thank my colleagues in the computational plasma dynamics lab, Robert Lilly, Noah Reddell, Sean Miller, Peter Norgaard, and Andrew Ho for the numerous and fruitful discussions, and for all the help they have given me through the years. A special thanks to Genia Vogman for the numerous suggestions, discussions, and thorough reviews of papers and this dissertation. I am grateful for the constant support and encouragement from my family and friends, which have made the long night and short vacations tolerable, and encouraged me to continue when there seemed to be no light at the end of the tunnel. A special thanks to my employers at the Air Force Research Lab for all the support completing this dissertation. To all my deep and sincere THANK YOU!

DEDICATION

to my dear mother Fátima, father Zeca, aunt Marina, and Step-father Stephen.

Chapter 1

INTRODUCTION

Plasma is the fourth state of matter, and is characterized as a quasi-neutral gas of charged and neutral particles that exhibit collective behavior [4]. About 99% of matter in the universe is in the state of plasma; stars, interstellar nebulae, accretion discs, solar wind, etc. Here on Earth lightning and auroras are examples of natural occurrences of plasma, while plasma displays in most living rooms in America and fluorescent light bulbs, present in almost every home, are examples of artificially produced plasmas.

Plasma can be described as a "soup" of positively charge ions and negatively charged electrons. These charged particles generate electric fields, which then produce forces on the ions and electrons. In addition, collisions between the different plasma constituents cause momentum and energy to propagate from one to another until the plasma comes to an equilibrium state. Due to the mass difference between the electrons and ions, plasmas have disparate time and spatial scales. The electron dynamics occurs on fast time scales, while ions are relatively slow to respond.

Human produced plasmas are essential parts of ion thrusters[5], Z-pinches[6], tokamaks[7], stellarators[8], and others. The operation of these devices require an extensive understanding of plasma behavior under different conditions. In the past fifty years, the development of the field of plasma physics has been guided in part by the goal of achieving an efficient means of producing nuclear fusion energy. The National Ignition Facility (NIF), for example, aims to address the challenges associated with inertial confinement fusion[9]. While efficient inertial fusion energy production is still a ways away, NIF has increased our understanding of hydrodynamic instabilities[10], mix[11], laser plasma interactions[12], kinetic effects[13], new plasma diagnostics[14], and presented new computational challenges. In the south of France, the International Thermonuclear Experimental Reactor (ITER)[15], a tokamak, is currently being built with the same goal of nuclear fusion energy production. Numerous

challenges and obstacles need to be addressed before first plasma is produced and numerous more will arise after. Simulations will continue to play an instrumental role in extending our understanding of plasma physics and will be vital to addressing the challenges of developing a viable fusion source. Experiments are extremely costly, which makes modeling crucial to aid our understanding of the physics.

1.1 The Multi-Fluid Plasma Model

In an attempt to better predict the behavior of plasmas, different computer models have been developed over the years. The most complete plasma model is an N-body problem where electrons, ions, and neutrals interact through the Lorentz forces and binary collisions. This N-body plasma model is extremely accurate and can model plasmas under any conditions, however, the model is extremely complex due to the large number of particles needed to represent a plasma, and the computational resources it requires.

Kinetic models perform an ensemble average of particle velocities to create a velocity distribution function, which describes the probability that a particle has a certain velocity at a given location in the plasma. This model is able to capture all the temporal and spatial scales of the plasma. However, the probability distribution function is dependent on three position and three velocity independent variables, which makes this model six-dimensional and computationally unattractive.

The kinetic description of a plasma can be reduced from six dimensions to three dimensions, provided that the particles that constitute the plasma are sufficiently collisional. The resulting model is the fluid model, in which each particle species is a fluid with an associated mass, momentum, and energy density [16]. The fluid model is not as general as the kinetic model in that it assumes that each species is in local thermodynamic equilibrium, though different species need not have the same thermodynamic equilibrium (e.g. ions can have a different temperature than electrons). Despite the simplifying assumption, the multi-fluid description of a plasma retains much of the physics relevant to and measured in fusion experiments.

The most widely used plasma description, the ideal magnetohydrodynamic [17] (MHD) model, represents plasma as a single fluid. This model is obtained from the multi-fluid

plasma model by neglecting the electron inertia ($m_e \to 0$), and by eliminating high frequency short-wavelength phenomena ($\epsilon_o \to 0$). Ideal MHD is valid in high collisionality and low resistivity regimes. MHD is a good model to describe large scale instabilities in devices such as Z-pinches, spheromak, and tokamak. However, when the characteristic spatial and temporal scales are small, multi-fluid effects become relevant[18], in which case the MHD description is not adequate. The multi-fluid plasma model captures non-neutral effects, which produce local electric fields, and models electron plasma waves and Debye shielding effects. The multi-fluid plasma model has a more expansive region of applicability, which might include high resistivity, large Larmor radius, or lower collisionality plasma regimes. Due to its reduced dimensionality compared to kinetic models, and its generalized physics compared to MHD, the multi-fluid model is selected as the optimal platform for investigating fusion-relevant plasma physics. Chapter 2 describes the detailed derivation of the multi-fluid model.

1.2 The Blended Finite Element Method

A two-fluid plasma model has been implemented using a high-resolution wave propagation finite volume method in Ref. [19]. The two-fluid plasma model is a special case of the multi-fluid plasma model where there is only one ion fluid and the electron fluid. Finite volume methods maintain the conservation properties of the model, and are able to resolve discontinuities with high accuracy. However, the wave propagation method has challenges capturing the high frequency oscillations of the plasma, causing phase error[20]. These oscillations are physical, not numerical, which can be difficult to resolve numerically.

In Ref. [21] the discontinuous Galerkin (DG) method is applied to the two-fluid plasma model. Like the finite volume method the DG method also retains the conservation properties of the two-fluid plasma model, and can capture shocks accurately. In addition, the DG method can produce high order spatial resolution, and can resolve high frequency oscillations without producing phase errors. The challenge of this method comes from the time integration, as the spatial order of accuracy is increased the time-step becomes very restrictive [22]. In Ref. [23], DG method is expanded to implicit time integration in an attempt to relax the time-stepping restrictions. However, due to sharp gradients and discon-

tinuities the nonlinear Jacobian matrix, needed for the implicit time integration, to become ill-conditioned and the solution often did not converge.

In most plasma applications, ions are often the only fluid that shocks, the electron and electromagnetic fields often do not. When the electrons and fields are modeled using a continuous Galerkin (CG) finite element method, the time integration can be done implicitly and the solution converges because CG methods are well behaved for implicit time integration [24]. The ion and neutral fluids can be represented using an explicit discontinuous Galerkin method. This method where the ion/neutral are advanced explicitly using a DG and the electrons and electromagnetic field are evolved implicitly using a CG method is referred to as a blended finite element method (BFEM) henceforth (Sec. 3).

The BFEM has multiple advantages for the multi-fluid plasma model (MFPM). The fast moving electrons are modeled implicitly and do not dictate restrictive time-steps, as they have the smallest mass and can move at higher speeds than the ions and neutrals. Another advantage is that, the DG and CG are both finite element methods, and as such, they provide high order spatial resolution of the plasma.

1.3 Inertial Confinement Fusion Fuel Species Separation

In Inertial Confinement Fusion (ICF) the plasma is under extremely large pressure and densities, and small spatial and temporal scales dominate the physics. Under these conditions, multi-fluid plasma effects are relevant and cannot be ignored. The temporal scales of interest are associated with the ion dynamics, but the electrons play an important role, e.g. charge separation and electric field, and heat conduction. Therefore, the MHD model in not well suited for ICF plasmas. The multi-fluid plasma model provides a more generalized description of fuel separation in ICF capsules, and in conjunction with BFEM provides a computationally efficient means of simulating the associated physics.

The more generalized physics encapsulated by the multi-fluid model can help shed light on the cause of the overestimated neutron production observed in ICF experiments. After the deuterium-tritium (DT) filled capsule has been compressed to fusion conditions, one of the diagnostics used to analyze the burn history is the neutron yield. Recent yield measurements conducted at the OMEGA facility have shown that the measured yield is about 50% less than the expected[25]. It is believed that this discrepancy is due to the DT fuel separation caused by the generation of large electric fields, on the order of GV/m.

ICF simulations are done using radiation-hydrodynamic codes that assume a single charge-neutral average-mass DT fluid[10]. This model is incapable of producing fuel separation. Additionally the charge-neutral assumption does not allow for charge separation effects that cause local electric fields. The MFPM does not have these assumption, which makes it an ideal candidate for this problem. In Chapter 5 the MFPM using the BFEM is used to study the effects of ICF fuel separation on the neutron yield.

1.4 Uncertainty Quantification using the Multi-level Monte Carlo Method

To verify computer simulations, numerical results have to be compared to experimental data. For a rigorous comparison, it is important to account for the numerous sources of uncertainty in simulations, which include: assumptions made in the derivation of the model, accuracy of numerical methods, boundary condition implementation, initial condition implementations, numerical constants, etc. Treating all the parameters as stochastic is computationally expensive, which points to the necessity to develop different sensitivity analysis methods to rank the importance of the random inputs and their interactions [26].

The standard most well know method to quantify uncertainty is the Monte Carlo method[27], but this method is slow to converge and requires a large number of simulations. The Multilevel Monte Carlo (MMC) method, developed in Ref. [26] for use in computational finance, on the other hand converges much faster. The MMC method reduces the computational complexity through the use of a multilevel approach that combines results obtained using different levels of discretization.

The MMC method uses a geometric sequence of time-steps similar to the multi-grid method and has proven to be efficient and reliable in achieving the desired accuracy. This permits establishment of regions of confidence in simulations which can subsequently be compared to experimental results. The MMC method shows promising results when it comes to accuracy and computational cost[28]. See Chapter 6 for the implementation.

1.5 Lacuna-based Open Boundary Conditions

Simulating open boundary conditions has always been challenging. Nonetheless, numerous problems from aerodynamics, to plasmas, to astrophysics, require the numerical approximation of far fields. Whenever open boundary domains are truncated to a finite computational domain, special care is needed when implementing boundary conditions, otherwise waves propagating outwards are reflected into the computational domain creating non-physical conditions.

In Chapter 7, the lacuna-based open boundary conditions [29] (LOBC) is implemented. Lacuna is a region in space that, after being disturbed by a traveling wave, has returned to its original condition and any change to a traveling wave does not affect its lacuna. This method is combined the perfectly matched layer [30] (PML) method to solve the problem of PMLs becoming unstable for long running simulations [31]. Combining both methods allow for the LOBC to be more efficient and less computationally expensive.

1.6 Objective

The objective of this dissertation is to develop a multi-fluid plasma framework that can be applied to problems where there are plasmas composed of multiple ion and neutral species, and the electron dynamics are relevant. The framework is applicable in problems where there is high collisionality within each species, and there is local thermodynamical equilibrium.

A blended finite element method is developed to numerically represent the multi-fluid plasma model. The BFEM is conservative, high order accurate, can resolve shock and high frequency oscillations, and eliminates the most stringent time-step limitations imposed by explicit methods.

The BFEM is applied to the ICF capsule fuel species separation problem, in which multi-fluid effects are relevant and which is of extreme importance to ICF research. To allow for rigorous comparison between simulation and experiments, an uncertainty quantification analysis is developed and demonstrated to work on the well-studied problem of magnetic reconnection. Boundary conditions, such as those relevant in ICF, that involve

the propagation of signals out of the simulated domain require special treatment. A means of handling such boundaries is developed so as to avoid spurious unphysical reflections of signals. Together the described numerical methods and techniques extend the present capabilities of fluid plasma simulations, and the scope of physics that can be captured with fluid models.

Chapter 2

THE MULTI-FLUID PLASMA MODEL

2.1 Introduction

Developments in plasma physics have been propelled by the necessity to better understand phenomena relevant to the study stellar structures, effects of the solar wind on the earth's magnetosphere, fusion energy research, space propulsion, etc. over the years. As such, numerous plasma models have been developed.

Kinetic models represent the velocity probability distribution function in phase space, and time, $f(\mathbf{x}, \mathbf{v}, t)$. The evolution of the distribution function is described by the Boltzmann equation,

$$\frac{\partial f_s}{\partial t} + \mathbf{v} \cdot \frac{\partial f_s}{\partial \mathbf{x}} + \frac{q_s}{m_s} \left(\mathbf{E} + \mathbf{v} \times \mathbf{B} \right) \cdot \frac{\partial f_s}{\partial \mathbf{v}} = \left(\frac{\partial f_s}{\partial t} \right)_{coll}.$$
 (2.1)

Each of the plasma constituents is represented by a distribution function. The model is sixdimensional as the position and velocity space dimensions are independent, which makes it computationally expensive. As a consequence, kinetic models are limited to narrow distributions, small spacial dimensions, and short time scales. In addition, velocity space extends to infinity, making the implementation of boundary conditions challenging.

Particle-in-Cell (PIC) models describe the plasma as electrons and ions particles responding to the electromagnetic forces and collisions. To reduce the complexity of the problem, instead of evolving individual particles, super-particles are used, which represent many particles, but have the same mass-to-charge ratio as individual ones. The problem with these super-particles is that they can produce statistical errors caused by relatively fewer particles than in actual plasmas. In addition, the model is six-dimensional, making it computationally expensive as well.

In Ref. [1] a two-fluid plasma model is presented, which reduces the six-dimensional kinetic model to three dimensions. This reduction is achieved by taking the first three

velocity moments of the Boltzmann equation for all the plasma species. The moments describe the evolution of the bulk properties of the plasma: density, momentum, and energy. The pressure is assumed to be isotropic and the heat flux tensor is zero. The model is derived by assuming local thermodynamic equilibrium within each fluid, but not between different fluids.

The magnetohydrodynamics (MHD) model[17], the most widely used plasma model, is derived from the two-fluid plasma model by neglecting the electron momentum and assuming the speed of light is much larger than any speeds in the system (infinite speed of light). As a consequence of neglecting the electron inertia, the electron momentum equation reduces to the generalized Ohm's law and the kinetic energy of the electrons is zero. In addition, the infinite speed of light assumption ignores all the high frequency electromagnetic waves, and sets the vacuum permitivity to zero. This means that the displacement current term of Ampere's law is zero, and from Poisson's equation this assumption implies that the electron and ion number density must always be equal (quasi-neutral plasma). The MHD model is often further simplified to an ideal MHD model, which limits its applicability to high collisionality, small Larmor radius, and low resistivity regimes. The two-fluid model is a generalization of the MHD model, which makes it applicable to a broader range of plasma regimes.

For the applications of interest in this dissertation, an expansion of the two-fluid plasma model to a multi-fluid plasma model is done to describe plasmas where more than one ion or neutral species are present. The multi-fluid can be applied to a wider range of plasma regimes than MHD and is less computationally expensive than kinetic or PIC models making it a good compromise between computational cost and plasma regimes.

2.2 Derivation of the multi-fluid plasma model equations

The multi-fluid plasma model includes a description for the evolution of multiple species: ions, neutrals, and electrons[16]. Each species mass, momentum, and energy is evolved separately. Multiple species add multi-scale effects to the model. The electron dynamics occur at fast time scales while the ion and neutral dynamics happens at much slower time-scales. The disparate scales are often a manifestation of the mass ratio of the species

and their interaction with the electromagnetic fields. This interaction produces waves that propagate in the plasma at different speeds, and some propagation occurring at faster than MHD waves[1].

Evaluating the velocity moments of Eq. (2.1) result in the multi-fluid plasma model, where, the zeroth moment produces the conservation of mass, the first moment the conservation of momentum and the third moment the conservation of energy. The process of obtaining the equations is described in details in Refs. [32] and [33]. The right-hand-side of the Boltzmann equation accounts for the species collisions. Collisions can be grouped into scattering and reacting collisions such as ionization, recombination and charge exchange, however, here only scattering collision will be considered, the plasma is assumed to be fully ionized.

The zeroth velocity moment provides a statement for conservation of mass,

$$\frac{\partial \rho_s}{\partial t} + \nabla \cdot (\rho_s \mathbf{u}_s) = 0, \tag{2.2}$$

where the subscript s denotes the species, ρ_s is the density, \mathbf{u}_s is the velocity. The first moment is conservation of momentum,

$$\frac{\partial \rho_s \mathbf{u}_s}{\partial t} + \nabla \cdot \left(\rho_s \mathbf{u}_s \mathbf{u}_s + p_s \overleftarrow{\mathbf{\Pi}} \right) = \frac{\rho_s q_s}{m_s} \left(\mathbf{E} + \mathbf{u}_s \times \mathbf{B} \right) + \sum_r \mathbf{R}_{rs} - \nabla \cdot \overleftarrow{\mathbf{\Pi}}_s, \tag{2.3}$$

and the second moment is the conservation of energy,

$$\frac{\partial \varepsilon_s}{\partial t} + \nabla \cdot ((\varepsilon_s + p_s)\mathbf{u}_s) = \left(\frac{\rho_s q_s}{m_s} \mathbf{E} + \sum_r \mathbf{R}_{rs}\right) \cdot \mathbf{u}_s + \overleftrightarrow{\mathbf{\Pi}}_s : \nabla \mathbf{u}_s - \nabla \cdot \mathbf{q}_s + \sum_r Q_{rs}. \quad (2.4)$$

E and **B** are the electric and magnetic fields, m is the mass, q_s is the charge, p_s is the pressure, and ε_s is the total energy given as

$$\varepsilon_s = \frac{p_s}{\gamma - 1} + \frac{1}{2}\rho_s |\mathbf{u}_s|^2. \tag{2.5}$$

The term \mathbf{R}_{rs} accounts for the momentum transfer between species s and r. In momentum transfer between the ions and the electrons, the more massive ions lose less momentum

than the electrons. In other words, this term accounts for the electrical resistive force, and $\mathbf{R}_{rs} \cdot \mathbf{u}_s$ is Ohmic heating. The momentum term is obtained from Ref. [34] as,

$$\mathbf{R}_{rs} = -\nu_s \rho_s (\alpha_o \mathbf{v}_{\parallel} + \mathbf{v}_{\perp}) \tag{2.6}$$

where ν_s is the collision frequency and $\mathbf{v} = \mathbf{u}_r - \mathbf{u}_s$, $\alpha_o = 0.51$ for Z = 1 and $\alpha_o = 0.44$ for Z = 2. The subscripts \parallel and \perp denote the directions parallel and perpendicular to magnetic field. The electron-ion, ν_e , and ion-ion, ν_i , collision frequencies are given as

$$\nu_e = \frac{4\sqrt{2\pi}e^4 Z^2 n_i \log \Lambda}{3\sqrt{m_e} T_e^{3/2}},\tag{2.7}$$

$$\nu_i = \frac{4\sqrt{\pi}e^4 Z^4 n_i \log \Lambda}{3\sqrt{m_i} T_i^{3/2}},\tag{2.8}$$

where Z is the ionization level, e is the electron charge, and $\log \Lambda$ is the Coulomb logarithm.

The viscous stress tensor, $\overrightarrow{\Pi}_s$, corresponds to a random-walk diffusion of momentum. Ion viscosity is greater than the electron viscosity by a factor of $m_i/m_e[34]$, which implies that the viscosity of a plasma is primarily governed by the ions. There is dissipation of energy in the form of heat due to viscosity, which is accounted for by the viscous heating term $\overrightarrow{\Pi}_s : \nabla \mathbf{u}_s$. The viscous stress tensor, in the absence of strong magnetic fields, is defined as

$$\overleftrightarrow{\Pi}_s = -\eta_s \overleftrightarrow{\mathbf{W}}_s \tag{2.9}$$

where η_s is the species viscosity and defined for electrons and ions as

$$\eta_e = 0.73 p_e / \nu_e \quad \eta_i = 0.96 p_i / \nu_i,$$
(2.10)

and

$$\overleftrightarrow{\mathbf{W}}_{s} = \nabla_{\alpha} \mathbf{u}_{s\beta} + \nabla_{\beta} \mathbf{u}_{s\alpha} - \frac{2}{3} \delta_{\alpha\beta} \nabla \cdot \mathbf{u}_{s}. \tag{2.11}$$

The first two terms on the right-hand-side of the equation above, are the transposes of each other, velocity gradients. The $\delta_{\alpha\beta}$ ensures that the divergence of the velocity is applied only for the diagonal components of the velocity gradient tensor.

In Eq. (2.4), Q_{rs} is the thermal equilibration term between species, which drives the plasma to reach an equilibrium temperature for all species in the absence of other transport terms. The thermal equilibration is evaluated differently for ions and electrons

$$Q_{ie} = Q_{\Delta} = \frac{3\rho_e \nu_e}{m_i} (T_e - T_i), \tag{2.12}$$

$$Q_{ei} = -\mathbf{R}_{ie} \cdot (\mathbf{u}_e - \mathbf{u}_i) - Q_{\Delta}, \tag{2.13}$$

$$Q_{ii'} = \frac{3\rho_i \nu_i}{m_{i'}} (T_i - T_{i'}), \tag{2.14}$$

where e represents the electrons, i is any ion, i' is a different ion species. The temperature is $T_s = p_s/n_s$, and n_s is the number density.

The heat flux, \mathbf{q}_s in Eq. (2.4), represents the diffusion of energy associated with the random motion of particles. In magnetized plasmas the heat flux parallel and perpendicular to the magnetic field are different. In the direction parallel to the field, the electron thermal conductivity is greater than the ion thermal conductivity by a factor of $\sqrt{m_i/m_e}$ at similar temperatures[34]. But in perpendicular direction the reverse is true by the same factor. However, in cases where there are steep temperature gradients, and the ratio of the ion and electron average mean free path $\lambda_{i,e}$ to the scale length of the temperature gradient $L_T = T/|\nabla T|$ is not small, e.g. $\lambda_{i,e}/L_T \geq 10^{-2}$ the heat flow should be replaced by the free streaming heat flux [35, 36], given as

$$\mathbf{q}_s = f m_s^{-1/2} n_s T_s^{3/2} \hat{\mathbf{t}}$$
 (2.15)

where $\hat{\mathbf{t}} = \nabla T/|\nabla T|$ is a unit vector in the direction of the temperature gradient, and f is the flux limiter usually determined by comparing results to experimental measurements. A value of f = 0.03 is usually used[35].

2.3 Maxwell's equations

The electromagnetic fields, **E** and **B**, are solved with Maxwell's equations

$$\frac{\partial \mathbf{B}}{\partial t} + \nabla \times \mathbf{E} = 0, \tag{2.16}$$

$$\frac{1}{c^2} \frac{\partial \mathbf{E}}{\partial t} - \nabla \times \mathbf{B} = -\mu_o \sum_s \frac{q_s}{m_s} \rho_s \mathbf{u}_s, \tag{2.17}$$

$$\epsilon_o \nabla \cdot \mathbf{E} = \sum_s \frac{q_s}{m_s} \rho_s, \tag{2.18}$$

$$\nabla \cdot \mathbf{B} = 0, \tag{2.19}$$

where ϵ_o is the permittivity of free space, μ_o is the permeability of free space and $c = 1/\sqrt{\epsilon_o \mu_o}$ is the speed of light.

Maxwell's equations are overdetermined. There are six unknowns and eight equations. Analytically the two divergence equation, Gauss' law and the divergence of the magnetic field, are satisfied over time as long the initial conditions satisfy them, but numerically there are round-off errors that violate these divergence constraints. To address this problem, Maxwell's equations are cast in purely hyperbolic form as described in Ref. [37],

$$\frac{\partial \mathbf{B}}{\partial t} + \nabla \times \mathbf{E} + \gamma \nabla \Psi = 0, \tag{2.20}$$

$$\frac{1}{c^2} \frac{\partial \mathbf{E}}{\partial t} - \nabla \times \mathbf{B} + \chi \nabla \Phi = -\mu_o \sum_s \frac{q_s}{m_s} \rho_s \mathbf{u}_s, \tag{2.21}$$

$$\frac{1}{\chi} \frac{\partial \Phi}{\partial t} + \nabla \cdot \mathbf{E} = \sum_{s} \frac{q_s}{m_s} \rho_s, \qquad (2.22)$$

$$\frac{1}{\gamma c^2} \frac{\partial \Psi}{\partial t} + \nabla \cdot \mathbf{B} = 0. \tag{2.23}$$

Error correction potentials Ψ and Φ are introduced for the divergence of \mathbf{B} and \mathbf{E} respectively. In this model, the errors are propagated out of the computational domain at speeds equal or larger than the speed of light, c. The error propagation speed is set by the error correction coefficients γ and χ . The larger the value of coefficients the larger the error propagation speed is, i.e., the errors are propagated out of the computational domain faster. However, large error propagation speeds require more restrictive explicit time steps, as the error propagation speed become the fastest traveling waves in the system. Therefore, in most problems, a value of one is sufficient to enforce the divergence constraints.

2.4 Normalized multi-fluid equations

The multi-fluid plasma equation can be cast in non-dimensional form. There are numerical and physical advantages to casting model in this form. Physically non-dimensionalization has the advantage that all systems, independent of size, that have the same non-dimensional parameters will behave in the same way. Numerically non-dimensionalization, can make a system less stiff, and easier to converge to a solution.

For the normalization used here, a characteristic mass density, velocity, and length scale (ρ_0, u_0, L) are introduced, and the normalized values are defined as $\tilde{\rho}_s \equiv \rho_s/\rho_0$, $\tilde{\mathbf{u}}_s \equiv \mathbf{u}_s/u_0$, and $\tilde{\mathbf{x}} \equiv \mathbf{x}/L$. Substituting these normalizations into Eq. (2.2) gives

$$\left[\frac{\rho_0}{\tau}\right] \frac{\partial \tilde{\rho}_s}{\partial \tilde{t}} + \left[\frac{\rho_0 u_0}{L}\right] \tilde{\nabla} \cdot (\tilde{\rho}_s \tilde{\mathbf{u}}_s) = 0.$$

Setting the characteristic time (τ) to $\tau \equiv t/\tilde{t} = L/u_0$, the terms in the square brackets cancel, and the normalized continuity equation simplifies to

$$\frac{\partial \rho_s}{\partial t} + \nabla \cdot (\rho_s \mathbf{u}_s) = 0, \tag{2.24}$$

where the tildes have been dropped for clarity.

The momentum equation, Eq. (2.3), is also normalized using the same characteristic values and additional ones for pressure, electric and magnetic fields (p_0, E_0, B_0) . Each species charge is normalized by the electron charge, which introduces the ionization level $Z_s = q_s/e$. The momentum equation becomes

$$\left[\frac{\rho_{0}u_{0}}{\tau}\right] \frac{\partial \left(\tilde{\rho}_{s}\tilde{\mathbf{u}}_{s}\right)}{\partial \tilde{t}} + \left[\frac{\rho u_{0}^{2}}{L}\right] \tilde{\nabla} \cdot \left(\tilde{\rho}_{s}\tilde{\mathbf{u}}_{s}\tilde{\mathbf{u}}_{s}\right) + \left[\frac{p_{0}}{L}\right] \tilde{\nabla}\tilde{p}_{s} = \\
\left[en_{0}E_{0}\right] Z_{s}\tilde{n}_{s}\tilde{\mathbf{E}} + \left[en_{0}u_{0}B_{0}\right] Z_{s}\tilde{n}_{s}\tilde{\mathbf{u}}_{s} \times \tilde{\mathbf{B}} + \\
\sum_{r} \left[\rho_{0}\mathbf{u}_{0}\nu_{s}\right]\tilde{\rho}_{s}\left(\alpha_{o}\tilde{\mathbf{v}}_{\parallel} + \tilde{\mathbf{v}}_{\perp}\right) - \tilde{\nabla} \cdot \left(\left[\frac{\eta_{0}u_{0}}{L^{2}}\right] \overleftrightarrow{\mathbf{W}}_{s}\right), \quad (2.25)$$

and $n_0 = \rho_0/m_0$. The terms in square brackets on the left-hand side cancel if the characteristic pressure is set to $p_0 = m_0 n_0 u_0^2$. However, the terms in square brackets on the

right-hand side do not cancel. The normalized characteristic ion skin depth is defined as

$$\delta \equiv \frac{\delta_i}{L} = \frac{c}{\omega_{pi}} = \sqrt{\frac{\epsilon_0 m_0 c^2}{e^2 n_0 L^2}}.$$
 (2.26)

which is then used to set the characteristic electric field, $E_0 = (m_0 c^2) / (eL\delta^2)$, the subscript 0 denotes the plasma species that is being used as reference for the normalization. The normalized, characteristic Larmor radius is defined as

$$r_L \equiv \frac{r_{L0}}{L} = \frac{u_0}{\omega_{ci}L} = \frac{m_0 u_0}{eLB_0},$$
 (2.27)

which then sets the characteristic magnetic field, $B_0 = \left(m_0 u_0\right)/\left(eLr_L\right)$. The Knudsen number is

$$Kn_s = \lambda_s^{mfp}/L, \qquad (2.28)$$

where $\lambda_s^{mfp} = u_0/\nu_s$ is the mean-free-path of species s, and the Reynolds number is defined as $\text{Re}_s = \frac{\rho_0 u_0 L}{\eta_s}$. The Knudsen and Reynolds numbers are related by

$$Kn = \frac{1}{Re}.$$
 (2.29)

The normalized momentum equation simplifies to

$$\frac{\partial \left(\rho_{s} \mathbf{u}_{s}\right)}{\partial t} + \nabla \cdot \left(\rho_{s} \mathbf{u}_{s} \mathbf{u}_{s}\right) + \nabla p_{s} = \frac{1}{\delta^{2}} \frac{c^{2}}{u_{0}^{2}} Z_{s} n_{s} \mathbf{E} + \frac{1}{r_{L}} Z_{s} n_{s} \mathbf{u}_{s} \times \mathbf{B} + \sum_{r} \frac{1}{\mathrm{Kn}_{s}} \rho_{s} (\alpha_{o} \mathbf{v}_{\parallel} + \mathbf{v}_{\perp}) - \nabla \cdot \left(\mathrm{Kn}_{s} \overleftrightarrow{\mathbf{W}}_{s}\right). \quad (2.30)$$

The tildes have again been dropped for clarity.

Following the same procedure, the energy Eq. (2.4) is normalized and becomes,

$$\frac{\partial \varepsilon_s}{\partial t} + \nabla \cdot ((\varepsilon_s + p_s) \mathbf{u}_s) = \frac{1}{\delta^2} \frac{c^2}{u_0^2} Z_s n_s \mathbf{u}_\alpha \cdot \mathbf{E} + \sum_r \frac{1}{\mathrm{Kn}_s} \rho_s (\alpha_o \mathbf{v}_{\parallel} + \mathbf{v}_{\perp}) \cdot \mathbf{u}_s
- \mathrm{Kn}_s \overleftrightarrow{\mathbf{W}}_s : \nabla \mathbf{u}_s - \nabla \cdot \mathbf{q}_s + \frac{1}{\mathrm{Kn}_s} \sum_r Q_{rs}, \quad (2.31)$$

Maxwell's equation also need to be normalized using the same non-dimensional parameters. The normalized Gauss's law is

$$\nabla \cdot \mathbf{E} = \sum_{s} Z_{s} n_{s}, \tag{2.32}$$

the divergence of magnetic field remains the same

$$\nabla \cdot \mathbf{B} = 0 \tag{2.33}$$

Faraday's law is,

$$\frac{\partial \mathbf{B}}{\partial t} + \frac{r_L}{\delta^2} \frac{c^2}{u_0^2} \nabla \times \mathbf{E} = 0, \tag{2.34}$$

and Ampere's law becomes,

$$\frac{\partial \mathbf{E}}{\partial t} - \frac{\delta^2}{r_L} \nabla \times \mathbf{B} = -\sum_s Z_s n_s \mathbf{u}_s. \tag{2.35}$$

2.5 Ideal Multi-Fluid Plasma Model

An ideal form of the multi-fluid plasma equations can be obtained when the viscosity and the heat flux are zero and there is no interspecies collisions. This assumption simplifies the calculations and reduces the computational cost because the anisotropic pressure tensor Π_s is not calculated. The balance laws for the multi-fluid plasma model (dimensional) are given by

$$\frac{\partial \rho_s}{\partial t} + \nabla \cdot (\rho_s \mathbf{u}_s) = 0, \tag{2.36}$$

$$\frac{\partial \rho_s \mathbf{u}_s}{\partial t} + \nabla \cdot (\rho_s \mathbf{u}_s \mathbf{u}_s + p_s \mathbf{I}) = \frac{\rho_s q_s}{m_s} (\mathbf{E} + \mathbf{u}_s \times \mathbf{B}), \tag{2.37}$$

$$\frac{\partial \varepsilon_s}{\partial t} + \nabla \cdot ((\varepsilon_s + p_s)\mathbf{u}_s) = \frac{\rho_s q_s}{m_s} \mathbf{u}_s \cdot \mathbf{E}, \qquad (2.38)$$

Maxwell's equations are expressed as Eqs. (2.16)-(2.19).

2.6 Numerical properties of the Multi-Fluid Plasma Model

The multi-fluid plasma equations are inhomogeneous with hyperbolic homogeneous part, meaning that the system flux Jacobian has real eigenvalues and a complete set of eigenvectors. Hyperbolic equation systems can be cast in balance form as

$$\frac{\partial \mathbf{Q}}{\partial t} + \nabla \cdot \overleftrightarrow{\mathbf{F}} = \mathbf{S},\tag{2.39}$$

where \mathbf{q} is the vector of conserved variables, $\overrightarrow{\mathbf{F}}$ is the flux tensor and \mathbf{S} is the source term. The eigenvalues of the flux Jacobian $(\partial \overrightarrow{\mathbf{F}}/\partial \mathbf{Q})$ are the characteristic speeds of the multi-fluid equation system, the fluids speed of sound,

$$c_{se} = \sqrt{\frac{\gamma p_e}{\rho_e}}, \quad c_{si} = \sqrt{\frac{\gamma p_i}{\rho_i}}$$
 (2.40)

and the speed of light, c. The subscript i in equation Eq. (2.40) represents all the ion species. In addition, the eigenvalues of the source Jacobian ($\partial \mathbf{S}/\partial \mathbf{Q}$) are all purely imaginary[20] and the first three being $0, \pm i\omega_p$, where ω_p is the plasma frequency,

$$\omega_{ps} = \sqrt{\frac{n_s q_s^2}{\epsilon_o m_s}}. (2.41)$$

Imaginary eigenvalues of the source Jacobian make the sources dispersive. This dispersion is physical not numerical, and is due to the presence of a wide range of plasma waves that result from the interaction of the charged fluids with the electromagnetic fields. The presence of physical dispersion restrict the type of numerical methods that can be used to properly capture such dispersion and not introduce numerical dispersion nor numerical dissipation that might dampen such oscillations.

2.7 Summary

The multi-fluid plasma model is presented as a generalization of the MHD model, and applicable to a broad range of plasma regimes. The model is less computationally expensive than PIC and kinetic codes, while retaining the relevant physics for most engineering ap-

plications and experiments. Collisional terms are given by the Braginskii closures and the system of equations are normalized so that all collisional terms depend on the same non-dimensional parameter, the Knudsen number. The electric field is scaled by the ion skin depth and the magnetic fields by the Larmor radius, and the field evolution is done using Maxwell's equations. The model has disparate time scales that need to be resolved in order to properly describe the physics of a problem.

Chapter 3

A BLENDED FINITE ELEMENT METHOD

3.1 Prior and foundational work

The choice of numerical methods that can be used in the solution of a partial differential equation (PDE) is dictated by the PDE's type. The multi-fluid plasma equations, described in Chapter 2, form an inhomogeneous equation system with homogeneous hyperbolic part, which can be put in balance law form given by Eq. (2.39). A balance law PDE is said to have hyperbolic homogeneous part if the flux Jacobian, $\partial \overrightarrow{F}/\partial \mathbf{Q}$, has real eigenvalues and a complete set of distinct eigenvectors. Balance laws can be solved using the finite volume wave propagation method described in Ref. [38]. This numerical method is second-order accurate, it provides good resolution of shocks even when the initial conditions are smooth, and is conservative.

The wave propagation method has been successfully applied to fluid mechanics[39], elasticity[40], Tsunami modeling[41], etc. In Ref. [42] the method is successfully applied to the magnetic reconnection problem using a two-fluid plasma model, where the reconnected flux calculated as comparable to the results of the GEM challenge magnetic reconnection[2]. The wave propagation method cannot incorporate the source term directly into the calculation of the fluxes and requires source splitting techniques. This produces phase errors when the characteristic frequency is high compared to the frequency of information propagation[20].

Continuous Galerkin (CG) finite element methods have also been used for solving plasma models. In the CG method the variables are represented within each element using polynomial basis functions where the order of the polynomials determine the spatial order of accuracy of the method. In Ref. [24] a reduced quintic triangular finite element method for MHD is presented. The method enforces continuity of the solution and its first derivative. In Ref. [43] a CG method for the extended MHD model is implemented in the NIMROD

code. The code is restricted to periodic configurations, and is a conforming representation composed of 2D finite elements in the poloidal plane and finite Fourier series in the toroidal direction. NIMROD has been used extensively in plasma simulations in Refs. [44, 45, 46, 47].

CG methods tend to be dispersive and often require some artificial dissipation to damp high frequency oscillations. The MHD model, with low speed flows, there are dissipation terms that ensure smoothness. The multi-fluid plasma model on the other hand is dispersive, and has no physical source of dissipation, therefore for the implementation discussed in this dissertation (Sec. 3.3), artificial dissipation is used to dampen high frequency oscillations.

The MHD model has a large range of timescales which makes implicit time integration desirable for most simulations. In Ref. [48] an implicit method is applied using a CG method. And in Ref. [49] the hyperbolic MHD model is converted into parabolic equations in order to make them more amenable to multigrid methods and physics-based preconditioning. This in turn makes the Jacobian-free implicit time integration diagonally dominant and convergence is attained using few iterations. CG methods are well suited to use implicit time integration methods and are used in this dissertation (Sec. 3.5) for the multi-fluid plasma model to relax the disparate time constrains imposed by an explicit method.

A method that combines the advantages of both finite volume methods (good shock capturing and conservation properties) and CG methods (high order accuracy and flux/source coupling) is the Discontinuous Galerkin (DG) finite element method. The method was introduced by Ref. [50] for the study of two-dimensional neutron transport. Like in CG, the DG solution is represented by a set of polynomial basis functions in each element but there is no continuity enforcement at the element boundaries.

The DG method was expanded to solve non-linear equations in Ref. [51] where they use total variation diminishing (TVD) Runge-Kutta time integration, and the Navier-Stokes equations [52] for unstructured grids and linear, quadratic, and cubic elements [53, 54, 55].

In plasma simulations the DG method has been used to model ideal MHD in Refs. [56] and [57], and in kinetic modeling for the Vlasov-Poisson equation system in Ref [58]. An extensive study of the DG method applied to the two-fluid plasma model and the challenges of the dispersive source term can be found in Ref. [20]. It was shown there that, the DG method was able to capture high frequency oscillations accurately at higher order discretiza-

tions without producing phase error, while accurately representing the relevant physics. The major benefit of the DG method is that it is remarkably robust in the presence of rapid oscillations while simultaneously capturing discontinuity fronts. One of the disadvantages of the DG method is that, with a polynomial basis function of degree p, the explicit timestep is limited by the CFL condition as $CFL \le 1/(2p-1)[22]$. This CFL restriction can be extremely costly for problems that require high resolution.

An ideal numerical method for multi-fluid plasma model would be one that: is capable of capturing shocks, has high order accuracy, resolves fast oscillations, and does not impose strict time-step limitations, e.g. an implicit DG method. In Ref. [23] an implicit time integration for the complete two-fluid plasma model discretized using DG was attempted; however, the non-linear Newton solver would not always converge. This was due to the fact that in regions of sharp gradients the use of limiters is required, and that made the Jacobian for the non-linear solver ill-conditioned.

A blended finite element method (BFEM) is presented to achieve the goals described in the previous paragraph. In the blended finite element method the electron fluid and the electromagnetic fields are represented using a CG method while all ions and neutral fluids are represented using a DG method. This ensures that the method is higher order accurate (depending on the basis functions used), and is able to resolve fast oscillations (flux and sources are coupled). Regarding shock capturing, for most plasma of interest the electron fluid and the electromagnetic fields are smooth throughout the domain, and in most cases do not have sharp gradient or discontinuities making their representation with a CG method appropriate. Shocks occur in ion and neutral fluids and are captured with the DG method.

Smooth solution in the electron fluid and electromagnetic fields means that there is no need to use limiters, which makes them excellent candidates for implicit time integration. The time-stepping is dictated by the characteristic speeds of the multi-fluid plasma model, which are the species acoustic speeds and the speed of light. In addition, the characteristic frequencies (plasma and cyclotron) need to be resolved to capture the full physics of the multi-fluid model. Evolving the electron fluid and electromagnetic fields implicitly removes the strictest time-step limitation, namely those due to the speed of light, the electron acoustic speed, and the electron plasma and cyclotron frequencies. In this dissertation a

Crank-Nicholson[59] implicit time integration is used.

The ion and neutral fluids do shock and require limiters, which is where implicit DG time integration has the most challenges, so these fluids are evolved explicitly using Runge-Kutta time integration (Sec. 3.6). Therefore, we can achieve the goals of capturing shocks where it is needed, higher order spatial accuracy everywhere, and have relaxed the time-step restrictions considerably by removing the most stringent limitations.

3.2 Description of the Numerical Method

In the new BFEM method the ion and neutral fluids are modeled using a DG method with an explicit Runge-Kutta time integration method, while a CG method with implicit time integration is used for the electron and the electromagnetic fields. Since the fast moving electrons and the fields do not shock, limiters are not needed and the Jacobian for a Newton solver is not ill-conditioned. This allows for bigger time steps compared to a fully explicit method. Often the electron dynamics or the speed of light impose the most restrictive time step constraints for explicit methods. The DG method for the ions and neutrals is evolved explicitly, nonetheless, the time steps are less stringent than an entirely explicit method.

3.3 Continuous Galerkin Finite Element Method

In the continuous Galerkin [60] (CG) finite element method the variables are expanded as a series of polynomial shape functions (also known as interpolation functions) over the volume of each element, Ω . The order of the polynomials define the spatial order of accuracy of the numerical method, and how fast the numerical solution converges to the exact solution as the element size decreases. If the element size is defined as h and the polynomial order is p the error in the solution is of order $O(h^{p+1})$, e.g., for linear elements p = 1 and the convergence rate is of order $O(h^2)$, therefore, halving the element size decreases the error in the solution by a factor of four.

In nodal CG C^0 continuity is enforced where adjacent elements have the same nodal values but the derivatives are not continuous at element boundaries, as depicted in Fig. 3.1.

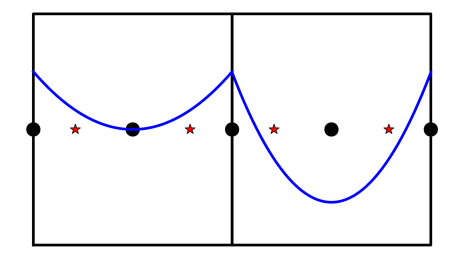


Figure 3.1: Two CG elements are shown. The blue curves are the solution within each element, and the solution is continuous at element boundaries even though the derivatives in not. The black dots are the location of the nodes for a second order representation, where adjacent element share one node. The stars are the location of the quadrature points.

For this implementation, Eq. (2.39) is changed to

$$\frac{\partial \mathbf{Q}}{\partial t} + \frac{\partial \overleftarrow{\mathbf{F}}}{\partial \mathbf{Q}} \cdot \frac{\partial \mathbf{Q}}{\partial \mathbf{x}} = \mathbf{S},\tag{3.1}$$

where $\partial \overrightarrow{\mathbf{F}}/\partial \mathbf{Q}$ is the flux Jacobian. The solution is expanded within each element as

$$\mathbf{Q} = \sum_{j=1}^{p} q_j \psi_j, \tag{3.2}$$

where ψ_j are the interpolation functions and q_j are the nodal values. In CG, Lagrange polynomials are usually used as interpolation functions because they have the value of one, on one of the nodes $\psi_p(x=x_p)=1$, and zero on all other nodes of a given element. An n-1 order polynomial interpolation function is represented by n nodes along each dimension. The Lagrange polynomials are defined as

$$\psi_j(x) = \prod_{k=1, k \neq j}^n \frac{x - x_k}{x_j - x_k},$$
(3.3)

where x_j and x_k are nodal coordinates. Equation (3.1) is multiplied by the test functions

and integrated over each element volume

$$\int_{\Omega} d\mathbf{x} v_j \frac{\partial \mathbf{Q}}{\partial t} + \int_{\Omega} d\mathbf{x} v_j \frac{\partial \overleftarrow{\mathbf{F}}}{\partial \mathbf{Q}} \cdot \frac{\partial \mathbf{Q}}{\partial \mathbf{x}} = \int_{\Omega} d\mathbf{x} v_j \mathbf{S}.$$
 (3.4)

In a Galerkin method the test and interpolation functions are the same, $v_j = \psi_j$, therefore the governing equation becomes

$$\int_{\Omega} d\mathbf{x} \psi_j \frac{\partial}{\partial t} \sum_{p=1}^n \psi_j \mathbf{q}_p + \int_{\Omega} d\mathbf{x} \frac{\partial \overrightarrow{\mathbf{F}}}{\partial \mathbf{Q}} \psi_j \frac{\partial}{\partial \mathbf{x}} \sum_{p=0}^n \psi_p \mathbf{q}_p = \int_{\Omega} d\mathbf{x} \psi_j \mathbf{S}.$$
 (3.5)

Since the nodal values \mathbf{q}_p do not vary in space they can be brought outside the integral

$$\frac{\partial \mathbf{q}_p}{\partial t} \int_{\Omega} d\mathbf{x} \psi_j \psi_p + \mathbf{q}_p \int_{\Omega} d\mathbf{x} \frac{\partial \overleftarrow{\mathbf{F}}}{\partial \mathbf{Q}} \psi_j \frac{\partial \psi_p}{\partial \mathbf{x}} = \int_{\Omega} d\mathbf{x} \psi_j \mathbf{S}. \tag{3.6}$$

The first integral is the element mass matrix,

$$\overrightarrow{\mathbf{M}}_{\Omega} = \int_{\Omega} d\mathbf{x} \psi_j \psi_p. \tag{3.7}$$

The spatially dependent terms can be moved to the right-hand-side,

$$\overrightarrow{\mathbf{M}}_{\Omega} \frac{\mathbf{q}_{p}^{n+1} - \mathbf{q}_{p}^{n}}{\Delta t} = -\int_{\Omega} d\mathbf{x} \frac{\partial \overrightarrow{\mathbf{F}}}{\partial \mathbf{Q}} \psi_{j} \frac{\partial \psi_{p}}{\partial \mathbf{x}} \mathbf{q}_{p} + \int_{\Omega} d\mathbf{x} \psi_{j} \mathbf{S}.$$
(3.8)

and evaluated using Gauss-Legendre quadrature rules.

The CG method introduces no dissipation, and in regions of sharp gradient it is prone to high frequency oscillations (Gibbs phenomenon). These oscillations can be dampened by adding some artificial numerical dissipation. A second derivative of the conserved variables is added to Eq. (2.39),

$$\frac{\partial \mathbf{Q}}{\partial t} + \nabla \cdot \overleftrightarrow{\mathbf{F}} = \mathbf{S} + \kappa \nabla^2 \mathbf{Q}^*, \tag{3.9}$$

where the scalar κ is added to scale the numerical dissipation and minimize the impact it may have on the physics of the problem. The vector \mathbf{Q}^* indicates that the modeled variable components being dissipated may be a subset of the conserved ones.

Multiplying the dissipation term by the basis functions, integrating over the element volume, and expanding \mathbf{Q}^* with basis functions, the following is attained

$$\kappa \nabla^2 \mathbf{Q}^* \Rightarrow \int_{\Omega} d\mathbf{x} v \kappa \nabla^2 \mathbf{Q}^* \Rightarrow -\kappa \mathbf{q}_p^* \int_{\Omega} d\mathbf{x} \frac{\partial \psi_j}{\partial \mathbf{x}} \frac{\partial \psi_p}{\partial \mathbf{x}} + \kappa \left(\psi_j \frac{\partial \psi_p}{\partial \mathbf{x}} \mathbf{q}_p^* \right)_{\partial \Omega}. \tag{3.10}$$

The last term in Eq. (3.10) is a surface term and in the CG method that is a physical boundary term, which accounts for boundary conditions, in particular the natural/Neumann boundary conditions.

Let the artificial dissipation matrix be defined as,

$$\overrightarrow{\mathbf{D}}_{\Omega} = -\kappa \int_{\Omega} \frac{\partial \psi_j}{\partial \mathbf{x}} \frac{\partial \psi_p}{\partial \mathbf{x}} d\mathbf{x}, \tag{3.11}$$

and the source vector as

$$\mathbf{f}_{\Omega} = \int_{\Omega} \psi_j \mathbf{S} d\mathbf{x},\tag{3.12}$$

and moving all the spatially dependent terms to the right-hand-side, the evolution equation can be written as

$$\overrightarrow{\mathbf{M}}_{\Omega} \frac{\mathbf{q}_{p}^{n+1} - \mathbf{q}_{p}^{n}}{\Delta t} = -\mathbf{q}_{p} \int_{\Omega} d\mathbf{x} \frac{\partial \overrightarrow{\mathbf{F}}}{\partial \mathbf{q}} \psi_{j} \frac{\partial \psi_{p}}{\partial \mathbf{x}} + \mathbf{f}_{\Omega} + \overrightarrow{\mathbf{D}}_{\Omega} \mathbf{q}_{p}^{*} + \kappa \left(\psi_{j} \frac{\partial \psi_{p}}{\partial \mathbf{x}} \mathbf{q}_{p}^{*} \right)_{\partial \Omega} = \mathbf{R}(\mathbf{q}_{p}^{n}). \quad (3.13)$$

In the CG method, all the unknowns (nodal values) must be solved simultaneously, therefore the element equations are assembled into global mass $(\overrightarrow{\mathbf{M}})$ and dissipation $(\overrightarrow{\mathbf{D}})$ matrices. The integral term in Eq. (3.13) and the source vector (\mathbf{f}_{Ω}) also need to be assembled into a global vectors. The link between the local matrices and the global ones is done through a connectivity matrix whose coefficient b_{ij} is the global node number corresponding node j of element i[60]. In continuous Galerkin nodes are shared between elements, which means that some node numbers will appear in multiple rows of the connectivity matrix. For example, the element mass matrix entries (M_{kl}^e) are added to the global matrix according to

$$M_{mn} = \sum_{e=1}^{E} \sum_{k=1}^{N} \sum_{l=1}^{N} M_{kl}^{e}, \tag{3.14}$$

and $m = b_{ek}$, $n = b_{el}$. The total number of elements is E and the number of nodes per element is N.

3.4 Discontinuous Galerkin Method

The discontinuous Galerkin (DG) method implemented here follows closely the implementation done in Refs. [23, 21]. The main difference between the DG and CG methods is the way the solution is treated between elements. While in CG the solution at element boundaries is required to be continuous, for the DG method the solution can be discontinuous. In addition, the CG method is a nodal finite element method while the DG method is a modal. The advantage of using modal for DG is that the implementation of limiters is easily done[23], while nodal CG can enforce continuity between elements because boundary nodes are shared between them.

The conserved variables are expanded as piecewise continuous polynomial of degree p within each element, as shown in Fig. 3.2.

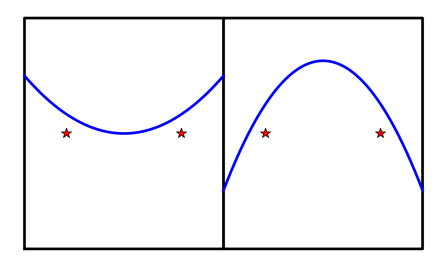


Figure 3.2: Two DG elements are shown. The blue curves are the solution within each element, and the solution is discontinuous at element boundaries. The stars are the location of the quadrature points. Note that the location of quadrature points for the DG method coincide with the ones of the CG method.

The order of the polynomials determine the spatial order of accuracy of the method as explained in the previous section. The conserved variables \mathbf{Q} from Eq. (2.39) are then expressed as linear combinations of shape functions v_p and expansion coefficients, \mathbf{q}_p , in

each element

$$\mathbf{Q} = \sum_{p=1}^{n} \mathbf{q}_p v_p. \tag{3.15}$$

Legendre polynomials up to order n-1 are used as test functions because they form an orthogonal basis,

$$\int_{\Omega} v_p(x)v_m(x)dx = \Delta V C_p \delta_{pm}$$
(3.16)

where ΔV is the volume of the element Ω , $C_p = 1/(2p+1)$ are normalized constants, and δ_{pm} is the Kronecker delta.

The balance laws equations in Eq. (2.39) are multiplied by the basis functions, v_p , and integrated over each element volume

$$\frac{\partial}{\partial t} \int_{\Omega} v_m \mathbf{Q} dV + \int_{\Omega} v_m \nabla \cdot \mathbf{F} dV = \int_{\Omega} \mathbf{S} v_m dV. \tag{3.17}$$

Integration by parts is applied to the second term, and the above equation becomes

$$\int_{\Omega} v_m \frac{\partial \mathbf{Q}}{\partial t} dV + \oint_{\partial \Omega} v_m \mathbf{F} \cdot d\mathbf{A} - \int_{\Omega} \mathbf{F} \cdot \nabla v_m dV = \int_{\Omega} v_m \mathbf{S} dV. \tag{3.18}$$

When the conserved variables are expanded using Eq. (3.15), and the orthogonality of the basis functions are taken into account the first term of the above equation simplifies to

$$\int_{\Omega} v_m \frac{\partial \mathbf{Q}}{\partial t} dV = \frac{\partial}{\partial t} \int_{\Omega} v_p v_m \mathbf{q}_p dV = \Delta V C_p \frac{\partial \mathbf{q}_p}{\partial t}.$$
(3.19)

The second term in Eq. (3.18) is a surface integral that accounts for the fluxes across each element boundary. The calculation of this numerical flux is done using Lax-Frederich flux expression, however other flux calculations can be used. Lax-Friedrich fluxes are given as

$$\mathbf{F} = \frac{1}{2}(F_i^+ - F_{i+1}^-) - \frac{1}{2}|\lambda|(Q_i^+ - Q_{i+1}^-), \tag{3.20}$$

where $|\lambda|$ is the maximum characteristic speed (eigenvalue of the flux Jacobian) of the average conserved values of elements i and i+1, and superscripts + and - represent the values at the upper and lower boundaries of an element, respectively. The integrals over the

volume of the elements, Ω , of Eq. (3.18) are evaluated using Gauss-Legendre quadrature rules. The temporally and spatially dependent terms can be separated

$$\frac{d\mathbf{q}_p}{dt} = \mathbf{L}(\mathbf{q}_p) = \frac{1}{\Delta V} \int_{\Omega} v \mathbf{S} dV - \frac{1}{\Delta V} \oint_{\partial \Omega} v \mathbf{F} \cdot d\mathbf{A} + \frac{1}{\Delta V} \int_{\Omega} \mathbf{F} \cdot \nabla v dV, \tag{3.21}$$

where $\mathbf{L}(\mathbf{q}_p)$ is the operator containing all the spatially dependent terms and the equation becomes an ordinary differential equation (ODE)

$$\frac{d\mathbf{q}_p}{dt} = \mathbf{L}(\mathbf{q}_p). \tag{3.22}$$

3.5 Implicit Theta-method Time Integration

The time integration for the CG method is done using the θ -method. The formulation of the θ -method for Eq. (3.13) is then given as

$$\overrightarrow{\mathbf{M}} \frac{\mathbf{q}^{n+1} - \mathbf{q}^n}{\Delta t} = (1 - \theta) \mathbf{R}(\mathbf{q}^n) + \theta \mathbf{R}(\mathbf{q}^{n+1}).$$
(3.23)

Choosing $\theta = 1$ the method is equivalent to the implicit backward Euler, and $\theta = 0$ is the explicit forward Euler but both methods are only first order accurate. When $\theta = 0.5$ it corresponds to the Crank-Nicholson method[59] which is an implicit method and second-order accurate.

A Newton method is used to solve for \mathbf{q}^{n+1} . The Newton method is used for finding successively better approximations to the roots of a real-valued function g(x + dx) = 0 (residual function),

$$g(x + \Delta x) = g(x) + g'(x)\Delta x + \dots = 0.$$
(3.24)

The residual function for the implicit finite element method is given as

$$\mathbf{G}(\mathbf{q}^n) = \frac{\overleftarrow{\mathbf{M}}}{\Delta t} (\mathbf{q}^{n+1} - \mathbf{q}^n) - (1 - \theta) \mathbf{R}(\mathbf{q}^n) - \theta \mathbf{R}(\mathbf{q}^{n+1}) = 0.$$
 (3.25)

The Jacobian is

$$\overrightarrow{\mathbf{J}}(\mathbf{q}^n) = \frac{\partial \mathbf{G}(\mathbf{q}^n)}{\partial \mathbf{q}^n} = \frac{\overleftarrow{\mathbf{M}}}{\Delta t} - (1 - \theta) \frac{\partial \mathbf{R}(\mathbf{q}^n)}{\partial \mathbf{q}^n}$$
 (3.26)

and the equation being solved is given as

$$\overleftrightarrow{\mathbf{J}}(\mathbf{q}^n)\Delta\mathbf{q} = -\mathbf{G}(\mathbf{q}^n),\tag{3.27}$$

$$\mathbf{q}^{n+1} = \mathbf{q}^n + \Delta \mathbf{q}. \tag{3.28}$$

3.6 Explicit Runge-Kutta Time Integration

Second-order total variation bounded (TVB) Runge-Kutta[51] time integration is used for DG method,

$$\mathbf{q}_p^1 = \mathbf{q}_p^n + \Delta t \mathbf{L}(\mathbf{q}_p^n), \tag{3.29}$$

$$\mathbf{q}_{p}^{n+1} = \frac{1}{2}\mathbf{q}_{p}^{1} + \frac{1}{2}\mathbf{q}_{p}^{n} + \frac{1}{2}\Delta t \mathbf{L}(\mathbf{q}_{p}^{1}). \tag{3.30}$$

The Courant-Frederich-Levy (CFL) stability condition of the DG method requires that $CFL = c\Delta t/\Delta x \approx 1/(2p-1)$, where p is the order of the basis function. Due to the time-step restrictions that are imposed by the explicit RKDG and the presence of high and low frequency oscillations in the two-fluid plasma model and implicit time-stepping scheme is appealing.

3.7 Continuous and Discontinuous Galerkin Couple Through Source Terms

Both the CG and a DG methods provide good coupling between the sources and the fluxes since neither is a split method. Therefore, the DG and CG representations only couple through the treatment of the source terms. The balance law equations for the ions and neutrals $(q_n = 0)$ are given as

$$\frac{\partial \mathbf{Q}_{i}}{\partial t} \begin{bmatrix} \rho_{i} \\ \rho_{i} \mathbf{u}_{i} \\ \varepsilon_{i} \end{bmatrix} + \frac{\partial}{\partial \mathbf{x}} \begin{bmatrix} \rho_{i} \mathbf{u}_{i} \\ (\rho_{i} \mathbf{u}_{i} \mathbf{u}_{i} + p_{i} \stackrel{\longleftrightarrow}{\mathbf{I}}) \\ (\varepsilon_{i} + p_{i}) \mathbf{u}_{i} \end{bmatrix} = \underbrace{\begin{bmatrix} \mathbf{S}_{i}(\mathbf{Q}_{i}, \mathbf{Q}_{em}) \\ 0 \\ \frac{\rho_{i}q_{i}}{m_{i}} (\mathbf{E} + \mathbf{u}_{i} \times \mathbf{B}) \\ \frac{\rho_{i}q_{i}}{m_{i}} \mathbf{u}_{i} \cdot \mathbf{E} \end{bmatrix}}_{(3.31)$$

where the *em* subscript denotes the electromagnetic fields variables.

For the evolution of the electron fluid and the electromagnetic fields, the divergence of

the flux term in the balance law is replaced by the product of the flux Jacobian and the spatial gradient of the conserved variables. The evolution equation for the electron fluid is then expressed as

$$\frac{\partial \mathbf{Q}_{e}}{\partial t} \begin{bmatrix} \rho_{e} \\ \rho_{e} \mathbf{u}_{e} \\ \varepsilon_{e} \end{bmatrix} + \frac{\partial \overrightarrow{\mathbf{F}}}{\partial \mathbf{Q}} \cdot \frac{\partial}{\partial \mathbf{x}} \begin{bmatrix} \rho_{e} \\ \rho_{e} \mathbf{u}_{e} \\ \varepsilon_{e} \end{bmatrix} = \underbrace{\begin{bmatrix} \mathbf{S}(\mathbf{Q}_{e}, \mathbf{Q}_{em}) \\ \mathbf{Q}_{e} \mathbf{Q}_{em} \\ \rho_{e} \mathbf{q}_{e} \\ \frac{\rho_{e} q_{e}}{m_{e}} (\mathbf{E} + \mathbf{u}_{e} \times \mathbf{B}) \\ \frac{\rho_{e} q_{e}}{m_{e}} \mathbf{u}_{e} \cdot \mathbf{E} \end{bmatrix}}, (3.32)$$

where the flux Jacobian can be expressed in terms of electron fluid variables, and

$$\frac{\partial \overrightarrow{\mathbf{F}}_{e}}{\partial \mathbf{Q}} = \begin{bmatrix}
0 & 1 & 0 & 0 & 0 \\
-u^{2} + \frac{(\gamma-1)}{2}(u^{2} + v^{2} + w^{2}) & (\gamma+3)u & -(\gamma-1)v & -(\gamma-1)w & \gamma-1 \\
-uv & v & u & 0 & 0 \\
-uw & w & 0 & u & 0 \\
-uw & w & 0 & u & 0 \\
-\frac{(e+p)u}{\rho} + \frac{u}{2}(u^{2} + v^{2} + w^{3}) & \frac{e+p}{\rho} - u^{2} & -(\gamma-1)uv & -\gamma uw & \gamma u
\end{bmatrix}, \tag{3.33}$$

where $\mathbf{u}_e = u\hat{x} + v\hat{y} + w\hat{z}$ and the *e* subscript has been omitted for clarity. The field evolution equations in one-dimension are

The Maxwell equation flux Jacobian is different for each direction. The coupling between the CG and DG is done through the source terms, where integrals are evaluated using the same Gauss-Legendre quadrature rules for all fluid.

3.8 General Implementation Details

The BFEM method is implemented in the Washington Approximate Riemann Plasma Solver (WARPX), described in appendix (B), which is a partial differential equations solver, focused mainly on hyperbolic equations, but can handle any equation systems.

3.8.1 Continuous Galerkin Matrix Assembling

The implementation is done using the Portable Extension Toolkit for Scientific Computation [61] (PETSc) and the Scalable Nonlinear Equations Solvers (SNES) are used for the implicit time advance. PETSc has the capability of managing all the data communication between different processors and can build massively parallel matrices.

The use of matrices is needed for the implementation of the CG discretization and the implicit time integration described by Eq. (3.25). The element mass matrix is the same for every element since the implementation is done on a structured grid. The evaluation of the element mass matrix integral, Eq. (3.7), is done using Gauss-Legendre quadrature rules

where lagpol is the Lagrange polynomials evaluated at the quadrature locations, w is the weights and Je is the determinant of the Jacobian of transformation. After the element matrix has been evaluated, the global mass matrix, $\overrightarrow{\mathbf{M}}$, can be built in PETSc using the following commands

```
MatCreate(comm.getMpiComm(),&MassM);
MatSetSizes(MassM,numUnknowns,numUnknowns,totNumUnknowns,totNumUnknowns);
MatSetType(MassM,MATMPIAIJ);
MatSetFromOptions(MassM);
MatMPIAIJSetPreallocation(MassM,nr,PETSC_NULL,nr_off,PETSC_NULL);
```

where numUnknowns is the number of unknowns in a given processor, which corresponds to the number of nodes multiplied by the number of conserved variables at each. And totNumUnknowns is the total number of unknowns for the entire problem. The number of non-zeros for each row is set by the parameter nr. The element to global matrix mapping is done according to Eq. (3.14),

where meqn is the number of component or conserved variable at each node. The element dissipation matrix, Eq. (3.11), is built similarly

De[i][j]
$$+=$$
 _quad->w(gl)*_quad->dlagpol(i,gl)*_quad->dlagpol(j,gl)*1./Je; where $dlagpol$ is the derivative of the Lagrangian polynomials evaluated at the quadrature point.

3.8.2 PETSc Matrix-Free Methods for Implicit Time Integration

Implicit time integration requires the evaluation of the Jacobian matrix, but this can be done without formally building a matrix by instead evaluating the matrix-vector multiplication as

$$\overrightarrow{\mathbf{J}}(\mathbf{Q}^n)\mathbf{a} = \frac{\partial \mathbf{G}(\mathbf{Q}^n)}{\partial \mathbf{Q}^n}\mathbf{a} = \frac{\mathbf{G}(\mathbf{q}^n + h + \mathbf{a}) - \mathbf{G}(\mathbf{q}^n)}{h}$$
 (3.35)

where h is a small value computed internally by PETSc and G is the residual function given by Eq. (3.25). A matrix coloring [62] is needed to efficiently evaluate the matrix-vector

```
product. The matrix coloring is done as following
unsigned value = blockSize-_meqn;
for (int i=0; i<_numElem; ++i) {
       int imin = (i==0)? 0 : (i-1)*value;
       int imax = (i = numElem - 1) ? numUnknowns : i*value+blockSize+value - 1;
       for (int k=0; k<blockSize; ++k) {
         int jr = i*value + k;
         // set non-zero elements to 1.0
         for (int jc = imin; jc < imax; ++jc) {
           MatSetValue(color, jr, jc, 1.0, INSERT_VALUES);
       }
where numElem is the total number of elements and blockSize = megn \times (number of node sperelement).
Once the matrix color has been populated, a coloring object is create
MatGetColoring (jacobian, MATCOLORINGSL, &iscoloring);
the a finite different coloring is created using
MatFDColoringCreate(jacobian, iscoloring, &matFDColoring);
and the function evaluation G for the finite different approximation is done using
MatFDColoringSetFunction(matFDColoring,
         (PetscErrorCode (*)(void)) WxFemPetscSnesSolver::evaluateFunction,
         (void *) cls);
finally set Jacobian evaluation function as
SNESSetJacobian (solver, jacobian, jacobian,
         SNESDefaultComputeJacobianColor, matFDColoring);
the non-linear problem is solved by invoking the command
```

SNESSolve(solver, PETSC_NULL, solVector);

where solver is the nonlinear solver object and solVector is the solution vector.

3.8.3 Continuous Galerkin Boundary Conditions

The boundary conditions are implemented using the penalty method which guarantees that the matrices remain symmetric. For an $\overrightarrow{\mathbf{A}}\mathbf{u} = \mathbf{F}$, a boundary on node zero $u_0 = g_0$ would be implemented by

$$\overleftrightarrow{\mathbf{A}}_{00} \Rightarrow \overleftrightarrow{\mathbf{A}}_{00} + \alpha \tag{3.36}$$

$$F_0 \Rightarrow F_0 + \alpha g_0. \tag{3.37}$$

where α is a large value added to the diagonal of the matrix and the right-hand-side vector. For this implementation the penalty method is applied to the mass, $\overrightarrow{\mathbf{M}}$ Eq. (3.7), and the dissipation, $\overrightarrow{\mathbf{D}}$ Eq. (3.11), matrices.

3.8.4 Discontinuous Galerkin Boundary Conditions

For the DG portion of the BFEM, the boundary conditions are imposed through ghost cells, where Dirichlet and Neumann boundary conditions can be imposed. Note that this boundary values are applied to the expansion coefficients which depend on the polynomial order being used. For example, to implement Dirichlet value of zero, the coefficients of all even basis functions are set to the negative of the adjacent domain cell, and the coefficients of all odd basis functions in the ghost cells remain the same as the adjacent domain cell.

3.8.5 Discontinuous Galerkin Limiters

The DG method uses limiters around sharp gradients and discontinuities. Limiters can be applied to either the conserved or the characteristic variables depending on the limiter. The implementation of limiters was done by Srinivasan in Ref. [23].

3.9 Summary

A new numerical method, blended finite element method (BFEM), has been introduced for the multi-fluid plasma model. A continuous Galerkin finite element method is used to discretize the electron fluid and the electromagnetic fields, and a discontinuous Galerkin finite element method for the all ion and neutral fluids. The method is higher order accurate in space and second order in time. The electron fluid and the electromagnetic fields time evolution is computed implicitly, which reduces the most stringent time limitation of the multi-fluid plasma model. The shock capturing propertied of the discontinuous Galerkin method are ideal at resolving the discontinuities of the ion and neutral fluids, which are the fluids that do shock. The result is a method that is robust, accurate, and can resolve physical aspects of the plasma without introducing numerical noise.

Chapter 4

VALIDATION AND VERIFICATION OF THE BLENDED FINITE ELEMENT METHOD

4.1 1-D Advection Equation: Convergence Studies

In Ref. [23] the linear advection equation was used to study the spatial and temporal convergence of the solution versus the polynomial order used in a discontinuous Galerkin method. The problem is the simplest of hyperbolic equations, does not have any source terms, and is linear, which restricts the accuracy of the solution solely to the numerical method. The one-dimensional linear advection equation is given as

$$\frac{\partial Q}{\partial t} + \frac{\partial Q}{\partial x} = 0. {(4.1)}$$

The pulse is initialized to a Gaussian given as $Q(x,0) = e^{-10(x-2)^2}$ on a domain size of $x \in [0,10]$. The pulse is propagated from x=2 to x=8 (a total time interval of $\Delta T=6$) and compared to the analytical solution given as $Q(x) = e^{-10(x-8)^2}$. The error in the numerical solution is calculated by evaluating the L_2 -norm as

$$||\Delta Q||_2 = \sqrt{\frac{1}{n} \sum_{i=1}^{n} (\hat{Q} - Q_i)^2}.$$
 (4.2)

where \hat{Q} is the analytical solution and Q_i is the numerical solution. The subscript i represents the summation is done over the quadrature points for the DG method and the nodal values for the CG case, and n is the total number of nodes or quadrature points.

Figure 4.1 shows the L_2 -norm for the advected pulse using a fixed $\Delta t = 0.00125$ with different polynomial interpolation functions for the DG and the CG methods. The fixed time steps isolates the convergence effect to the spatial order. The plot shows that, for equivalent order polynomial interpolation functions, the CG and DG methods converges at the same

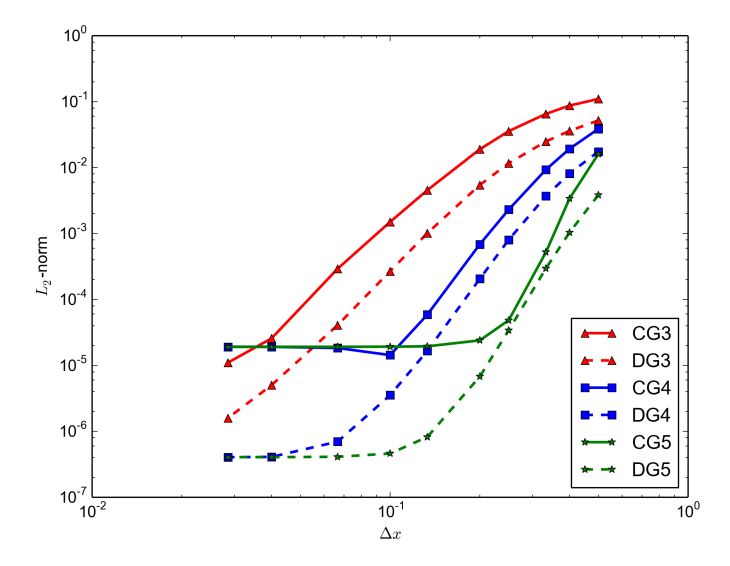


Figure 4.1: Log-log plot of the L_2 -norm as a function of Δx for the linear advection problem using a fixed time step of $\Delta t = 0.00125$ and spatial orders 3, 4, and 5 for the CG and the DG schemes. The κ value for the artificial dissipation is 10^{-7} . The linear portion of each line has a slope that corresponds to the order of accuracy of the numerical method. Both methods converge as expected.

rate, i.e. the linear portion of the curve have the same slope. The CG scheme L_2 -norm plateaus around 10^{-5} , which is due to the artificial dissipation. The artificial dissipation decreases the peak of the Gaussian every time-step and over the interval $\Delta T = 6$ the peak for all cases has decreased by the same amount.

Figure 4.2 shows the calculated L_2 -norm for the advection problem using a fixed CFL number of CFL = 1.0. For each spatial order, the time-step is given as $\Delta t = CFL\Delta x$. This isolates the rate of convergence to the temporal order of accuracy of the time-stepping method. For the CG a θ -method is used with $\theta = 0.5$, which is the Crank-Nicholson method that is second-order accurate, and for the DG a second-order TVB Runge-Kutta time integration is used, which is also second-order accurate. The slope of the lines for both method is two, i.e. for every decade decrease in Δx there are two decades decrease in the L_2 -norm. Therefore, the desired temporal converge is attained by the time-stepping methods.

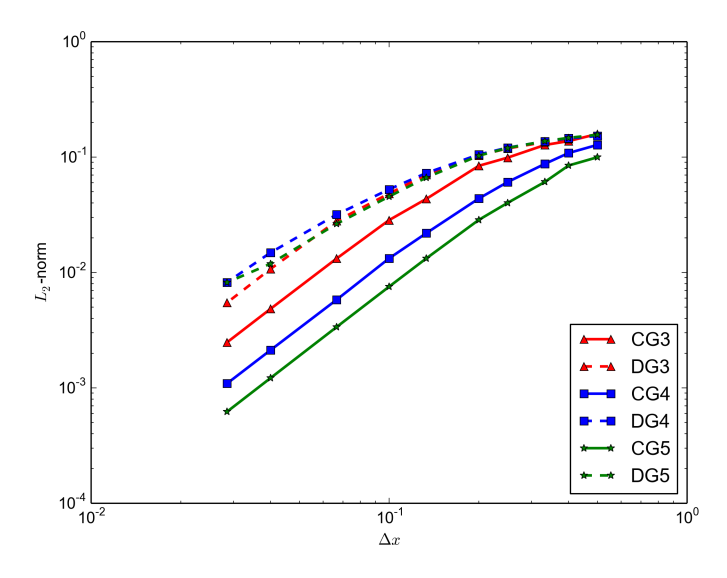


Figure 4.2: Log-log plot of the L_2 -norm as a function of Δx for the linear advection problem using a fixed CFL=1 and spatial orders 2, 3, and 4 for the CG and the DG schemes. The κ value for the artificial dissipation is 10^{-7} . All of the lines have a slope of two corresponding to the temporal order of accuracy of both the CG and DG section of the BFEM method.

4.2 Two-Fluid Plasma Soliton in 1-D: Accuracy and Timing Studies

A one-dimensional soliton propagation [63] is modeled using the multi-fluid plasma model. This problem is used to study the accuracy and compare the computational cost of the BFEM and the DG method. This problem is chosen because it describes a multi-fluid plasma composed of one electron and one ion-fluid, and is one the simplest problems that can be solved using the BFEM. In addition, the solution of the problem is smooth, which permits the use of small values of artificial dissipation for BFEM, eliminating the inaccuracies associated with the artificial dissipation, as seen in the previous section.

The problem in this section solves the ideal multi-fluid plasma model described in Sec. 2.5. The initialized for the z-component of the magnetic field is $B_z = 1.0$, the temperature (T = p/n), where n is the number density $n = \rho/m$ is $T_e = T_i = 0.01$, $\mathbf{u}_i = \mathbf{u}_e = \mathbf{0}$, q = 1, and $n_e = n_i = 1.0 + e^{-10(x-6)^2}$ on a domain $x \in [0, 12]$. The ratio of specific heats is $\gamma = 2$. The simulation uses 512 second-order elements for DG and BFEM.

Table 4.1: Total computing time elapsed and time savings for a simulations using a fully DG method, compared to one using the BFEM for different values of electron-to-ion mass ratio and the speed-of-light to the ion sound speed.

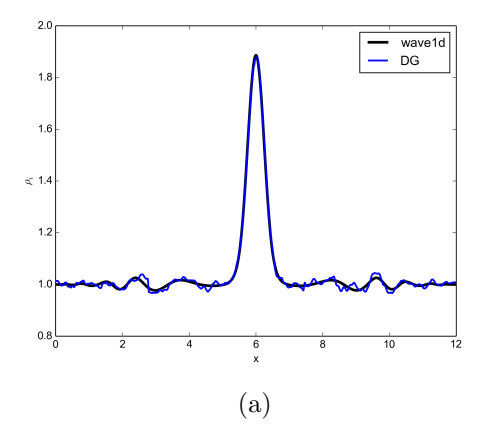
case	m_i/m_e	c/c_{si}	DG time(s)	BFEM time (s)	BFEM cost over DG
1	25	$10\sqrt{2}$	1.176	87.56	+7345%
2	1836	85.70	343.2	317.5	-7.488%
3	1836	1000	4487	3948	-12.02%

The purpose of this problem is to quantify the computational cost, and to show when the BFEM is more advantageous over a explicit DG method. The problem has smooth variables which makes it easier for the implicit portion of the BFEM to converge to a solution in fewer Newton iterations. The artificial dissipation coefficient κ in Eq. (3.9) is small, $\kappa = 10^{-10}$.

It is common practice in plasma simulation to artificially decrease the ion-to-electron mass ratio as well as the speed-of-light to ion sound speed ratio. This is done to decrease the time restriction otherwise imposed by the speed-of-light and the plasma frequency. However, this could affect the physics of the problem in certain cases. In this section, we calculate the computational savings of the BFEM over the DG method when using physical values for the mass ratio and the speed-of-light to ion sound speed ratio.

Table 4.1 shows the computational time needed to advance the solution from normalized time t = 0 to t = 1 for different mass ratios and the speed-of-light. Initially, for a mass ratio of 25, the DG method is immensely faster than the BFEM, however as the mass ratio and speed-of-light to ion sound speed ratio approach realistic values, the BFEM computational time becomes less than the DG method.

In Fig. 4.3 the DG and BFEM ion densities using 512 second-order elements, at t = 40, are compared to a converged finite volume wave propagation method[42] (wave1D) solution at using 5000 cells. The problem is initialized using the conditions described in case (3) of Table 4.1. The DG solution has a large amount of dispersion which appears when a realistic mass ratio is used. The BFEM has a higher peak value than the other methods because both the DG and FVM are dissipative. The dissipation in the BFEM method comes from



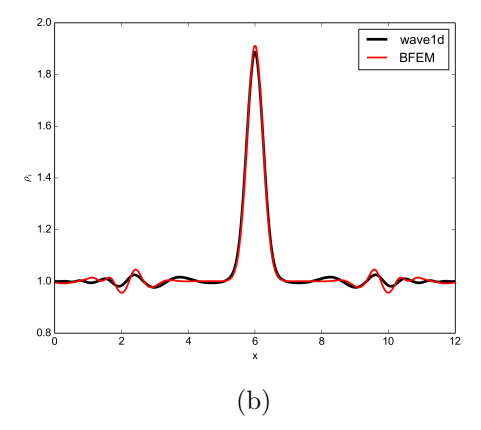


Figure 4.3: Ion density fluctuations propagate from the center of the domain towards the boundaries. The DG and BFEM solutions using 512 second-order elements are compared to a converged finite volume solution of 5,000 cells at t = 40. Both methods resolve the oscillations of the problem, but there is some phase errors associated with the BFEM.

the artificial dissipation term, Eq. (3.9), but for smooth solutions, the value of κ can be small, $\kappa = 10^{-10}$.

Figure 4.4 plots the evolution over time of the L_2 -norm of the relative error for the DG and BFEM. The error is defined as

$$error = \frac{\rho_i^k - \rho_i^c}{\rho_i^c} \tag{4.3}$$

where ρ_i^c is the mass density for the converged solution and ρ_i^k represents the solution given by the DG or BFEM. The error is evaluated at each quadrature point (DG) or the nodal values (BFEM). The DG error L_2 -norm is lower than the BFEM one, but the error is only on the order of about $\sim 1.5\%$ of the converged solution using a resolution of onetenth. Therefore, it is an acceptable error for the computational saving attained. The source of the error is the fact that DG and converged solution are obtained using a explicit time integration which resolves the electron plasma frequency, while the BFEM does not resolve the electron plasma frequency. Figure 4.5 compares the L_2 -norm for a case where the electron-to-ion mass ratio is one, and for that case the error for both methods is comparable

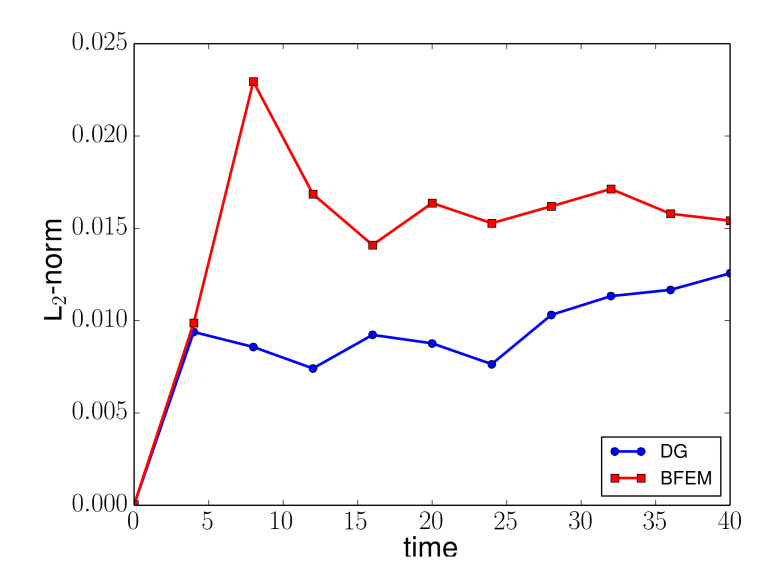


Figure 4.4: L_2 -norm of error the DG and the BFEM over time. The DG method error norm is lower than the BFEM one, but the error is only about 1.5% of the converged solution.

because the electron and ion plasma frequency are the same, and the time-steps for both simulations is the same. The BFEM is less computationally costly than the DG method for problems where realistic ion-to-electron mass ratios and/or speed-of-light to ion sound speed are used. In this problem ion-to-electron mass ratio of 1836 is assumed, which is the case for an hydrogen plasma, but for fusion plasmas, namely deuterium and tritium plasma that ratio is higher, which would make the explicit time-step more restrictive. Therefore, for fusion plasmas the BFEM produces more computational cost savings over the DG method than shown here.

4.3 The Electromagnetic Plasma Shock Problem

The blended finite element method is applied to a two-fluid version of the electromagnetic plasma shock [64] as presented in Refs. [23, 21]. The electromagnetic plasma shock problem is a good test for the multi-fluid plasma algorithm because both MHD-like behavior and multi-fluid effects can be modeled by changing the Larmor radius, r_L . In the MHD limit $r_L \to 0$, and multi-fluid effects become relevant as the Larmor radius becomes comparable

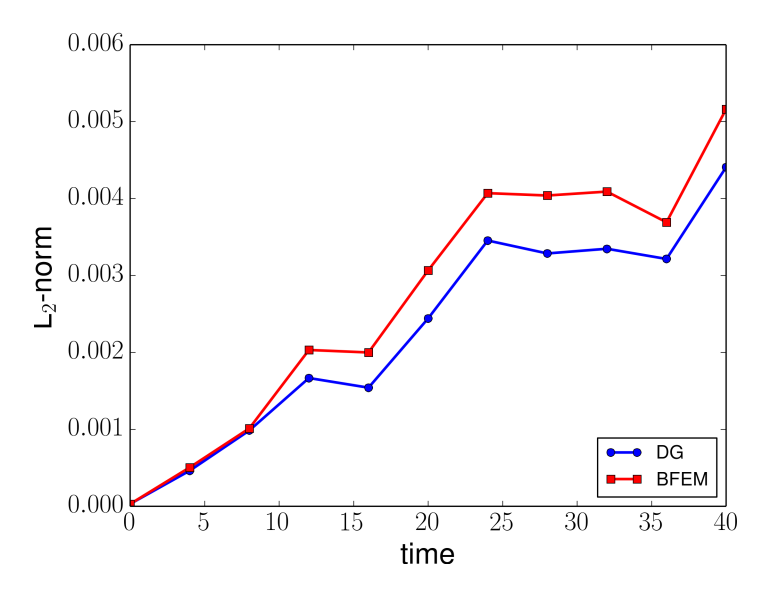


Figure 4.5: L_2 -norm of error the DG and the BFEM over time for a case where $m_i/m_e = 1$. The DG and BFEM L_2 -norms are the same because both simulations have the same time-step and the electron plasma frequency is resolved.

to the scale length of the problem. For Larmor radius comparable to the domain size, the electron fluid couples to the magnetic field and the solution contains wave-like structures that propagate faster than MHD waves, and can be seen in Fig. 4.6.

The electromagnetic plasma shock is an initial boundary value problem with a discontinuity in the variables such that half of the domain is at one state and the other half is at another state. For the test case presented here, $m_i/m_e = 1836$. The problem is described in detail in [1]. The solution features are shown in Fig. 4.6. From left to right they are, a fast rarefaction wave (FR), a slow compound wave (SC), a contact discontinuity (CD), a slow shock (SS), and another fast rarefaction wave (FR).

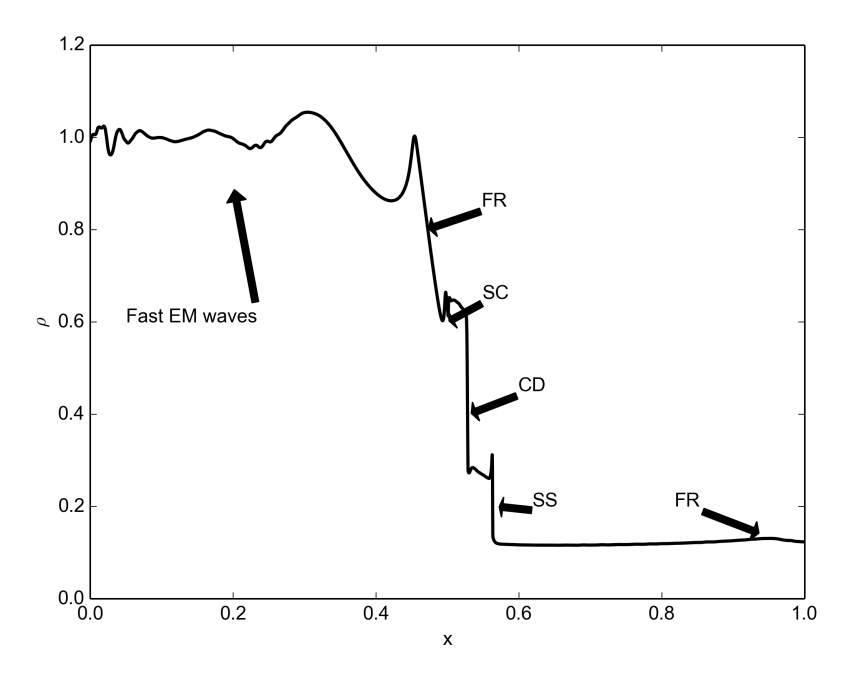


Figure 4.6: The features of the electromagnetic plasma shock are a fast rarefaction wave (FR), a slow compound wave (SC), a contact discontinuity (CD), a slow shock (SS), and another fast rarefaction wave (FR). The solution also shows fast electromagnetic waves that propagate faster than MHD waves[1].

The two-fluid equivalent initial conditions for the electromagnetic plasma shock are

The parameters used for the problem are obtained from Ref. [1], and are $c/u_0 = 110$, $\delta = 1$, $r_L = 0.73$, $\gamma_e = \gamma_i = \frac{5}{3}$ and the ion-to-electron mass ratio is $m_i/m_e = 1836$. A grid resolution of 512 second order elements is used. Time is normalized as $\tau_c = \frac{1000r_L}{c}$.

The blended finite element method is compared to a discontinuous Galerkin (DG) implementation[21] and to a wave propagation method finite volume (FV) methods[42]. Figure 4.7 shows the mass density profile for all three methods and there is good agreement between all of them. The BFEM smoothed the oscillations in the problem, which is due to the artificial dissipation and is discussed in more detail in Sec. 4.3.2.

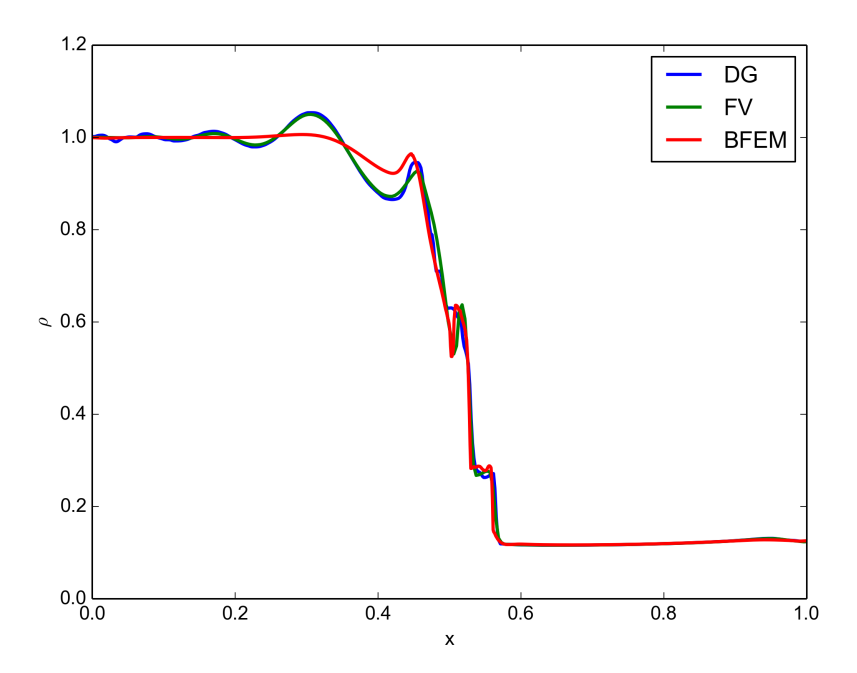


Figure 4.7: The total mass density is plotted for the electromagnetic plasma shock problem at $t=0.05\tau_c$. The main features of the problem are captured by all three methods, but the BFEM does not resolve the EM waves properly, which maybe due to the artificial dissipation in the method.

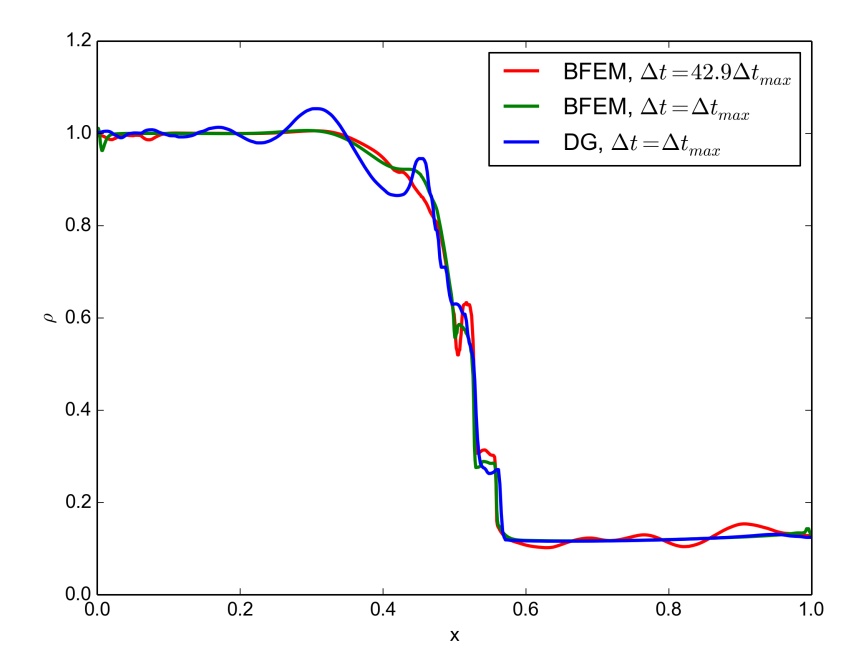


Figure 4.8: The total mass density is plotted for the electromagnetic plasma shock problem at $t=0.05\tau_c$. The results were obtained using different Δt . Δt_{max} corresponds to the maximum value allowed for an explicit methods and for this problem $\Delta t=42.9\Delta t_{max}$ is the maximum value allowed by the semi-implicit BFEM, where the ion dynamics restricts the time-step.

Table 4.2: Characteristic speeds and frequencies for the electromagnetic shock problem.

	electron	ion
c_s	0.39115	0.00912
ω_{cs}	183.6	0.1
ω_{ps}	428.48	10
c = 1		

4.3.1 Implicit and Explicit Time Integration Comparison

The CFL condition of the multi-fluid plasma model is dependent on the characteristic speeds of the system, the species speed of sound, Eq. (2.40), and the speed of light, c. Moreover, the problem must also resolve the cyclotron, $\omega_{cs} = \frac{q_s B}{m_s}$, and plasma, $\omega_{ps} = \sqrt{\frac{n_s q_s^2}{\epsilon_o m_s}}$, frequencies for the different species. For the initialization parameters used here, these values are shown in Table 4.2. Therefore the maximum explicit time step is determined by the following expression,

$$\Delta t_{max} = \min\left(\frac{\Delta x}{c_{se}}, \frac{\Delta x}{c_{si}}, \frac{\Delta x}{c}, \frac{0.1}{\omega_{ce}}, \frac{0.1}{\omega_{ci}}, \frac{0.1}{\omega_{pe}}, \frac{0.1}{\omega_{pi}}\right). \tag{4.5}$$

The electron plasma frequency produces the most restrictive time-step, $\Delta t_{max} = 2.33 \times 10^{-4}$. In BFEM the electron fluid is advanced implicitly, so the time step restrictions are dependent on the ion fluid, which are less stringent than the explicit case (DG and FV).

Fig. (4.8) compares the mass density solution for BFEM using an explicit time step $(\Delta t = \Delta t_{max})$ against an implicit one $(\Delta t = \sqrt{m_i/m_e}\Delta t_{max} = 42.9\Delta t_{max})$. The implicit time step is limited by the ion plasma frequency. The solution attained using the implicit Δt resolves all the main features of the problem except the fast rarefaction wave, which should be ahead of the slow shock, but instead there are small oscillation ahead of the SS. The compound wave is also more prominently resolved in this case.

4.3.2 Effects of Artificial Dissipation

In Eq. (3.9) an artificial dissipation term was added to the hyperbolic equations to dampen high frequency oscillations (Gibbs phenomena) in regions of sharp gradients. The parameter

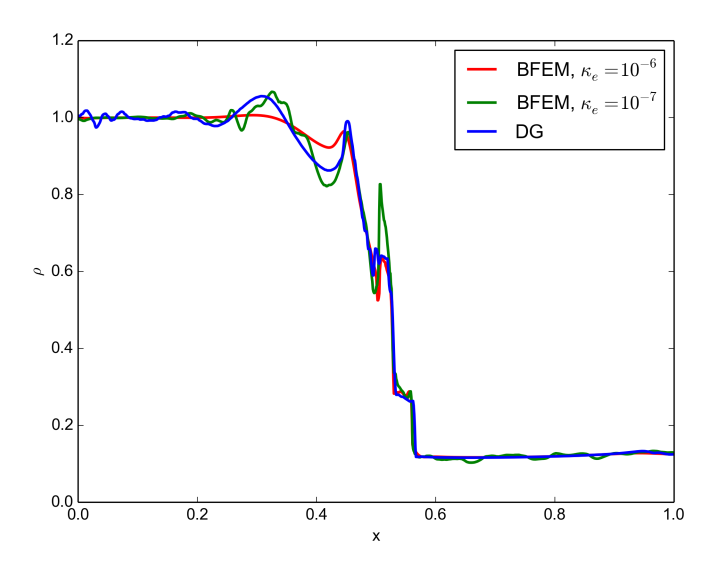


Figure 4.9: Mass density plot comparing two cases where the electron fluid artificial dissipation, κ_e , is decreased by a factor of 10, with the DG method. The solution for the lower artificial dissipation captures the wave-like behavior better. The compound wave spikes up in amplitude, and the right rarefaction wave is not visible.

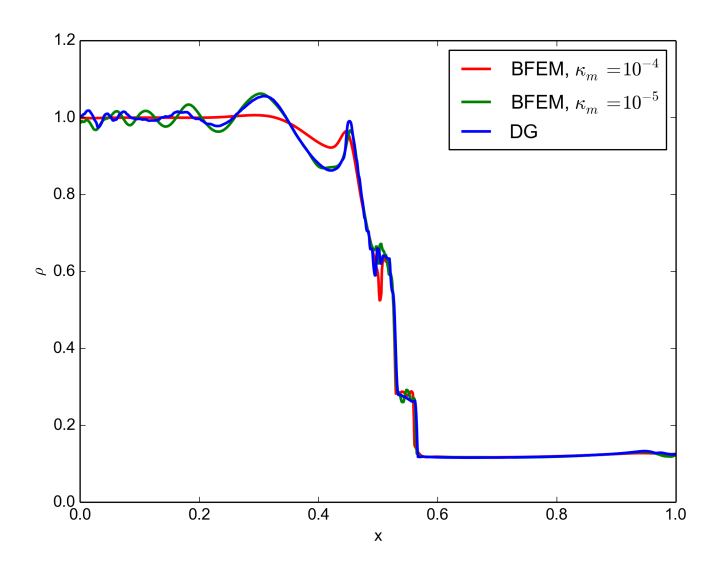


Figure 4.10: Mass density solution comparing two BFEM cases where the electromagnetic fields artificial dissipation is decreased by a factor of 10. The reduced dissipation solution agrees better with DG solution, reinforcing the point that the wave-like behavior arises from the interaction of the electron fluid with the electromagnetic fields.

 κ was introduced to scale the amount of artificial dissipation on the physics of the problem. There are no guidelines on how to pick a value for κ . If it is too small the solution will have high amplitude node-to-node oscillations that grow over time, making the solution of the nonlinear Newton solver more stiff and hard to converge. On the other hand, if κ is too big the solution will smooth out all the relevant features of the problem producing an inaccurate result.

In the BFEM the artificial dissipation is applied only to the electron fluid variables and the electromagnetic field equations. It is possible to apply different values of κ for the two equation system separately.

In Fig. 4.9 the effects of the artificial dissipation on the electron fluid equations is studied. There, it can be seen that reducing the value of κ from 10^{-6} to 10^{-7} makes the compound wave more distinct and the oscillations due to charge separation and fast waves are more visible. However, the solution is out of phase with the DG result and the second FR wave is not resolved. Small oscillation appear superimposed onto the larger wavelength fast electromagnetic waves.

Decreasing the artificial dissipation in Maxwell's equations resolves the oscillations due to species separation and the phase shift is less visible in the solution in Fig. 4.10. In addition, in this case the fast rarefaction wave is resolved properly. In this case there is remarkable agreement between the BFEM and the DG solutions. In conclusion, the artificial dissipation plays an important role in the accuracy of the BFEM. It might be prudent to investigate better forms of calculating the parameter κ or different forms of artificial dissipation.

4.4 Summary

The DG and CG schemes converge according to the theoretically predicted values. The order of the accuracy of the scheme depends on the polynomial order of the interpolation function chosen. Both time-stepping methods are second-order accurate in time. The BFEM is less computationally expensive when realistic values of the ion-to-electron mass and speed of light to ion sounds speed ratios are used. For problems where the electron dynamics can be ignored the results produced by the BFEM are comparable to the DG method. The artificial dissipation can affect the results considerably, therefore it needs to be tuned in

order to resolve physical oscillations in the problem while damping numerical dispersion.

Chapter 5

INERTIAL CONFINEMENT FUSION FUEL SPECIES SEPARATION

5.1 Introduction

In inertial confinement fusion (ICF) experiments a spherical capsule is compressed to high densities and pressures using a laser driver. The capsule is filled with deuterium and tritium ice (DT-ice). Fusion is achieved when the plasma has reached ion temperatures greater than 10 keV and an areal density greater than 0.3 g/cm²[65].

One of the products of the fusion reaction is neutrons. Neutron energies are measured to identify what fusion reactions are occurring, and to quantify the reaction rates by counting the number of neutrons produced per unit time. In Ref. [25] the authors measured the neutron yield of an ICF pellet using direct drive at the OMEGA facility and found that the DT reaction yield was lower than expected, which was in line with the results in Ref. [66] where the neutron yield was 50% lower than expected. They attributed this yield reduction to fuel stratification caused by baro-diffusion[67] (pressure gradient-driven diffusion), which leads to the separation of the deuterium and the tritium during the implosion. Thermo-diffusion[68] and electro-diffusion[69] have also been suggested to cause ICF fuel separation.

After large electric fields were inferred during ICF capsule implosions, it was proposed in Ref. [65] that the presence of these fields could produce significant amount of baro-diffusion in ICF capsules implosions. The baro-diffusion is localized to regions of sharp gradients and electric fields have formed [67]. The baro-diffusion argument is that, in a DT plasma, the deuterium will experience a larger acceleration than the tritium because of its larger charge-to-mass ratio. The deuterons will move closer to the region where the electric field is large, and in the process shield the tritons from experiencing the same field intensity. The deuterium shielding of the electric field has the effect of compounding the two species separation.

Three main candidates have been proposed for the origin of the electric field in the ICF

pellets[65]. The first candidate is electron pressure gradient caused by the acceleration at the pusher-fuel interface and also by ionization gradients. The second candidate is simple charge separation caused by the fact that electrons have a lower mass and accelerate ahead of the ions generating electric fields. And the third candidate is concentration driven diffusion of the electrons ahead of the ion shock creating an electric field. Of these three mechanisms, only the third one predicts field values the same order of magnitude as the inferred values from experimental results[25].

Challenges in theoretically predicting this electric field and observing the deuterium-tritium separation can be attributed to the fact that ICF capsule implosions are generally modeled using radiation-hydrodynamic (rad-hydro) codes which are single fluid, mass averaged, and charge neutral [10]. Rad-hydro codes are adequate when modeling hydrodynamic instabilities that develop in ICF capsules; however, species separation is inherently a multifluid effect and generation of local electromagnetic fields precludes the use of the MHD model [17] because it assumes charge neutrality.

ICF fuel species separation have been modeled using a hybrid-PIC code in Ref. [70], where the authors analyzed the effects that the charge-to-mass ratio had on ion separation. For the ICF relevant case, DT plasmas, the separation was less than the cases with ionization of two and an ion mass ratio of ten. In spherical geometry the authors found that the yield was highly dependent on the choice of heat flux limiter for the free streaming heat flux model used [36]. However, there was no comparison of the multi-fluid results with a single fluid averaged atom to study if the current ICF codes are correctly predicting the neutron yield.

Ion Vlasov-Fokker-Planck(VFP) simulations were performed recently in Ref. [71] where the authors compared the results of a two-ion species simulation with one of a single ion species simulation. They found that the temperature and density at the stagnation phase of the ICF implosion for the two-ion species were higher than the one predicted by a average atom radiation hydrodynamic code. In addition, the yield rate, number of neutrons produced per unit time, for the two-ion fluid was higher that the single-ion simulation. However, the authors do not make any references to electric field, in the simulations or what causes the separation.

In this dissertation the multi-fluid plasma model (MFPM) is used because it resolves charge separation with high fidelity and can generate large local electric fields. During the derivation of the MFPM local thermodynamical equilibrium within each species was assumes, which implies that there is high collisionality within each species (intra-species collisions), but the model allows for lower collisionality between different species, inter-species collision. The collisionality is quantified by the Knudsen number deined by, Eq. (2.28), high values imply low collisionality (kinetic plasma), and low values imply a highly collisional plasma where the fluid assumption is appropriate. A Knudsen number to validate a fluid assumption is generally taken to $\text{Kn} \leq 10^{-2}$. In the simulations presented in this research, each species is assumed to be a fluid, so the intra-species Knudsen number is always assumed low. Henceforth, whenever the Knudsen number is mentioned it refers to the inter-species collisionality.

The model is implemented using the Blended Finite Element Method (BFEM) as described in Ch. 3. The results of a single-ion fluid is compared to a two-ion species simulation to study the effects that the separation on the neutron yield. The advantage of the multifluid plasma model is that it is computationally less expensive than the VFP model, which often require small time-steps to resolve the electron dynamics. The electron fluid and full Maxwell equations are evolved implicitly, which relaxes the time-step limitations. The MFPM is also less restrictive than the MHD model[17]. In the MFPM the electron inertia is not zero and there is an assumption of a finite speed-of-light. Therefore, the MFPM is at the optimal position between computational effort required and the relevant physics that is needed to simulate ICF species separation.

5.2 Planar Geometry Results

The problems presented in this section are obtained from Ref. [70]. The multi-fluid plasma model used in the simulations are shown in Sec. 2.4 (non-dimensional form). In order to compare the results obtained here with the ones given in Ref. [70], viscosity is assumed to be zero, and the free-streaming limit heat flux is assumed. The Cartesian geometry problems

are initialized as

$$\begin{cases} x < 0 \ \mu\text{m} : & \sum_{i} n_{i} = 4 \times 10^{19} \text{ cm}^{-3}; \quad T = 100 \text{ eV} \\ x > 0 \ \mu\text{m} : & \sum_{i} n_{i} = 1 \times 10^{19} \text{ cm}^{-3}; \quad T = 10 \text{ eV} \end{cases}$$
(5.1)

where the subscript i denotes all the ion species. The plasma is initially assumed to be charge neutral everywhere, $n_e = \sum_i Z_i n_i$, and the heat flux is zero. The Knudsen number is calculated using the ion thermal speed and the ion-ion collision frequency, $\mathrm{Kn}_i = 0.8$. The only non-ideal terms considered are the momentum transfer and the thermal equilibration terms, the heat flux is set to zero as well as the viscosity. The computational domain is $\mathrm{x} \in [-30~\mu\mathrm{m},~30~\mu\mathrm{m}]$, and zero normal gradient boundary condition are applied at $\mathrm{x}=-30~\mu\mathrm{m}$ and $\mathrm{x}=30~\mu\mathrm{m}$.

The goal is to analyze how ions of different mass and ionization levels separate if initialized to the same conditions. Fig. 5.1 shows the density profile of a multi-fluid plasma in Cartesian geometry. The plasma has three constituents, two-ion species and electrons. It can be seen that the separation between the ion species is dependent on the charge-to-mass ratio, $\mu = m_i/m_p$, where m_i is an ion mass and m_p is the proton mass. An increase in the ionization level, Z = q/e, from Fig. 5.1(a) to 5.1(b) decreases the species separation. This points to the role that electric fields have in the separation for this particular case. The increase in the ionization level causes the force generated by the electric field to double and leads to a larger acceleration of the heavier fluid. From Fig. 5.1(a) to 5.1(c) a decrease in the mass difference between the two ions causes the species separation to decrease. When the heavier fluid's mass is decreased, two effects are observed: its speed-of-sound increases, making the shock front propagate faster; and its acceleration due to the electric field increases.

High collisionality drives the two ion species to a common equilibrium state. In Fig. 5.1(d) a high collisionality multi-fluid plasma simulation is compared to a single-fluid averaged mass plasma under the same conditions. The single-fluid approximation is valid only if there is high collisionality between the species. However, during the capsule implosion

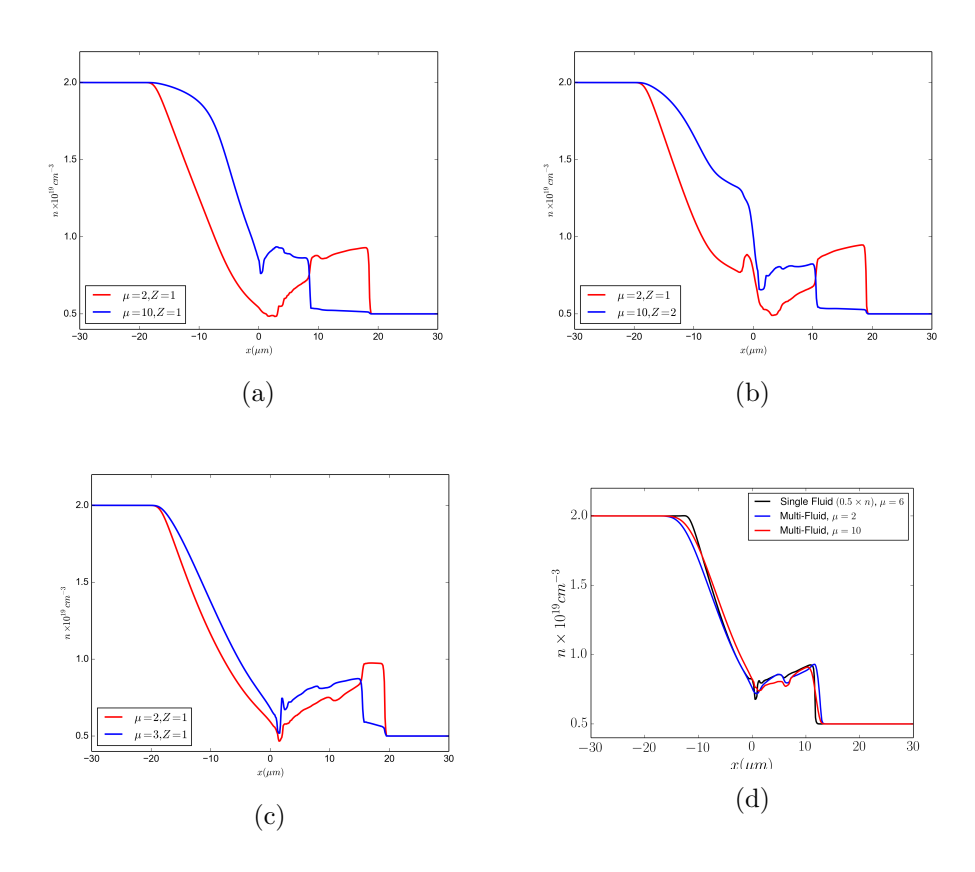


Figure 5.1: Density plots at t=150ps, for two ion species for $\delta_i=1.2,\ c/v_o=3,065$ and $\mathrm{Kn}_i=0.8$. Z is the ionization level and μ is the ratio of the ion mass to a proton mass. Plot (b) shows the decrease in separation with an increase in the ionization level. Plot (c) is the case more relevant for ICF, and it shows that there is less separation compared to (a) and (b). In plot (d) $\mathrm{Kn}_i=0.008$ showing that for high collisionality the solution converges to a single fluid averaged atom for a $\mu=6$.

there is no a guarantee of high collisionality throughout the entire implosion process. In fact, in Ref. [65] the authors argue that during the capsule implosion that the fuel behaves as a quasi-collisionless, classical plasma. This might mean that the separation is more of a kinetic effect and that models that depart further from Maxwellian equilibrium are needed to more accurately represent this phenomenon.

5.3 Spherical Geometry Results

For the ICF fuel species separation problem, spherical symmetry is assumed, which reduces the equation system to a one-dimensional problem in the radial direction. The balance law form (Eqn. 2.39) in spherical coordinates is given as,

$$\frac{\partial \mathbf{Q}_s}{\partial t} + \frac{1}{r^2} \frac{\partial (r^2 \mathbf{F}_s)}{\partial r} = \mathbf{S}_s. \tag{5.2}$$

By expanding the second term on the left-hand-side and reorganizing the equation, spherical symmetry equation takes a similar form as the Cartesian one with an additional source term

$$\frac{\partial \mathbf{Q}_s}{\partial t} + \frac{\partial \mathbf{F}_s}{\partial r} = \mathbf{S}_s - 2\frac{\mathbf{F}_s}{r}.$$
 (5.3)

The equations are normalized as described in Sec. 2.4.

One-dimensional spherically imploding capsules are simulated in plasma regimes of interest for ICF. The problem initialization is on profiles of experimental measurements[70] and adapted to resemble a shock tube,

$$\begin{cases} r < 600 \ \mu\text{m} : & n_D = n_T = 1. \times 10^{21} \text{ cm}^{-3}; & T_D = T_T = T_e = 75 \text{ eV} \\ r > 600 \ \mu\text{m} : & n_D = n_T = 1. \times 10^{22} \text{ cm}^{-3}; & T_D = T_T = 750 \text{ eV}, & T_e = 250 \text{ eV} \end{cases}$$
(5.4)

the problem is normalized using the deuterium initial conditions, and the dimensionless parameters are the speed-of-light to ion thermal speed ratio $c/v_o = 1120$, the ion skin depth is $\delta = 5.37 \times 10^{-3}$, the DT Knudsen number is $\text{Kn}_{DT} = 1.07 \times 10^{-2}$, the electron-ion Knudsen number is $\text{Kn}_{eD} = \text{Kn}_{eT} = 8.3 \times 10^{-3}$, and the flux limiter for the heat flux is f = 0.06, which is the value regularly used in ICF[70]. Zero flux boundary conditions are

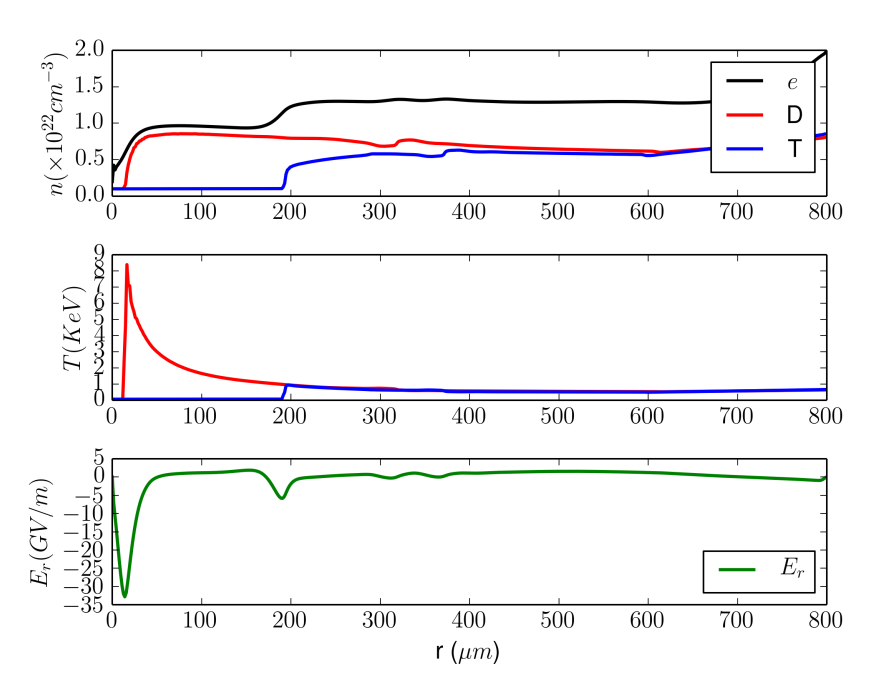


Figure 5.2: Plot for a spherical imploding DT plasma for $c/v_o = 1120$, $\delta = 5.37 \times 10^{-3}$, $\mathrm{Kn}_i = 1.07 \times 10^{-2}$, $\mathrm{Kn}_e = 8.3 \times 10^{-3}$, and f = 0.06. Shown are the number density, temperature and radial electric field at t = 1.375 ns. As the compression evolves and the fluids approach the center the density and temperature increase. The charge separation between the ions and the electron generate radial electric fields which peak at regions of large density and temperature gradients.

used at $r = 0 \mu m$ and zero normal gradient boundary conditions are used at $r = 800 \mu m$.

Figure 5.2 shows profiles of the number density, temperature and electric field at t = 1.375 ns. There is clearly a separation of the deuterium and the tritium, and electric fields in the order of GV/m form and peak in regions where the density and temperature gradients are large. Fig. 5.3 shows the relative difference in number density between the deuterium and the tritium. The separation occurs from the beginning of the simulation and increases over time, and by the time the deuterium shock front reaches the center of the of the capsule, it is $\sim 170~\mu m$ ahead of the tritium shock front. The time delay between when the deuterium shock reaches r = 0 to when the tritium one does is ~ 0.35 ns. The peak deuterium concentration occurs slightly off center (region in gray in Fig. 5.3) as the reflected

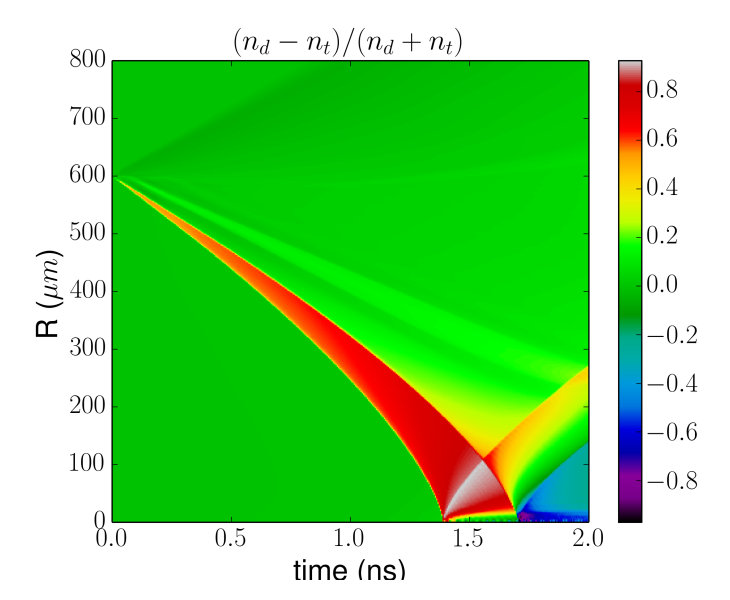


Figure 5.3: Relative difference between the deuterium and the tritium number densities as a function of radius and time. Regions where the deuterium percentage is larger are in red, and blue where the tritium is larger. The deuterium separates from the tritium from the beginning and the separation increases as time progresses. A 0.35 ns interval separates the deuterium and the tritium shocks reaching the center.

portion interacts with a fraction that is moving towards the center. After both species have reached the center (t ~ 1.7 ns) there is a depletion of the deuterium from the center, shown in the figure in blue.

Fields on the order of Gigavolts per meter (GV/m) develop. In Refs. [65, 67], the authors suggested that at the beginning of the simulation, the electric field produces an equivalent force on both ion species. The deuterium, which has a smaller mass, experiences a bigger acceleration, and moves to shield the tritium from the electric field thereby reducing its accelerations. To verify if the electric fields are actually the cause of the separation, the maximum value of the different forces present in the system are a plotted as a function of time in Fig. 5.4(a). There are three forces acting on each ion, the pressure gradient (dp/dr) that separates them, the frictional force (R_{dt}) that opposes the separation, and the electric force that, in this case, also contributes to the separation of the two ion species. The frictional force is six orders of magnitude smaller than the pressure gradient which dominates through the entire implosion. The force produced by the electric field is about an order of magnitude larger than the frictional force, which acts to increase the ion separation. Therefore, even though the electric fields are in the order of GV/m, the force they produce are small in comparison to the pressure gradient. Therefore the electric fields are not the main cause of the species separation. If the frictional force is small, then the DT Knudsen number is large, which brings into question whether a fluid model is appropriate to represent the physics in this problem. Figure 5.4(b)shows the value of the deuterium-tritium Knudsen number as a function of space and time. Recall that $\mathrm{Kn} \ll 10^{-2}$ is where fluid description of the plasma is valid. The plot shows that a fluid description is valid for almost the entire duration of the implosion, until $t \sim 1$ ns, where the Knudsen number starts increasing due to the rapid increase in the deuterium temperature, $Kn_{dt} \sim T_d^2/n_t$. In regions of large deuterium temperature and low tritium number density Kn_{dt} is large, and the plasma becomes kinetic and fluid description breaks down. Figures, 5.4(c) and (d) show the Kn_{dd} and Kn_{tt} as a function of space and time, respectively, and as deuterium and tritium fluids approach the center, kinetic physics start to dominate.

The three-fluid (deuterium-tritium-electron) simulation, used above, is compared to a two-fluid fluid one, composed of a DT-ion fluid with an averaged DT-mass and an electron

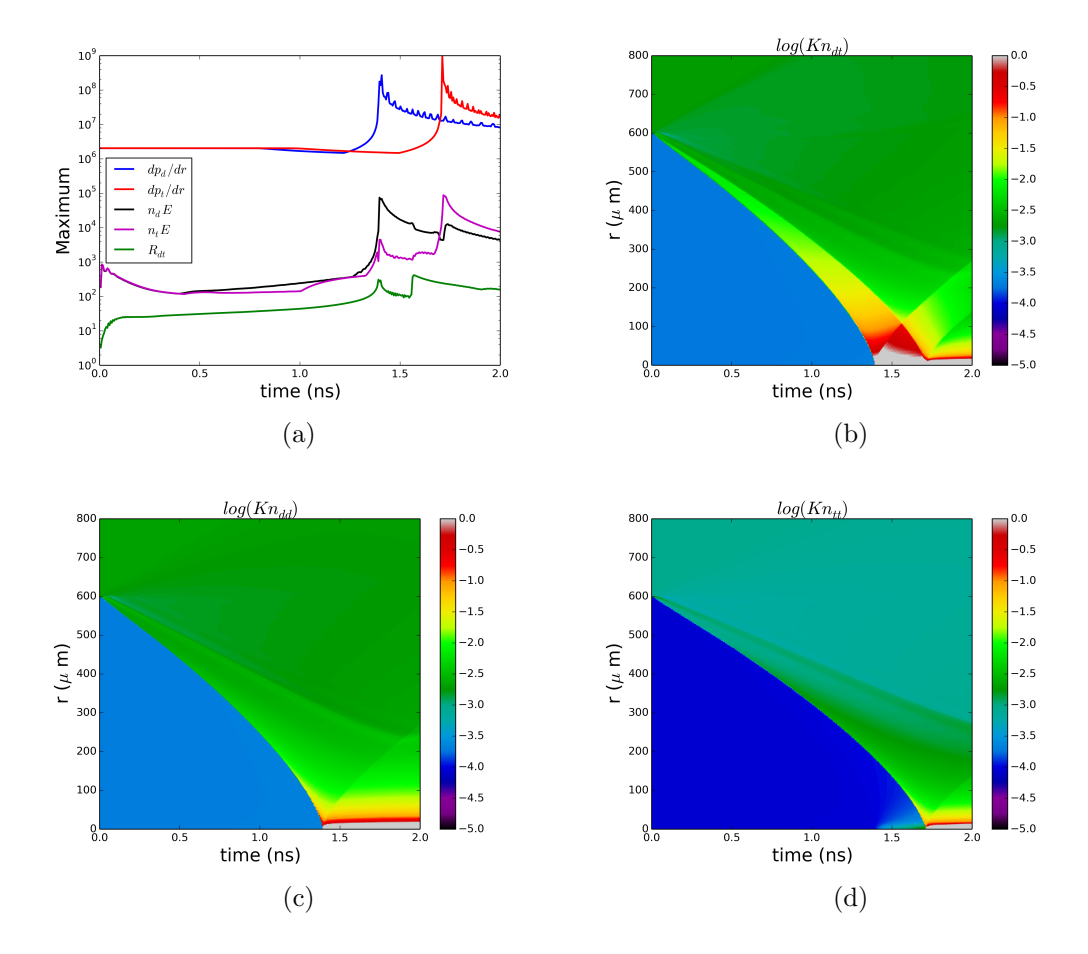


Figure 5.4: (a) Plots the normalized maximum values of the deuterium pressure gradient, electric, and frictional forces for the time interval before the deuterium reaches the center of the capsule. The pressure gradient and the electric force cause the separation and are orders of magnitude larger than the frictional force which resists the separation. (b) For the same time interval the largest value of the mean free path and the corresponding Knudsen number are plotted. This shows that for the majority of the time $\mathrm{Kn} < 10^{-2}$, so a fluid description of the plasma is valid. (c) and (d) show the Kn_{dd} and Kn_{tt} respectively, and as these fluid approach the center of the imploding capsule, the deuterium-deuterium and tritium-tritium collisions decrease.

Table 5.1: Parameter used in Eq. (5.6) for the calculation of the DT reactivity as a function of the ions temperature [3].

Reaction Fit	Units	$T+D \rightarrow n+^4 He$
C_0	${ m keV^{1/3}}$	6.6610
$C_1 \times 10^{16}$	${ m cm^3/s}$	643.41
$C_2 \times 10^3$	${ m keV^{-1}}$	15.136
$C_3 \times 10^3$	${ m keV^{-1}}$	75.189
$C_4 \times 10^3$	${ m keV^{-2}}$	4.6064
$C_5 \times 10^3$	${ m keV^{-2}}$	13.500
$C_6 \times 10^3$	${ m keV^{-3}}$	-0.10675
$C_7 \times 10^3$	${ m keV^{-3}}$	0.01366
T range	keV	0.2-100
Error		< 0.25%

fluid. Current ICF HYDRA simulations[10] are done using averaged mass models. It is suspected that species separation affects the DT fusion reaction rate considerably, and may be the cause of the unexpectedly low neutron yield. A measurement of how much the DT-fusion reaction has occurred is done by measuring the neutron yield given as

$$Y = \int \int n_D n_T \langle \sigma \nu \rangle_{DT} dV dt \tag{5.5}$$

where the DT reactivity, $\langle \sigma \nu \rangle_{DT}$, can be fitted using the expression[3]

$$\langle \sigma \nu \rangle_{DT} = C_1 \zeta^{-5/6} \xi^2 \exp\left(-3\zeta^{1/3} \xi\right)$$
 (5.6)

where

$$\zeta = 1 - \frac{C_2 T + C_4 T^2 + C_6 T^3}{1 + C_3 T + C_5 T^2 + C_7 T^3},\tag{5.7}$$

and

$$\xi = C_0 / T^{1/3}. (5.8)$$

The values of the constants $C_0 - C_7$ are given in Table (5.1). In the three-fluid simulation the averaged temperature is calculated as $T = (p_D + p_T)/(n_D + n_T)$.

Comparing the three-fluid and two-fluid yields over a 2 ns interval we obtain that $Y_{3f}/Y_{2f} = 0.3362$. In the three-fluid case, there is separation of the deuterium from the tritium, and as a consequence, the yield is only about one third that of the two-fluid problem. Figure 5.5 compares the product of the number density for both cases and the ratio of the reactivities are plotted. The figure shows three shocks reaching the center and being reflected. The first shock corresponds to the 3-fluid case when the deuterium reaches the center. The second shock corresponds to the 2-fluid case when the averaged mass ion reaches the center. The third one is when the tritium from the 3-fluid case reaches the center. If a horizontal line, at a fixed radius, is drawn, and $n_D n_T$ is measured, the value for the two-fluid simulation is higher, therefore the yield calculation for the two-fluid should be bigger than the three-fluid simulation.

Figure 5.6 shows the temperature and reactivity at the center of the capsule plotted as a function of time. The deuterium reaches the center earlier than ion fluid in the two-fluid simulation. At this time in the simulation, the temperature of the two-fluid simulations at r=0 is still low and the ion reaches the capsule center ~ 0.175 ns after the deuterium. After another ~ 0.175 ns, the tritium fluid from the three-fluid simulation reaches the capsule center and the mass averaged temperature of the three-fluid simulation dips below the two-fluid ion temperature. For the remainder of the simulations the three-fluid ion temperature remains below the two-fluid temperature. Figure 5.6 also shows why initially the ratio of the two reactivities is 15 orders of magnitude, that is because the deuterium reaches the center first. Note that the two-fluid plasma reaches the center exactly in between the time the deuterium and the tritium for the three-fluid plasma, as expected for a mass averaged fluid.

The electric fields have their peak value at the shock fronts. In Fig. 5.7 the maximum electric field is plotted over time. The peak field for the two-fluid plasma is on the order a 160 GV/m while the three-fluid has double peaks corresponding to when the deuterium and tritium reach the center, and is about ~ 80 GV/m. These values of the electric field are of the same order of magnitude as those inferred and simulated in Ref. [65].

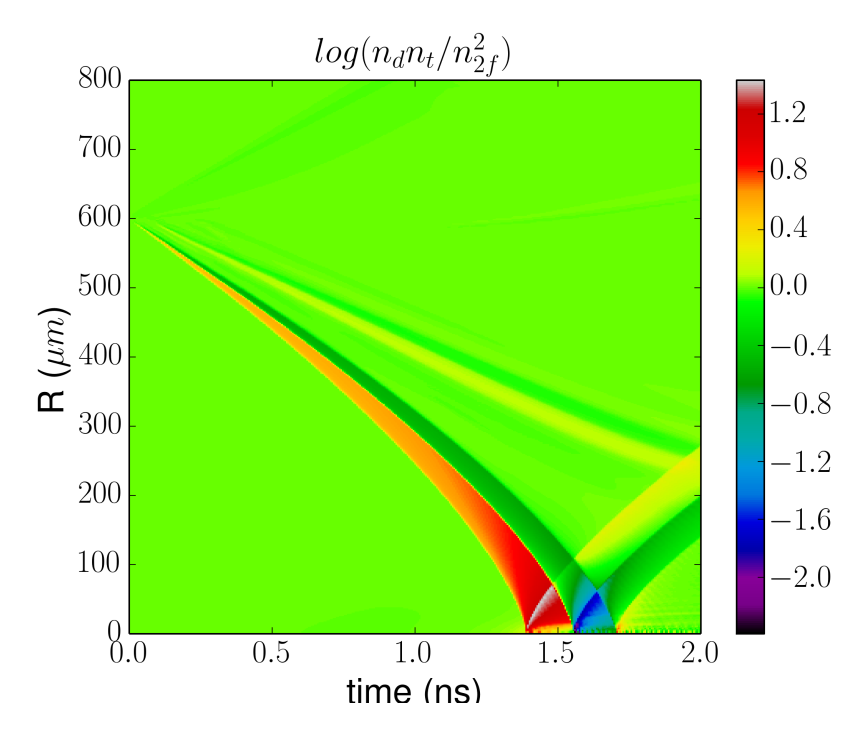


Figure 5.5: Comparison of the variables used when calculating the neutron yield for the three-fluid and two-fluid cases. Comparison of the ratio of the density product $n_d n_t$ in the three-fluid simulation with the square of the density of the two-fluid simulation. The density product for the two-fluid case is larger than the three-fluid case where the ions have separated, therefore the first term in the yield calculation is larger for the two-fluid simulation.

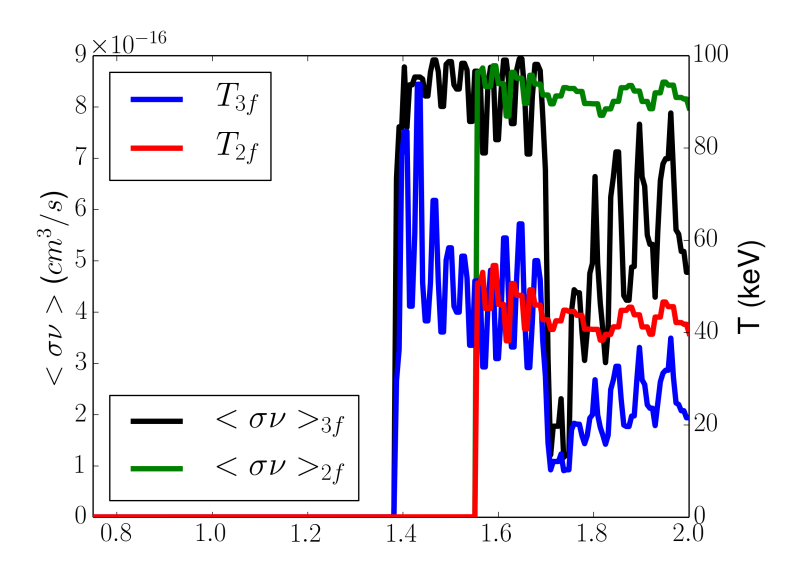


Figure 5.6: Temperature and DT reactivity at r=0 for the three-fluid and two-fluid simulations are plotted over time. In the three-fluid simulation ions reach the center earlier causing an increase in the temperature and the reactivity a few nanoseconds before the two-fluid ions reach the center. Although the temperature is initially larger for the three-fluid case, after the two-fluid case reaches the center its temperature remains steadily higher.

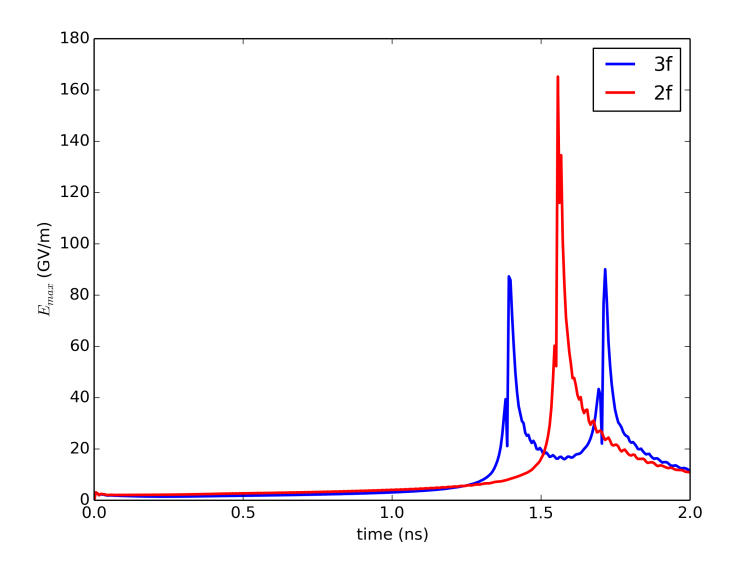


Figure 5.7: Maximum electric field plotted over time. The two-fluid case produces a larger peak electric field than the three-fluid simulation by a factor of two. However, gigavolt per meter electric fields produce forces that are still too small compared to the plasma pressures in the problem.

5.4 Summary

The Inertial Confinement Fusion (ICF) fuel species separation problem has been extensively analyzed using the multi-fluid plasma model and the blended finite element method. Most ICF capsule implosion simulations assume that there is high collisionality between the deuterium and tritium, therefore, they use radiation-hydrodynamic simulations to study separation. It is shown that the single fluid, average mass atom assumption is not accurate because the collisionality between the deuterium and the tritium is low, and in a Knudsen number regime where there is a transition from a fluid to a kinetic plasma. Low collisionality between the ion species is not capable of producing fictional forces that are large enough to overcome the pressure gradients experienced by the plasma. Electric field on the order of Gigavolts per meter are generated, however the forces they produce is small in comparison to the pressure gradients, which are the main cause of separation. The separation of the ICF fuel causes the fusion reaction rate to decrease to about one third of the yield pro-

duced by radiation-hydrodynamic conditions, which are in line with the 50% reduction that experimental results have shown.

Chapter 6

UNCERTAINTY QUANTIFICATION OF THE GEM CHALLENGE MAGNETIC RECONNECTION PROBLEM USING THE MULTILEVEL MONTE CARLO METHOD

6.1 Prior and Foundational Work

Uncertainty quantification (UQ) of plasma simulations are extremely important because, in most cases, they are compared to experimental results in an attempt to validate the simulations and explain the relevant physics of an experiment. Just like experimental data have a region of certainty in the measured data (error bars), uncertainty quantification can be used to produce the same effect on computationally generated results.

There are numerous sources of uncertainty in many plasma models, including the Two-Fluid Plasma Model (TFPM). This uncertainties range from individual parameters uncertainty, to boundary or initial conditions, transport coefficients among others. Often times the exact value of a parameter is not know, only a range of values. Treating all the input values as stochastic ic computationally expensive. Therefore, different sensitivity analysis methods have been developed to rank the importance of the random inputs and their interactions.

The Multilevel Monte Carlo (MMC) method was developed by Giles [26] for use in computational finance for the solution of stochastic differential equations. Giles proved that computational complexity could be reduced through the use of a multilevel approach that combines results obtained using different levels of discretization while reducing the variance. The MMC method uses a geometric sequence of time-steps similar to the multi-grid method and has proven to be efficient and reliable in achieving the desired accuracy.

This permits establishment of regions of confidence in simulations which can subsequently be compared to experimental results. The MM method shows promising results when it come to accuracy and computational cost.

The MMC method was extended from stochastic ODEs to elliptic PDEs in problems with

random coefficients arising in ground water flow[28]. In the case of the PDEs the geometric series is applied to the spatial discretization instead of the temporal although both may be related through the CFL stability condition. There is a dramatic reduction in cost associated with the MMC method over the standard Monte Carlo (MC) method. Most of the uncertainty can be captured on a coarse spatial discretization, thereby reducing the need for numerous simulations on the finer and more computationally expensive discretizations.

Another method used in this study is the Probabilistic Collocation (PC) method. The PC method was first introduced by Tatang and McRae [72], and recently Xiu and Hesthaven [73] have used Lagrange polynomial interpolation to construct high-order stochastic collocation methods. The properties of PC method were extensively studied in the past ten years. The errors of integrating or interpolating functions with Sobolev regularity were analyzed for Smolyak constructions based on one-dimensional nested Clenshaw-Curtis rules [74, 75, 76]. The degree of exactness of the Smolyak quadrature using Clenshaw-Curtis and Gaussian one-dimensional rules was investigated in Ref. [75]. The efficiency of Clenshaw-Curtis-based sparse grid stochastic collocation was demonstrated in comparison to other stochastic methods on an elliptic problem [73]. In 2003, Gerstner and Griebel [77] introduced the dimension-adaptive tensor product quadrature method. Sparse grid collocation schemes were applied to solving stochastic natural convection problems [78]. An adaptive hierarchical sparse grid collocation algorithm has been developed [79, 80].

Reference [81] describes a Multi-Element Probabilistic Collocation Method (ME-PCM) that was developed to study the sensitivity of the TFPM model. The ME-PCM based sensitivity analysis method is efficient and can achieve fast convergence compared to standard MC based sensitivity analysis methods for cases with 20 – 100 random parameters.

In the research reported here, the MMC, MC, and PC methods will be applied to the GEM challenge magnetic reconnection^[2] problem for sensitivity and uncertainty quantification study. Magnetic reconnection is a physical process that occurs in plasma by which the magnetic field lines tear and reconnect and in the process convert magnetic energy into kinetic energy. This phenomenon is present in virtually every plasma, whether in laboratory fusion research experiments, stars solar flares, or even in the Earth's magnetosphere.

Reference [2] presents multiple plasma models that are used in an effort to understand

the process on magnetic reconnection in better detail. Ideal MHD the magnetic field lines are frozen into and move with the plasma; however for magnetic reconnection to occur, the frozen-in flow constraint must be broken and this can only be done if there is some resistivity or two-fluid effects.

In a fluid description the frozen-in constraint is broken and the magnetic topology is allowed to change when the scale sizes in the system approach the electron skin depth $\delta_e = c/\omega_{pe}$, where c is the speed of light and ω_{pe} is the electron plasma frequency. Therefore, changing the electron mass or the speed of light affects this scale size[82].

The plasma model used here is the two-fluid model which models the electrons and ions as separate fluids and couples both fluids through the Maxwell's equations[37]. The numerical scheme used is the wave propagation method[38]. It is a class of Godunov methods, which rely on the solution of a Riemann problem at each cell interface while allowing for discontinuities at these interfaces. Second order accuracy is achieved by applying flux limiters.

The main objective of this work is to evaluate the benefits of the MMC method and quantify the uncertainty in the GEM challenge problem due to the choice of ion-to-electron mass ratio, speed of light to Alfvén speed ratio, and the magnetic flux perturbation that determines the dominant mode in reconnection, on the reconnected flux evolution.

6.2 Plasma Models for Uncertainty Quantification Study

In this work, two different plasma models are employed to quantify the uncertainty and compare three UQ methods (MC, MMC and PC). The first plasma model is the quasi-neutral ion cyclotron waves model. The problem models a quasi-neutral ion cyclotron wave, a dispersive wave, in an uniform plasma in a magnetic field that is constant in space and time. Like the two-fluid plasma model, the quasi-neutral ion cyclotron waves has imaginary

eigenvalues of the source Jacobian. The equation system being solved is given as

$$\frac{\partial \rho}{\partial t} + \rho \frac{d\mathbf{u}}{dx} = 0, \tag{6.1}$$

$$\rho \left(\frac{\partial \mathbf{u}}{\partial t} + \mathbf{u} \frac{\partial \mathbf{u}}{\partial x} \right) + \frac{\partial p}{\partial x} = nq\mathbf{u} \times \mathbf{B} = \rho \omega_c \mathbf{u} \times \hat{b}, \tag{6.2}$$

$$\frac{\partial \epsilon}{\partial t} + \frac{d}{dx} \left((\epsilon + p)\mathbf{u} \right) = 0, \tag{6.3}$$

where ρ is the mass density, **u** is the velocity, p is the pressure, **B** is the magnetic field, \hat{b} is the unit vector in the direction of **B**, $\omega_c = \frac{q|\mathbf{B}|}{m}$ is the ion cyclotron frequency, and

$$\epsilon = \frac{p}{\gamma - 1} + \frac{1}{2}\rho u^2 \tag{6.4}$$

is the total energy density, where γ is the ratio of specific heats.

A benefit of using this problem is that the exact solution of the velocity field is known and given by

$$u(x,t) = -\sum_{n=0}^{N} \frac{u_1^o}{2n+1} \sin(k_n x + \omega_n t), \tag{6.5}$$

when the fluid is initially perturbed with the random velocity (to simulate uncertainty),

$$u_1(x) = u_1^o(\xi) \sum_{n=0}^{N} \frac{i}{2n+1} e^{ik_n x}, \tag{6.6}$$

where $u_1^o(\xi)$ is the random velocity, ξ is a random variable with uniform distribution, $U[10^{-10}$ to $10^{-4}]$, $k_n = 2\pi(2n+1)$ is the wave number, $\omega_n = \pm \sqrt{k_n^2 c_s^2 + \omega_c^2}$ is the dispersion relation, and $c_s = \sqrt{\gamma p/\rho}$ is the speed of sound. This problem is computationally inexpensive.

The second plasma model is the collisionless TFPM[83, 16, 84] which is derived by taking moments of the Boltzmann equation and regarding the electron and ion species as separate fluids. The resulting equation system for the TFPM is used to evolve the fluid variables and Maxwell's equations advance the electric and magnetic fields. The fluids and fields variables couple through the source terms.

There are several sources of uncertainty in the two-fluid plasma model. Often times modelers change the ion-to-electron mass ratio or the speed of light to Alfvén speed ratio to

speed up the computation. This study aims to quantify the uncertainty of varying the ion-toelectron mass ratio, speed of light to Alfvén speed ratio, and the magnetic flux perturbation that determines the dominant mode of the reconnection, have on the reconnected flux of the the GEM magnetic reconnection challenge. In particular, we assume $m_i/m_e = \xi_1$, where ξ_1 is a random variable with uniform distribution U[25, 100], $v_A/c = \xi_2$, ξ_2 is a random variable with uniform distribution, U[10, 20], $v_A = B/\sqrt{\mu_o \rho}$ and the magnetic flux perturbation, $\psi = \xi_3 \psi_p$. Here ξ_3 is a random variable with uniform distribution, U[0.085, 0.115].

The other model used is the ideal multi-fluid plasma model described in Sec. 2.5. The source terms in Maxwell's equations couple the fluid variables to the electromagnetic fields and the Lorentz forces act as body forces on the electrons and ions. These source terms introduce physical dispersion in the two-fluid model which comes from the fact the flux Jacobian of the system has imaginary eigenvalues and therefore the waves in the system are undamped [84].

Contrary to the MHD model, the two-fluid plasma model includes the Hall and diamagnetic-drift terms, assumes a finite speed of light, and a finite electron mass. These assumptions allow for the description of displacement current effects and high-frequency oscillations.

Both models are solved using the high-resolution wave propagation (a finite volume) method. The solution method belongs to the class of Godunov solvers, which rely on the solution of Riemann problems described in Refs. [83, 19, 38] and can be applied to balance laws of the form Eq. (2.39). A Riemann problem is solved at each cell interface and the solution is, in general, discontinuous. Second order accuracy can be achieved by performing a linear reconstruction of the waves needed to compute the numerical fluxes at the cell interfaces[19].

6.3 Standard Monte Carlo Method

In statistics, aggregate mathematical measures are created to characterize data, these rules are referred to as estimators. Common estimators are the mean value and the variance of

the data set. In the standard MC method the mean estimator is given as

$$\mathbb{E}[P_{m,N}^{MC}] = \frac{1}{N} \sum_{i=1}^{N} P_m^i, \tag{6.7}$$

where N is the number of samples and P_m^i is a measured quantity of each sample i obtained using m spatial grid points. The value of P_m^i obtained using m grid points approaches the exact solution, P, as the number of grid points increases and the mean square error (MSE), e^2 , can be represented as

$$e_{MC}^2 = \mathbb{V}[P_{m,N}^{MC}] + (\mathbb{E}[P_m] - \mathbb{E}[P])^2.$$
 (6.8)

The first term represents the sampling error and is given by

$$\mathbb{V}[P_{m,N}^{MC}] = \frac{1}{N-1} \sum_{i=1}^{N} (P_m^i - \mathbb{E}[P_{m,N}^{MC}])^2, \tag{6.9}$$

which is the variance. The second term of Eq. (6.8) represents the discretization error. To achieve an MSE less than ϵ^2 , both terms are chosen to be less $\epsilon^2/2$. Reducing the first term is achieved by having a large number of samples, $N \sim O(\epsilon^{-2})$. The second term is reduced by increasing the number of grid points (increased resolution), $m \sim O(\epsilon^{-1/\alpha})$ where α is the discretization convergence rate[28].

6.4 Multilevel Monte Carlo Method

For most numerical simulations, either large sample size or high discretization are computational expensive. Therefore, novel methods that reduce the numerical error while achieving "reasonable" discretization and sample size are desired. In this case the MMC method is chosen to quantify the uncertainty in the two-fluid plasma model.

When there is uncertainty in a quantity or constant being used in a numerical simulation it is common to use a MC method to study the effects of this uncertainty in the solution of the problem. This is done by running a large number of simulations each using a randomly selected value of set quantity within the uncertainty interval. All the simulations are exe-

cuted using the same discretization. For the MMC method for each random quantity two simulations are done at different discretization.

The MMC estimator is defined as

$$P_m^{MMC} = \sum_{l=0}^{L} Y_l, (6.10)$$

where

$$Y_l = \frac{1}{N_l} \sum_{i=1}^{N_l} (P_{m_l}^i - P_{m_{l-1}}^i), \tag{6.11}$$

The MMC mean estimator is

$$\mathbb{E}[P_m^{MMC}] = \sum_{l=0}^{L} \mathbb{E}[Y_l], \tag{6.12}$$

where $P_{m-1}^i = 0$. In this case, because there are different discretization levels, l, the spacial resolution becomes, m_l , to denote the number of grid points at level l. Also, the sample size (N) from Eq. (6.7) is now level dependent (N_l) and does not need to be the same for every level. Y_l is estimated independently for each level l and the multilevel variance estimator is

$$\mathbb{V}[P_m^{MMC}] = \sum_{l=0}^{L} \mathbb{V}[Y_l]. \tag{6.13}$$

Following Eq. (6.8) the error in the MMC method is expressed as

$$e_{MMC}^2 = \sum_{l=0}^{L} \mathbb{V}[Y_l] + (\mathbb{E}[P_{m_l} - P])^2,$$
 (6.14)

where

$$V[Y_l] = \frac{1}{N_l} V(P_{m_l} - P_{m_{l-1}}). \tag{6.15}$$

The multilevel variance $\mathbb{V}[Y_l] = N_l^{-1}V(P_{m_l} - P_{m_{l-1}}) \to 0$ as $l \to \infty$ and if the variance is decreasing, a lesser number of sample data will be needed, consequently $N_l \to 1$ as $l \to \infty$. The cost at the coarsest level is fixed for all levels of accuracy. Achieving an overall MSE of ϵ with MMC method is easier than the standard MC method. The MMC method is used

to measure the effect uncertainty in the initial velocity for the quasi-neutral ion cyclotron waves problem. This problem is chosen because it is computationally inexpensive. The MC and MMC methods are compared for numerical cost and variance in the solution. Then, the uncertainty due to the ion to electron mass ratio, light speed to Alfvén speed ratio, and initial magnetic flux perturbation in the collisionless magnetic reconnection problem are each studied separately. The reconnected flux for each case is computed for comparison.

Once the variable with uncertainty is identified, a range and distribution for the uncertainty are chosen. A uniform distribution is used in all cases in this study; however, other distributions could also be used (e.g. Maxwellian). For each simulation the specified variable is set to a random value within the given range. Since the distribution is uniform, every value has an equal probability of being selected.

The procedure for the multilevel method used in this implementation is described below.

- Start at level zero, l = 0, the coarsest grid.
- Step 1: Collect initial sample (velocity at x = 0 in the quasi-neutral ion cyclotron waves problem and magnetic field in the reconnection problem) at the current level and obtain initial statistics of the problem, mean and variance.
 - Calculate initial samples, each using a random coefficient (e.g. mass ratio, initial velocity...) from an uniform distribution. The resolution (spacial discretization) is given by $m_l = M^l m_o$, where M^l is the refinement multiplier (in this case M = 2, double grid points from level l 1 to l), and m_o is the coarsest level resolution.
 - If the current level is zero, the simulations are standard Monte Carlo (the mean is calculated from Eq. (6.7)), and data is collect only at one discretization level.
 - If the current level is not zero, for each random coefficient, two cases are run, one at resolution $M^l m_o$ and another at the immediately lower resolution $(M^{l-1} m_o)$. Then compute the difference between a chosen observed variable/quantity (e.g., velocity or reconnected flux) of the two cases $P_{m_l} P_{m_{l-1}}$. Because the solutions

are at different resolutions, the intermediate values at the coarse grid are the average of the values of the two closest grid-points.

- The multilevel estimator of the mean of the solution is given by Eq. (6.12) and is calculated from data collected at two different discretization levels.
- Step 2: Estimate the variance using the initial sample. The unbiased variance of each level is given by Eq. (6.15). Not to be confused with the overall method variance given in Eq. (6.13).
- Step 3: Calculate the optimal sample size for all levels up to the current one. The optimal number, N_l required to reduce the variance V_l to less than $\frac{1}{2}\epsilon^2$ is given from Ref. [26] as

$$N_l = 2\epsilon^{-2} \sqrt{V_l m_l} \left(\sum_{k=0}^l \sqrt{V_k / m_k} \right). \tag{6.16}$$

- Step 4: Collect additional sample at each level as needed for the new N_l . Run additional cases if N_l is bigger than the initial number of the sample.
- Step 5: Check for convergence. If $l \geq 1$, and $\max \left(M^{-1} |\hat{P}_{L-1}^{MMC}|, |\hat{P}_{L}^{MMC}| \right) < \frac{1}{\sqrt{2}} (M-1)\epsilon$ then the error is less than $\frac{1}{\sqrt{2}}\epsilon$ and the solution has converged.
- Step 6: If the solution has not converged, increment level to l+1 and repeat from step 1.

Another uncertainty quantification method, probabilistic collocation, is described in the Appendix.

6.5 Numerical Results

The quasilinear ion cyclotron wave problem is used to examine the performance of the MMC method in computing the expected values of the velocity. This model is nonlinear and less computationally expensive than the full two-fluid model. It is a one-dimensional (1D) problem, with periodic boundary conditions and the velocity field is initialized to the

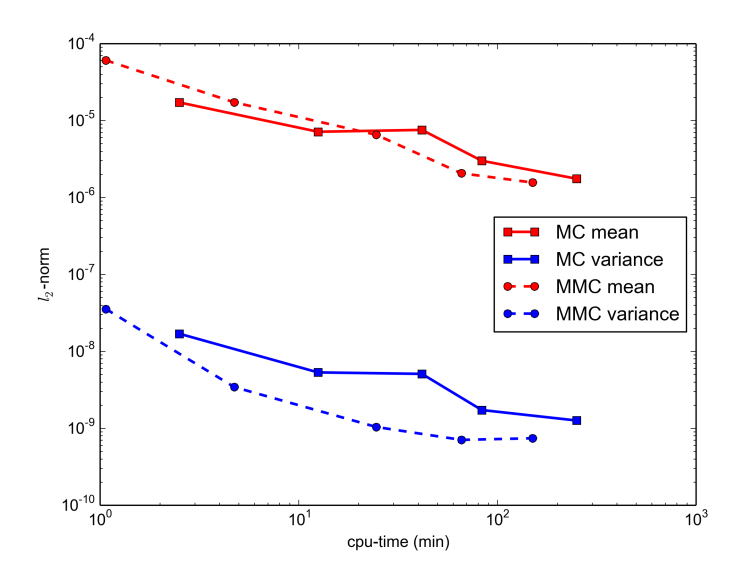


Figure 6.1: $L_2 - norm$ error for the mean and variance as a function of computational time using the quasi-neutral ion cyclotron wave test problem. With $c_s = \sqrt{1.4}$, $\omega_c = 10.0$, $B_z = 1.0$, $m_i = 1.0$ and q = 10.0 and initial values of $\rho = 1.0$ and p = 1.0. The rates of convergence for the mean using the MC and MMC methods are similar. The rate of convergence for the variance using the MMC method is faster than the MC method.

approximate step function given by Eq. (6.6) with N = 9. The results are analyzed after one unit of normalized time. The uncertainty is on u_1^o , Eq. (6.6), using an uniform distribution from 10^{-10} to 10^{-4} .

Figure 6.1 shows the L_2 -norm error of the mean and the variance as a function of computational time. The L_2 -norm error is given as

$$||\Delta u||_2 = \sqrt{\frac{1}{m_l} \sum (\hat{u} - u_i)^2},$$
 (6.17)

where \hat{u} is a highly converged solution computed using 30,000 MC samples, treated as the accurate solution. The mean and variance are calculated using smaller sample sizes using MC or MMC method and compared to converged solution. The slope of the MC variance line is about -0.561, while the MMC variance slope is -0.777.

The Geospace Environmental Modeling (GEM) reconnection challenge [2] is an effort to understand the mechanism of collisionless reconnection using different plasma models. The reconnection process tears magnetic fields and converts magnetic energy into kinetic and thermal energies of electrons and ions. Magnetic reconnection is present in numerous plasma environments including solar flares and geomagnetic sub-storms. The GEM reconnection challenge involves using different plasma models, including Hall-MHD, full particle, and hybrid models.

The initial conditions used for all cases are given in Ref. [2]. A Harris equilibrium is used with a floor in the density outside the current layer. The magnetic field is initialized as

$$B_x(y) = B_0 \tanh(y/\lambda), \tag{6.18}$$

and the density as

$$n(y) = n_o \operatorname{sech}^2(y/\lambda) + n_\infty. \tag{6.19}$$

The pressure balance is given as $n_o(T_e + T_i) = B_o^2/8\pi$. The velocities are normalized to the Alfvén speed v_A . The normalized parameters for these simulations $B_o = 1$, $n_o = 1$, $\lambda = 0.5$,

 $n_{\infty}/n_o = 0.2$, $T_e/T_i = 0.2$. An initial perturbation in the magnetic flux is given as

$$\psi(x,y) = \psi_o \cos(2\pi x/L_x) \cos(\pi y/L_y), \tag{6.20}$$

and the magnetic field perturbation is given as $\mathbf{B} = \hat{z} \times \nabla \psi$ and $\psi_o = \xi_3$ which is the third source of uncertainty that is investigated in this research. When the uncertainties of m_i/m_e and c/v_A are being studied, ξ_3 is set to 0.1. The unit scale length is the ion-skin depth (c/ω_{pi}) and the unit time scale is the inverse ion cyclotron frequency (ω_{ci}^{-1}) . The computational domain is $L_x = 8\pi$ and $L_y = 4\pi$ and the final time is $400/\omega_{ci}$. The problem has periodic boundary conditions in the x-direction and conducting boundary conditions in the y-direction. To compare results, the reconnected flux, ϕ , is computed using,

$$\phi(t) = \frac{1}{2L_x} \int_{-L_x/2}^{L_x/2} |B_y(x, y = 0, t)| dx.$$
(6.21)

The two-fluid plasma method used in these simulations are in good agreement with the benchmarked results published in the GEM challenge paper [2] and can be seen in Ref. [19].

For magnetic reconnection to occur and magnetic fields to tear and reconnect, the magnetic field lines can not be frozen into the plasma and must move with the plasma. In a fluid description of plasmas the frozen-in constraint is broken and the magnetic topology is allowed to change when the length scales in the problem approach the electron skin depth $\delta_e = c/\omega_{pe}$, where c is the speed of light and ω_{pe} is the electron plasma frequency. In this study the effects of varying the speed of light and the electron mass are analyzed. Changing these quantities change the electron skin depth, which in turn could affect the reconnected flux.

In a hydrogen plasma the ion-to-electron mass ratio is 1836. However, running simulations at this mass ratio presents a challenge. The two-fluid plasma model has disparate timescales, i.e., ω_{cs}^{-1} and ω_{ps}^{-1} need to be resolved, where

$$\omega_{cs} = \frac{q_s |\mathbf{B}|}{m_s}, \qquad \omega_{ps} = \sqrt{\frac{n_s q_s^2}{\epsilon_o m_s}}$$
(6.22)

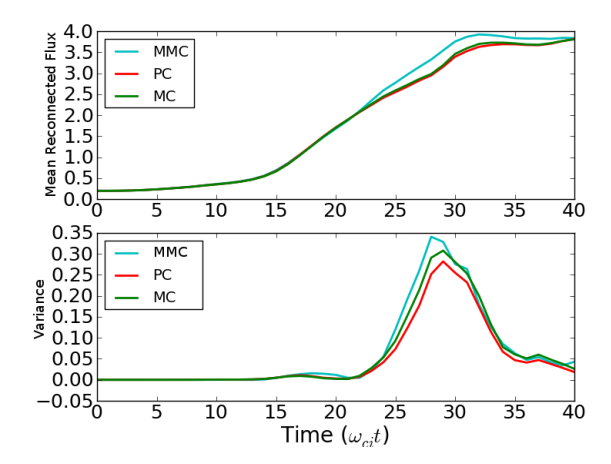


Figure 6.2: Mean (top) and variance (bottom) of the reconnected flux for varying ion-to-electron mass ratio ranging from 25 to 100, for the MMC, MC, and PC methods.

are the cyclotron frequency and the plasma frequency for each species, respectively. Decreasing the ion-to-electron mass ratio relaxes the time step restrictions and allows simulations to be completed in less time. A small artificial mass ratio of $m_i/m_e = 25$ is used in the GEM challenge paper to reduce the stiffness and speedup the computation.

Figure 6.2 shows the mean and variance reconnected flux for simulations by varying the mass ratio $m_i/m_e \in [25, 100]$ and the results of the MMC method is compared to the MC and PC methods results. The MMC simulations are completed using two levels with 32 simulations at a coarse grid (256×128) and 16 at a twice finer grid. The PC method has 33 simulations and the MC has 56, all at 512×256 resolution. The results for this case show that all three methods produce approximately the same mean and variance, σ^2 .

For the MMC method the variance is computed using

$$\sigma^2[P_l] = \mathbb{E}[P_l^2] - \mathbb{E}^2[P_l] \tag{6.23}$$

where

$$\mathbb{E}[P_l^2] = \mathbb{E}[P_o^2] + \sum_{l=1}^L \mathbb{E}[P_l^2 - P_{l-1}^2]$$
(6.24)

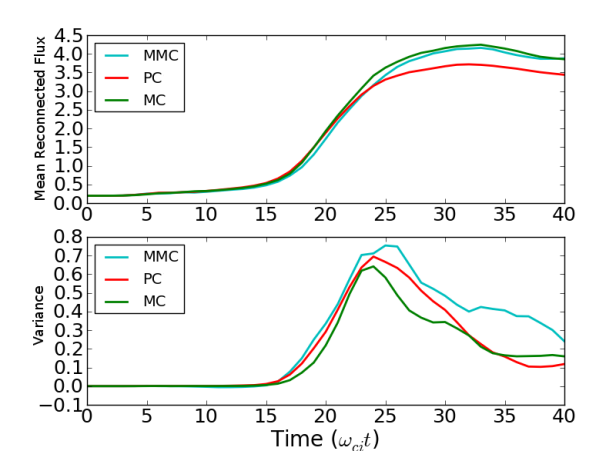


Figure 6.3: Mean (top) and variance (bottom) of the reconnected flux for varying speed of light to Alfvén speed ratio ranging from 10 to 20, for the MMC, standard MC, and PC method.

instead of the multilevel estimator given by Eq. (6.13).

The second variable of the skin depth that is analyzed is the speed of light, c. In the two-fluid plasma model, explicitly advancing the equations in time is limited by the highest frequency or the fastest velocity in the system. The speed of light is often the fastest speed in the system and hence usually generates the most restrictive time step constraint. Relaxing this restriction can be achieved by reducing the value of c. As mentioned before, all the velocities in the GEM challenge paper are normalized to the Alfvén speed and in all simulations $\epsilon_o = \mu_o = 1$.

Figure 6.3 shows the mean and variance when the ratio of the speed of light to the Alfvén speed is varied from $c/v_A \in [10, 20]$ for the three different methods, MMC (2 levels, 32 samples at level 0 and 16 at level 1), MC (56 samples), and PC method (33 samples), at the resolution of 512×256 (for the MMC this is the resolution of level 1, finest grid resolution).

The GEM reconnection challenge Harris equilibrium is perturbed by a sinusoidal flux with an amplitude ψ_o as described by Eq. (6.20). Depending on the amplitude of this perturbation the reconnection is either delayed or sped up, therefore, the reconnected flux

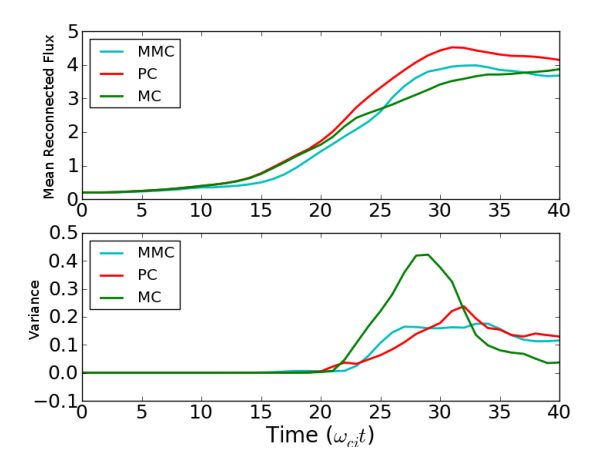


Figure 6.4: Mean (top) and variance (bottom) of the reconnected flux for varying amplitude of the magnetic flux perturbation ranging from [0.085, 0.115], for the MMC, standard MC, and PC method.

should be highly sensitive to variations in this parameter. Figure 6.4 shows the mean and variance of the reconnected flux when $\psi_o \in [0.085, 0.115]$ of the background magnetic field amplitude.

6.6 Discussion

The MMC, MC, and PC methods are applied to the GEM magnetic reconnection problem to study the sensitivity of the reconnected flux to uncertainties in ion-to-electron mass ratio, speed of light to Alfvén speed ratio, and the magnitude of the initial magnetic flux perturbation. The goal is to determine which of the methods is more computational inexpensive and reduces the variance more rapidly as the sample size is increased.

Initially the performance of the different methods is studied using the quasilinear ion cyclotron wave problem since it is computationally inexpensive. Figure 6.1 shows that the error decreases as the computational cost increases. However, the error in the MMC variance is lower than the MC method, and the variance decreases much faster for the MMC method. Therefore the MMC method gives a better result with less computation effort.

Figure 6.2 shows the results for the mass ratio study. Here the variance is relatively low

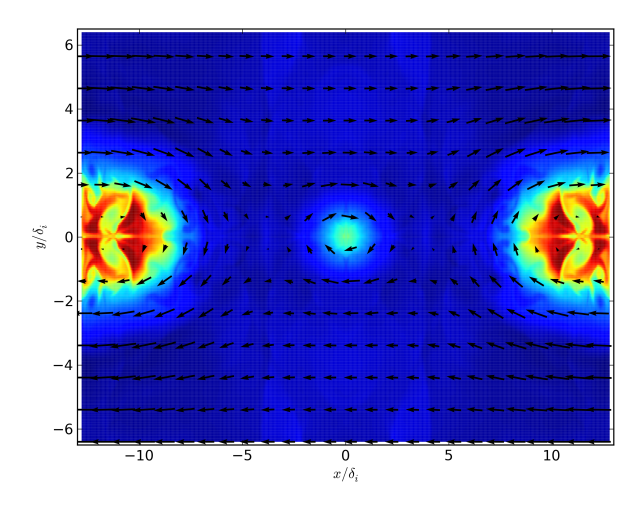


Figure 6.5: Ion density and magnetic field vectors showing the formation of a second smaller magnetic island at the center and as a result the reconnected flux in these cases is slightly higher because there are no asymmetries in the grid and during the solution the smaller island will remain at the center of the grid. However if some numerical asymmetry develops the island will move to the right or the left. $\omega_{ci}t = 38$ and $m_i/m_e = 25$.

except between $\omega_{ci}t = 25 - 35$, therefore the reconnected flux is relatively independent of the mass ratio. A possible explanation for the higher variance between $\omega_{ci}t = 25 - 35$ is that for certain cases an intermediate, smaller magnetic island forms at the center of the domain as seen in Fig. 6.5. This smaller island eventually merges with the bigger island.

Figure 6.3 demonstrates good agreement of the mean and the variance between the different methods showing the small sensitivity of the problem to changes in the speed of light to Alfvén speed ratio. Like the mass ratio case, the variance also spikes around $\omega_{ci}t = 23.0$ for the same reason as explained for the mass ratio.

The variance of the MC method is observed to be stochastically higher than the variance of the MMC and PC methods, as seen in Fig. 6.4. The MMC mean follows closely the MC mean. The cost of the MMC is much lower than the MC. The MMC method has 36 simulations at 256×128 resolution and only 6 simulations at 512×256 which resulted in a total of 4075 CPU-hours while the MC has 46 simulations at 512×256 resolution and a total of 6496 CPU-hours. Therefore, there is a total computational time saving of about one

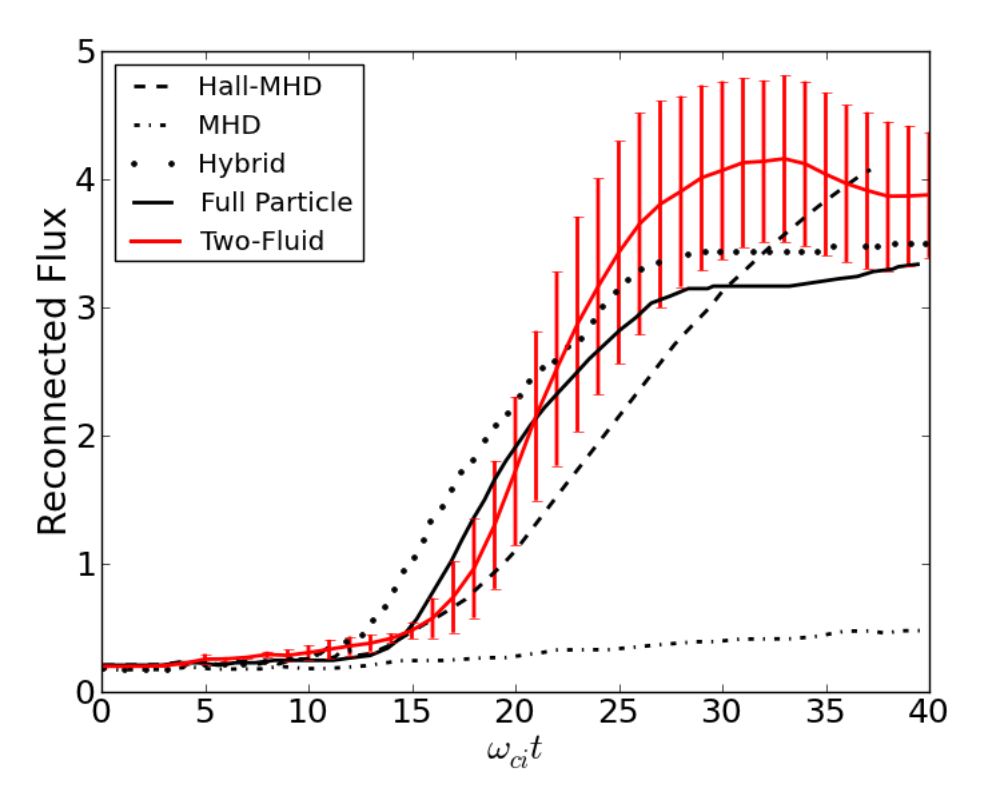


Figure 6.6: Reconnected flux plotted versus time for different plasma models used in the GEM challenge paper [2] compared to two-fluid model. The error bars represent the uncertainty due to the sensitivity in the c/v_A as measured using the MMC method in Fig. 6.3. The Two-fluid region of certainty encompass the full particle case and most of the hybrid reconnected flux, while the Hall-MHD case is almost completely outside the region of confidence.

third (37.3%) of the MMC method over the standard MC method and a smaller variance. The PC method has a total CPU time of 4660 CPU-hours (33 simulations at 512×128 resolution) which is 14.4% more computationally expensive as the MMC.

Figure 6.6 compares the reconnected flux computed by the different plasma models given in Ref. [2] and the reconnected flux computed by the two-fluid plasma model. The MHD and Hall-MHD models assume the speed of light is infinite while the hybrid, full particle, and two-fluid models assume a finite value. In the two-fluid case the standard deviation is plotted as the error bars to see the influence of varying the speed of light on the reconnected flux. Our results seem to be somewhere between the hybrid and the Hall-MHD models. The two-fluid plasma model results compare favorably with the full particle, Hall-MHD, and hybrid models. MHD has insufficient physics to capture collisionless reconnection.

6.7 Summary

A less costly method of obtaining the mean and variance of a numerical simulation with uncertainty in parameters is presented. The cost reduction comes from the fact that a large number of simulations are done at a coarse resolution which captures the variance of the uncertainty, and few simulations are done at a fine resolution which resolves the mean accurately. Coarse resolution simulations are computationally inexpensive, while the finer ones are more expensive but only a few are needed. Less costly computation of the region of validity of simulation results allow for the comparison of numerical and computational values more accurately and for better computer models validation.

Chapter 7

OPEN BOUNDARY CONDITIONS

7.1 Prior and Foundational Work

One method that has been used to simulate open boundary conditions is the Perfectly Matched Layers (PML)[30]. In the PML method an absorbing layer is added at the domain boundary, which absorbs and dissipates incoming waves while reducing reflections. This is done by first matching the impedance of the computation domain and the absorbing layer to eliminate reflections and achieve 100% transmission of the incoming waves. Once the waves have been transmitted to the layer, they are dampened, i.e. the PML acts as a lossy medium. This method has been developed extensively for electromagnetics problems in the frequency [85] and time domain [86]. The method is successful at eliminating refection. However, PML's become unstable when integrated over long time intervals and exacerbate the problem of accumulation of error in long-term numerical simulations [87].

Another method used for hyperbolic partial differential equation systems with sharp aft fronts is the lacuna-based open boundary conditions (LOBC)[29]. Lacuna is a region in space that, after being disturbed by a traveling wave, has returned to its original condition. The basic idea is that, any finite size domain will fall within the lacuna of any traveling wave if enough time has been elapsed. Therefore, any change to a traveling wave will not affect its lacuna which contains the computational domain of interest.

The advantage of the lacuna method is that it allows for stable long-term integration of the equations driven by continuously operating sources without accumulation of numerical error. The method is also non-local in space and time, and can be applied to any geometry domain. The implementation of this method requires the creation of an auxiliary grid/domain that overlaps with computational grid of interest at the boundary that is open. Any incoming waves to this boundary are transmitted to the auxiliary grid, which in turn provides the required closure (boundary condition) for the computational domain. Once the

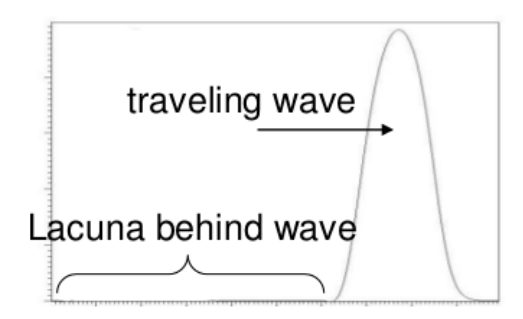


Figure 7.1: Lacuna are still regions present in wave-like solutions on odd-dimension spaces.

computational domain is in the lacuna of the traveling waves a reintegration of the auxiliary domain is done and the earlier sources used to transmit the wave into the auxiliary domain are removed. This guarantees that the waves are completely removed from the problem without ever being reflected into the computational domain. Larger auxiliary domains require less often reintegration, and smaller auxiliary domains require fewer computations and lower memory usage.

By combining the PML and the lacuna-based open boundary conditions, the disadvantages of both schemes are addressed. This is done by adding a PML in the auxiliary domain of the lacuna-based method. The advantage is that the auxiliary domain can be smaller in size because the PML dampens the incoming waves which otherwise would have reflected into the computational domain of a lacuna only method. In addition, smaller auxiliary domains require less computations and memory usage. The PML in the auxiliary domain is reset every time the auxiliary domain is reintegrated which prevents it from going unstable.

Therefore, in combining these two method, a new open boundary methodology is created that is stable and does not accumulate errors over time, is nonlocal in space and time, can be applied to any arbitrarily shape computational grid, and is not computational expensive nor memory demanding.

7.2 The Lacuna-based Open Boundary Condition (LOBC)

For the implementation of the LOBCs, the original infinite-domain problem is split into an interior and an auxiliary sub-domains. The interior problem becomes the bounded computational region of interest, whereas the auxiliary problem models an infinite domain. The two problems are dependent on each other. The sources for the auxiliary problem depend on the interior solution, and the solution of the auxiliary problem provides the required boundary conditions for the interior one [29].

This still leaves the auxiliary problem defined in an infinite domain. There, any changes applied to a propagating wave will not affect its lacuna (the interior domain). Therefore, a reintegration of the solution can be done in which "sufficiently" earlier sources of the wave is removed.

The interior problem is evolved using hyperbolic equations in balance law form, given by Eq. (2.39), and the auxiliary domain is evolved using,

$$\frac{\partial \mathbf{w}}{\partial t} + \nabla \cdot \mathbf{F}(\mathbf{w}) = S(\mathbf{w}) + \Omega(\mathbf{Q}). \tag{7.1}$$

The auxiliary source term $\Omega(\mathbf{Q})$, in Eq. (7.1), couples the interior solution to the auxiliary one. This source is solely dependent on values in a transition region; the location where the two domains overlap. To calculate this source, an auxiliary function, $\mu(x)$, is needed to guarantee that the two problems match at the boundary between the interior and exterior domain, while making the transition smooth, as shown in Fig. (7.2). This function is $\mu(x) = 1$ in the exterior domain and $\mu(x) = 0$ in the interior domain except the transition region, where $\mu(x)$ varies from zero to one smoothly and be C^1 continuous everywhere. The interior variable \mathbf{Q} and the auxiliary variable \mathbf{w} are related through $\mu(x)$ as $\mathbf{w} = \mu(x)\mathbf{Q}$.

Solving Eq. (7.1) for the time derivative, substituting $\mathbf{w} = \mu(x)\mathbf{Q}$, and noting that μ is only a function of position, the following relation is obtained

$$\mu \frac{\partial \mathbf{Q}}{\partial t} = -\nabla \cdot \mathbf{F}(\mu \mathbf{Q}) + S(\mu \mathbf{Q}) + \Omega(\mathbf{Q}), \tag{7.2}$$

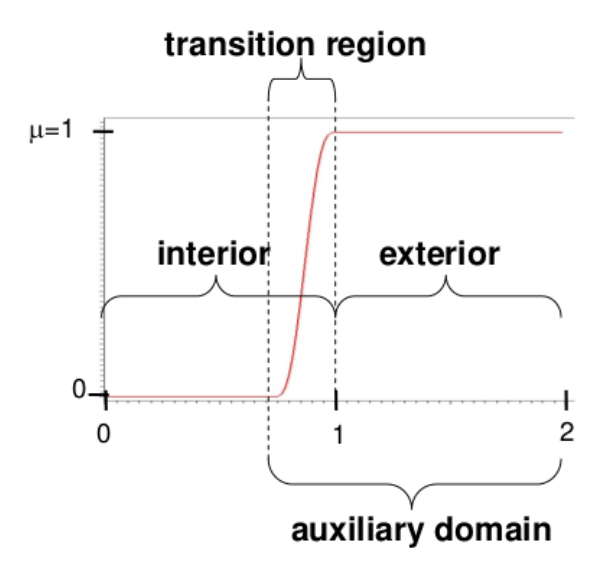


Figure 7.2: The transition function $\mu(x)$ varies from zero in the interior domain to one in the exterior domain and is C_o and C_1 continuous.

substituting Eq. (2.39) into Eq. (7.2) leads to an expression of the auxiliary source

$$\Omega(\mathbf{Q}) = \nabla \cdot F(\mu \mathbf{Q}) - S(\mu \mathbf{Q}) - \mu \nabla \cdot F(\mathbf{Q}) + \mu S(\mathbf{Q}). \tag{7.3}$$

For homogeneous problems where fluxes and sources that are linear functions of \mathbf{q} , the calculation of the auxiliary source can be reduced to $\Omega(\mathbf{Q}) = F \cdot \nabla \mu$.

Another important step of this method is referred to as the temporal re-integration of the auxiliary sources described in Ref. [88]. Waves in the auxiliary domain, can themselves be reflected from the exterior boundaries which can eventually re-enter the interior domain. To avoid this, a reintegration of the auxiliary sources is performed at constant time intervals, and earlier contributions to the auxiliary sources are removed. Since the interior domain is in the lacuna of such contributions any removal of auxiliary source does not affect the interior solution.

To better understand this process consider the following. Suppose that at $t = t_0$ and step n = 0 the source Ω_0 is generated and at every subsequent time step, n, the equivalent source Ω_n is generated. After the simulation has been elapsed for $t = T_N$ the source Ω_N

has been generated. At this point it can be deemed that sufficient time has passed and the computational (interior) domain is in the lacuna of the wavelet that the sources from $n = 0...n_r$ ($n_r < N$) are no longer affect the interior solution. Therefore, the re-integration of the auxiliary domain can be done following Eq. (7.1) to attain the new solution at $t = T_N$

$$\mathbf{w}|_{t_N} = \int_{t_{n_r}}^{T_N} \frac{\partial \mathbf{w}}{\partial t} dt = \mathbf{w}|_{t_{n_r}} + \sum_{i=n_r}^{N} \int_{t_{n_r}}^{T_N} \left(-\nabla \cdot \mathbf{F}(\mathbf{w}) + S(\mathbf{w}) + \Omega_i \right) dt.$$
 (7.4)

Equation (7.4) gives the auxiliary solution from the beginning of the simulation to the current time. All the sources from timesteps $n=0...n_r-1$ are ignored and only the sources from $n=n_r...N$ are used, that means $\mathbf{w}|_{t_{n_r}}=0$. Only the source contributions from $n=n_r...N$ are retained. If each source contribution can be viewed as being a discrete value, Ω_i , integrating each contribution from time $t=t_n$ to $t=t_N$ gives the current solution due to the earlier source. Therefore, if all the contributions from all the discrete values of the source from $n=n_r$ to n=N are added up, the solution $\mathbf{w}|_{t_N}$ at $t=t_N$ is obtained without the earlier sources. This reintegration guarantees that no waves re-enter the interior domain after they have completely exited it. It is not practical to do the reintegration every time step. The maximum time that the wavelet can propagate without re-entering the interior domain is denoted as the reintegration time (T_{ri}^{max}) ; this value depends on the size of the exterior domain, d_{ext} , and the fastest traveling speed in the system, c

$$T_{ri}^{max} = \frac{2d_{ext}}{c}. (7.5)$$

The implementation is as follows,

- 1. Integrate Eq. (2.39) and get \mathbf{Q} in the interior domain;
- 2. Calculate the auxiliary source using \mathbf{Q} and Eq. (7.3);
- 3. Integrate Eq. (7.1) using the auxiliary source and obtain \mathbf{w} ;
- 4. Use the new \mathbf{w} to apply the boundary conditions to \mathbf{Q} ;

- 5. Within a temporal interval less that T_{ri}^{max} reintegrate **w** using Eq. (7.4).
- 6. Goto step 1

7.3 Application of the LOBCs to Maxwell Equations

The LOBCs are applied to 2D electromagnetic pulse using the Washington Approximate Riemann Plasma Solver (WARPX) using a finite volume formulation [16]. The problem is formulated using a perfectly hyperbolic representation of the Maxwell's equations to account for divergence error corrections described in Sec. (2.3).

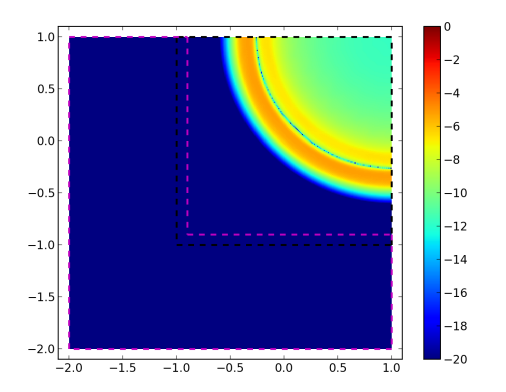
For the current problem, a cylindrical electromagnetic pulse propagates radially outwards through free space. The computational domain is define as -1 < x, y < 1. The LOBCs are applied at x = -1 and y = -1. The initial conditions are given by

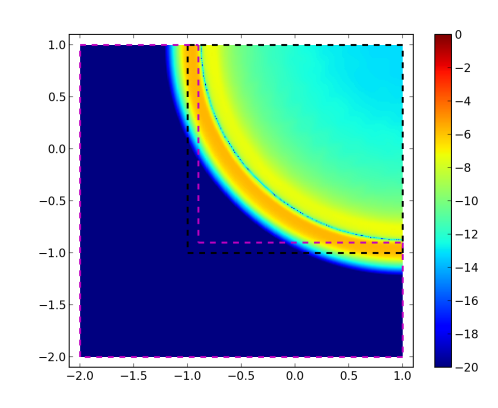
$$\begin{bmatrix} E_x \\ E_y \\ E_z \\ B_x \\ B_y \\ B_z \end{bmatrix} = \begin{bmatrix} 0 \\ 0 \\ 0 \\ 0 \\ \exp\left[-100\left((x-1)^2 + (y-1)^2\right)\right] \end{bmatrix}.$$
 (7.6)

For the simulations, in Fig. 7.3, the boundary conditions at y = 1.0 and x = 1.0 are symmetric, and y = -2.0 and x = -2.0 are Dirichlet and set to zero. Time is normalized using the combined length of the interior and the exterior domain and the speed of light, $t = \frac{L}{c}$.

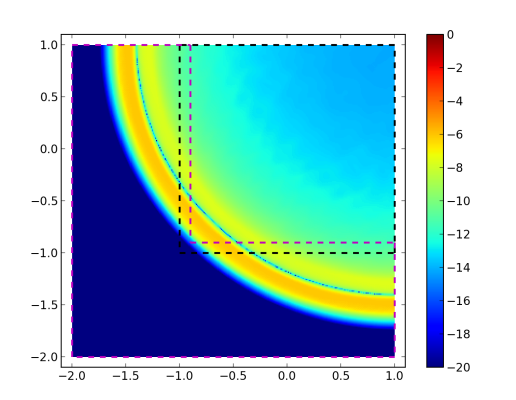
Figure 7.3 shows the pulse at time t = 0.438, 0.642, 0.836, 0.846 at which point the first reintegration occurs. The pulse is sourced into the auxiliary domain with no reflections and the two solution match exactly along x = -1.0 and y = -1.0. Once the interior problem is in the lacuna of the pulse, then the auxiliary problem is reintegrated and the earlier sources are removed from the auxiliary problem.

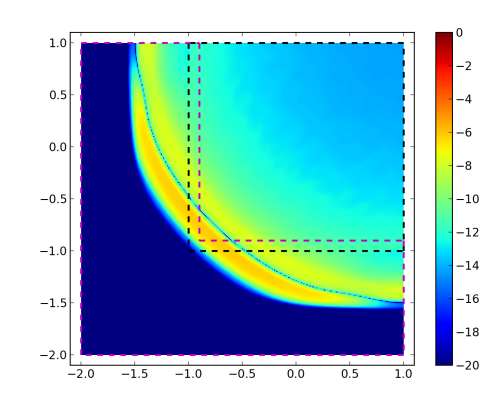
Figure 7.4 compares the results of the problem described above, to a case where zero





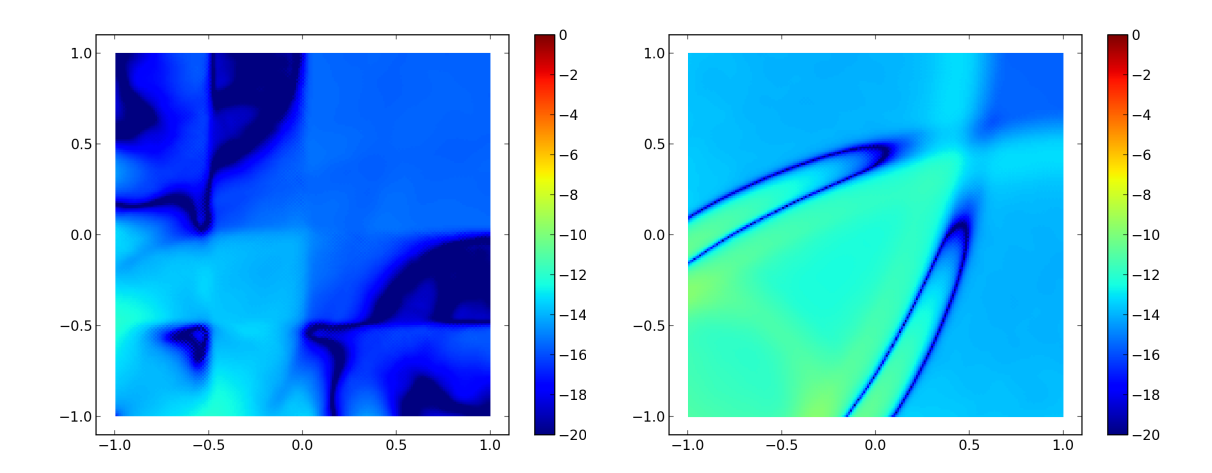
- (a) An electromagnetic pulse traveling though free space. t=0.438
- (b) The pulse is transmitted to the auxiliary domain. t=0.642





- (c) Right before the first reintegration occurs. t=0.836
- (d) The first reintegration occurs and the earlier sources are removed from the auxiliary domain. t=0.846

Figure 7.3: A cylindrical pulse propagates through free space, plot of the $\log |B_z|$. The black dashed lines show the limit of the interior domain and the purple dashed lines delimit the auxiliary domain. The top and right side boundary conditions are conducting walls. There are no reflections from the boundaries.



- (a) Interior domain reflections using the lacuna- (b) Computational domain reflections using the based LOBC.
 - Zero Normal Gradient BC.

Figure 7.4: Plot of $\log |B_z|$ at t = 1.168. In the ZNG there are considerably large reflections from the boundaries while the LOBC the reflections extremely small, in the other of 10^{-16} .

normal gradient (ZNG) boundary conditions are used instead of LOBC. The $\log B_z$ is plotted at t = 1.168. The reflections in the LOBC have a magnitude of about 10^{-13} while the ZNG has a magnitude of about 10^{-9} . Showing that the LOBC produces much better results when simulating open boundary conditions.

Figure 7.5 plots the logarithm of the maximum magnitude of magnetic field $(\max(\log |\mathbf{B}|))$ as the pulse propagates out of the interior domain. The solution using the lacuna boundary condition is compared to the ZNG boundary condition. The profiles of the two implementations coincide before the pulse reaches the boundary at t = 2/3. Afterward, the ZNG boundary condition reflects portions of the pulse and it has a much slower decrease in magnetic field magnitude.

Therefore, it has been shown that the lacuna based open boundary conditions are able to simulate infinite domain without developing instabilities like PML and, when compared to the ZNG BC, produces a much better results eliminating boundary reflection.

For problems that occur at long time scales, multiple reintegrations of the auxiliary domain are needed. For the problem described in this section the $\Delta T_{max} = L_{ext}/c = 2$.

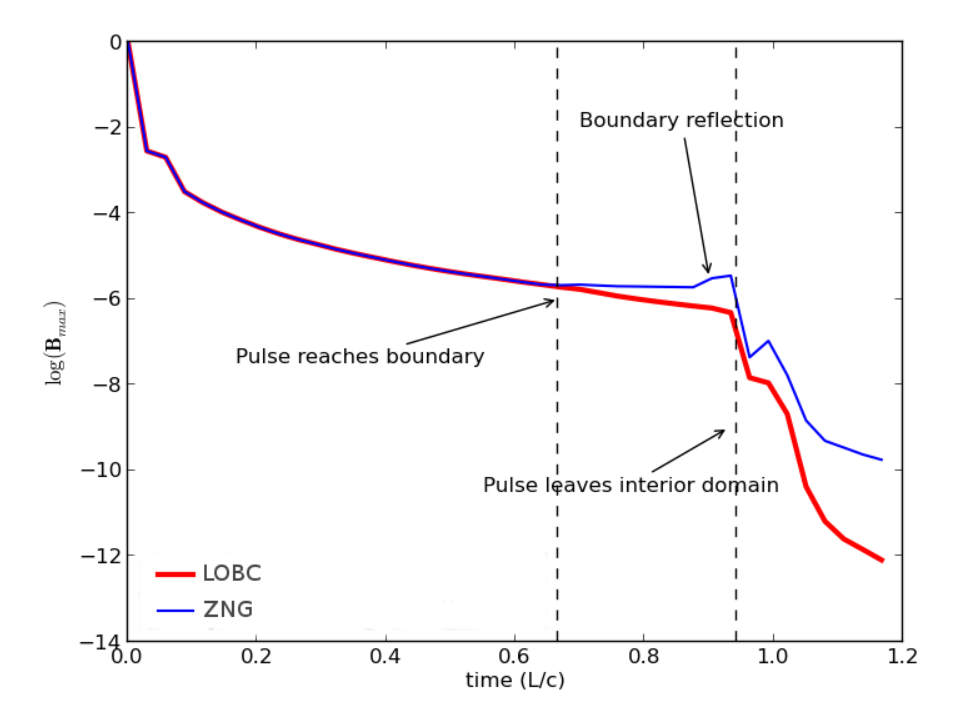


Figure 7.5: The logarithm of maximum value of the magnetic field magnitude is plotted versus the elapsed simulation time. The ZNG method produces reflection when the pulse reaches the boundaries while the LOBC does not.

For smaller exterior domains the reintegration has to occur more frequent, and for larger ones more memory is need to store the auxiliary sources. Therefore, there is a compromise between the frequency of reintegration and exterior domain size used. One way to eliminate this dependence is described in the next section.

Combined Application of PMLs and LOBCs to Maxwell's Equations

Adding PML at the outer boundary of the auxiliary domain of a LOBC implementation, is done to solve two problems: to reduce the frequency of reintegration of the LOBC, and by doing so resetting the PML to prevent it from going unstable.

For the current implementation an unspilt PML is used for the 2D Maxwell's equations. The PML is applied in the x-direction boundaries. The PML implemented here is the physically motivated PML [31]

$$\frac{\partial E_x}{\partial t} = \frac{\partial H_z}{\partial y} + \sigma(E_x - P) \tag{7.7}$$

$$\frac{\partial E_y}{\partial t} = -\frac{\partial H_z}{\partial x} - \sigma E_y \qquad (7.8)$$

$$\frac{\partial H_z}{\partial t} = \frac{\partial E_x}{\partial y} - \frac{\partial E_x}{\partial y} - \sigma H_z \qquad (7.9)$$

$$\frac{\partial H_z}{\partial t} = \frac{\partial E_x}{\partial u} - \frac{\partial E_x}{\partial u} - \sigma H_z \tag{7.9}$$

$$\frac{\partial P}{\partial t} = \sigma(E_x - P). \tag{7.10}$$

where P is nonzero only in the PML. The wave dampening is controlled by the variable $\sigma(x) = (x-a)^3/d^3$, d the PML thickness, and a is the location of the PML boundary.

The goal is to compare the performance of a PML only application (on the right) versus a combined PML-LOBC one (on the left), as illustrated in Fig. 7.6: the regions in magenta are the extend of the PMLs and the region in gray is the exterior domain of the POBC. The problem is initialized according to Ref. [87] on a computational domain $\{(x,y)|-50 \le$ $x \le 110, -50 \le y \le 50$ } d = 10, and $\Delta x = \Delta y = 1$, and the fields are initialized as

$$H_z(x, y, t = 0) = \begin{cases} \cos^8 \left(\frac{\pi \sqrt{x^2 + y^2}}{2r_o} \right) & \text{if } \sqrt{x^2 + y^2} \le r_o, \\ 0 & \text{if } \sqrt{x^2 + y^2} > r_o. \end{cases}$$
(7.11)

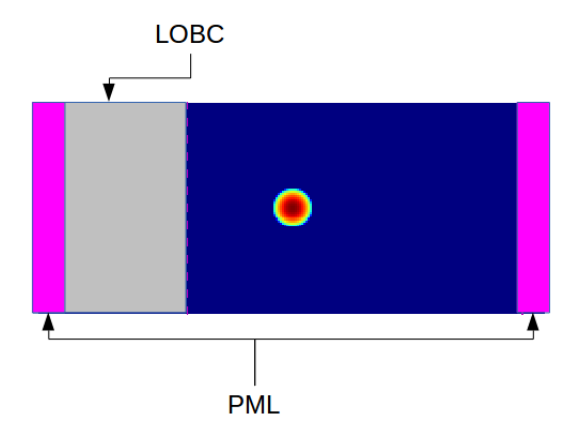


Figure 7.6: A combined PML-LOBC is applied to the left boundary while a PML-only BC is used to the right boundary. The region in gray is the exterior domain of the LOBC, and both region in magenta represent the PMLs. The domain of interest is in blue with the initialization in orange. Top and bottom BCs are reflecting walls.

where $r_o = 10$ and $\mathbf{E}(x, y, t = 0) = \mathbf{0}$.

In Fig. 7.7(a), the PML instability has begun to develop on the right side PML while the left side PML has been reset by the reintegration of the auxiliary domain in the LOBC. In Fig. 7.7(b) another reintegration has been done in the auxiliary domain and the left side PML has again been reset, while the right side PML instability has contaminated the computational domain, rendering the solution there useless.

7.5 Summary

It has been shown that the LOBC produces significantly less reflections from the boundary than the ZNG boundary conditions, a decrease of four orders of magnitude. In addition, the LOBC was combined with a PML to address the disadvantages of both methods. The LOBC requires frequent reintegrations of the solution in the auxiliary domain depending on its size, and the PML goes unstable in problems that are integrated over long time intervals. By adding a PML at the outer boundary of the auxiliary domain of a LOBC the reintegration is no longer dependent on the domain size and reintegration is required less frequently, which reduces computational effort and memory usage. In addition, every time the reintegration is done the PML is reset preventing it from going unstable. Therefore, the

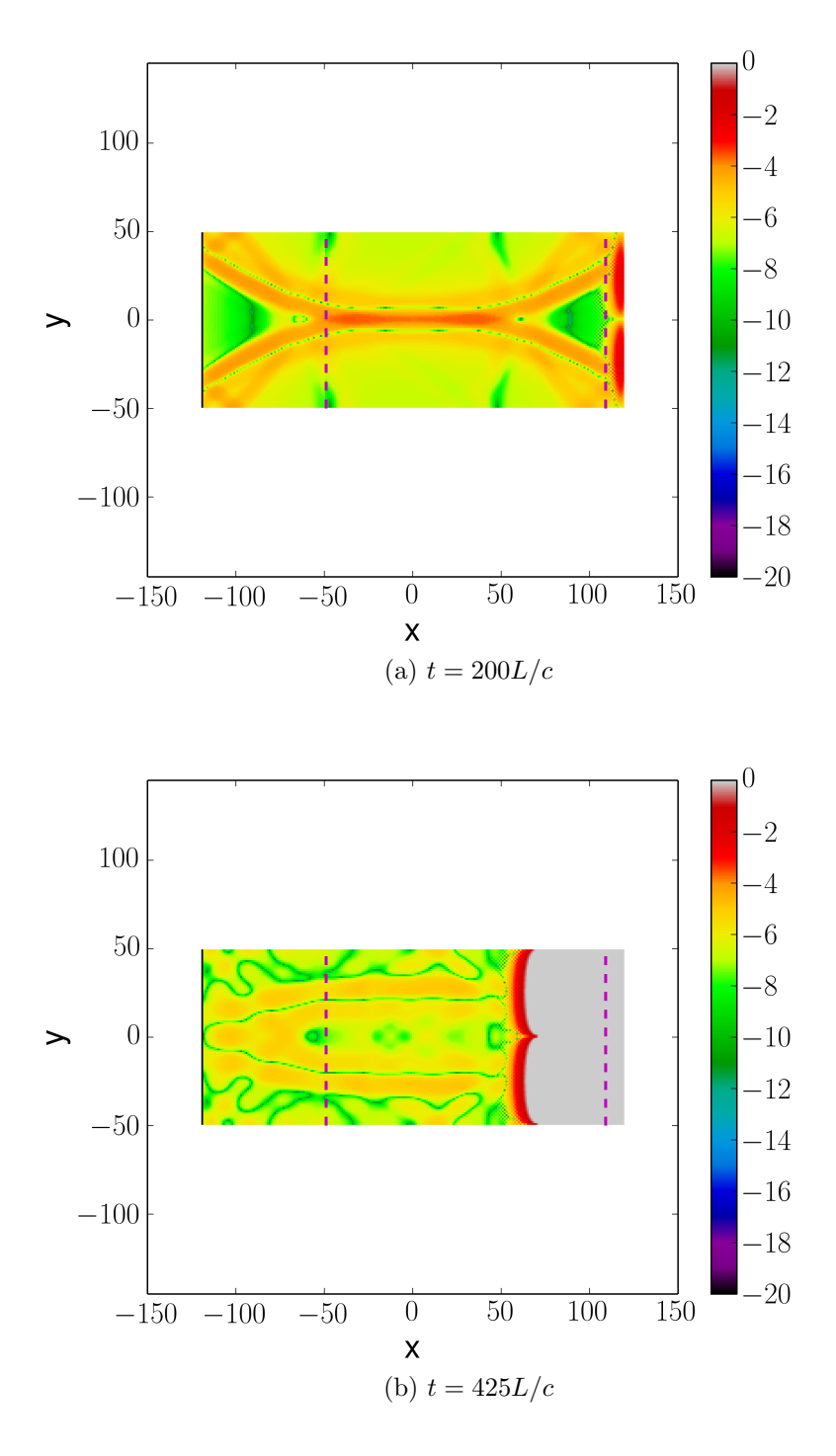


Figure 7.7: Plot of $\log |H_z|$. Top and bottom boundary conditions are reflecting. The right BC is a simple PML and the left BC are a mixed PML and Lacuna. (a) Shows that the PML has become unstable in the right boundary, while at the left boundary the reintegration of the auxiliary domain has reset the PML, removing the instability. (b) The PML instability has contaminated the computational domain on the right boundary, while the left boundary still behaves as intended with no reflections nor instabilities.

combined PML and LOBC method can be applied to any geometry domain, is non-local in space and time, considerably reduces reflection from the boundaries, and can be used in long running problems at moderate computational effort and reduced memory usage.

Chapter 8

CONCLUSION

The multi-fluid plasma model (MFPM) has been presented. The MFPM is a generalization of the MHD model that retains the electron dynamics and a finite speed of light. The model is derived from the kinetic description of a plasma by assuming local thermodynamical equilibrium within each of the species.

Multiscale effects are present in the MFPM, which is a manifestation of the large mass difference between the electron and ion species. In order to properly model the physics of the MFPM, an efficient numerical method have to be developed, the blended finite element method (BFEM). The BFEM uses a discontinuous Galerkin representation for the ion and neutral fluids with an explicit time integration. The electrons and electromagnetic fields are discretized using a continuous Galerkin representation, and the time integrated is done using an implicit method. The method is high order accurate and highly efficient. Verification of the BFEM is done using simple test problems as well as for more complex multi-fluid problems.

The BFEM is applied to the problem of inertial confinement fusion (ICF) fuel species separation. The problem initialization is based on experimental results from OMEGA, but simplified to a shock-tube-like problem. Deuterium-tritium separation and its effect on neutron yield is investigated. The results show that there is considerable separation of the deuterium from the tritium and that the separation is dominated by the pressure gradient. Electric fields in the order of Gigavolts per meter develop, but the forces they produce are small in comparison to the pressure gradients. Inter-species collisionality decreases as the plasma approaches the center of the capsule, and the Knudsen number increase indicating a transition from a fluid to a kinetic description of the plasma. In addition, the separation causes the neutron yield to be reduced compared to a mass-average fluid simulation. The neutron yield measured are on the same order of magnitude as experimental results.

Uncertainty quantification techniques are applied to the well-studied problem of magnetic reconnection. Studies of the sensitivity of the reconnected flux to uncertainties in ion-to-electron mass ratio, speed of light to Alfvén speed ratio, and the magnitude of the initial magnetic flux perturbation are done. Three uncertainty quantification methods are compared for accuracy and computational cost. The Multi-level Monte Carlo (MMC) method performs better than the other methods and can capture the true mean and variance of the problems at relatively low computational cost. Therefore, the MMC method can be easy used to compare computational results with experimental data accurately, and at low cost.

Lacuna-based open boundary conditions (LOBC) are implemented in conjunction with the perfectly matched layer (PML) method to address the problem of numerical reflection when simulating open boundary conditions. The combined method of using the LOBC with PMLs at its boundaries address the shortcomings of both methods. The LOBC reintegration can be done less frequently, and the PML instabilities can be prevent from contaminating the computational domain. When the reintegration occurs, the PML is reset. The results show that this approach is successful in eliminating reflections, and is computationally efficient.

In summary, a novel numerical method, the blended finite element method, is introduced and demonstrated to effectively and efficiently model plasmas using the multi-fluid representation. The method is applied to standard benchmarks, and experimental configurations involving ICF conditions in an effort to answer some relevant questions in the field. The effects of uncertainty in simulations is quantified efficiently, accurately, and at low computational cost. And, in anticipation of further developments in this area of research, methods of treating open boundary conditions are investigated, and a new approach is presented. Together, the combined numerical methods and techniques offer a means of extending the capabilities of plasma physics simulations. In particular, they offer a high-fidelity and computationally efficient means of treating ICF-relevant physics, and provide a means of capturing multi-fluid effects in a way that is consistent, conservative, high-order accurate, and computationally viable.

8.1 Suggested Future Work

The inclusion of ionization and recombinations models to the multi-fluid plasma model is a natural next step, which would make the model more complete and extended it to a wider range of plasma conditions, for example ion-thrusters, plasma assisted combustion, or plasma actuators.

Future work for the BFEM include the study of better artificial dissipation models or other methods to dampen the high frequency oscillations associated with sharp gradients and discontinuities. In addition, the BFEM can easily be extended to higher dimensionality by calculating fluxes in the additional dimensions for DG representation and by calculating the flux Jacobian in the other directions for the CG portion.

For the ICF species separation problem, future work would include adding fusion reaction that occur in DT-plasma which would allow for the modeling of neutrons species at different energies and additional ions products of the fusion reactions. Accounting for reaction can then be used to measure the amount of the deuterium and tritium that fuses. In addition, better DT-reactivity models are need, which are dependent on separate deuterium and tritium temperatures instead of an averaged one. Fluid models that allow for departure from Maxwellian distributions (higher moment models) are desirable for regions where the Knudsen number is large which encompasses some regimes in inertial confinement fusion.

BIBLIOGRAPHY

- [1] U. Shumlak and J. Loverich. Approximate riemann solver for the two-fluid plasma model. *Journal of Computational Physics*, 187:620–638, 2003.
- [2] J. Birn, J. F. Drake, M. A. Shay, B. N. Rogers, R. E. Denton, M. Hesse, M. Kuznetsova, Z. W. Ma, A. Bhattacharjee, A. Otto, and P. L. Pritchett. Geospace environmental modeling (gem) magnetic reconnection challenge. *J. Geo. Res.*, 106(A3):3715–3719, March 2001.
- [3] S. Atzeni and J. Meyer ter Vehn. *Inertial Fusion*. Number 125 in International Series of Monographs on Physics. Oxford University Press.
- [4] F. F. Chen. Introduction to plasma physics and controlled fusion, volume 1. Plenum Press.
- [5] Hui Liu, Boying Wu, Daren Yu, Yong Cao, and Ping Duan. Particle-in-cell simulation of a hall thruster. *Journal of Physics D: Applied Physics*, 43(16):165202, 2010.
- [6] M G Haines. A review of the dense z -pinch. Plasma Physics and Controlled Fusion, 53(9):093001, 2011.
- [7] S.P. Hirshman and D.J. Sigmar. Neoclassical transport of impurities in tokamak plasmas. *Nuclear Fusion*, 21(9):1079, 1981.
- [8] P Helander, C D Beidler, T M Bird, M Drevlak, Y Feng, R Hatzky, F Jenko, R Kleiber, J H E Proll, Yu Turkin, and P Xanthopoulos. Stellarator and tokamak plasmas: a comparison. *Plasma Physics and Controlled Fusion*, 54(12):124009, 2012.
- [9] John D. Lindl, Peter Amendt, Richard L. Berger, S. Gail Glendinning, Siegfried H. Glenzer, Steven W. Haan, Robert L. Kauffman, Otto L. Landen, and Laurence J. Suter1. The physics basis for ignition using indirect-drive targets on the national ignition facility. *Physics of Plasmas*, 11:339, 2004.

- [10] M. M. Marinak, G. D. Kerbel, N. A. Gentile, O. Jones, D. Munro, S. Pollaine, T. R. Dittrich, and S. W. Haan. Three-dimensional HYDRA simulations of national ignition facility targets. *Physics of Plasmas*, 8(5), 2001.
- [11] S. P. Regan, R. Epstein, B. A. Hammel, L. J. Suter, J. Ralph, H. Scott, M. A. Barrios, D. K. Bradley, D. A. Callahan, C. Cerjan, G. W. Collins, S. N. Dixit, T. Doeppner, M. J. Edwards, D. R. Farley, S. Glenn, S. H. Glenzer, I. E. Golovkin, S. W. Haan, A. Hamza, D. G. Hicks, N. Izumi, J. D. Kilkenny, J. L. Kline, G. A. Kyrala, O. L. Landen, T. Ma, J. J. MacFarlane, R. C. Mancini, R. L. McCrory, N. B. Meezan, D. D. Meyerhofer, A. Nikroo, K. J. Peterson, T. C. Sangster, P. Springer, and R. P. J. Town. Hot-spot mix in ignition-scale implosions on the NIF. *Physics of Plasmas*, 19(5), 2012.
- [12] B. J. MacGowan, B. B. Afeyan, C. A. Back, R. L. Berger, G. Bonnaud, M. Casanova, B. I. Cohen, D. E. Desenne, D. F. DuBois, A. G. Dulieu, K. G. Estabrook, J. C. Fernandez, S. H. Glenzer, D. E. Hinkel, T. B. Kaiser, D. H. Kalantar, R. L. Kauffman, R. K. Kirkwood, W. L. Kruer, A. B. Langdon, B. F. Lasinski, D. S. Montgomery, J. D. Moody, D. H. Munro, L. V. Powers, H. A. Rose, C. Rousseaux, R. E. Turner, B. H. Wilde, S. C. Wilks, and E. A. Williams. Laser-plasma interactions in ignitionscale hohlraum plasmas. *Physics of Plasmas*, 3(5), 1996.
- [13] S. Atzeni, A. Schiavi, F. Califano, F. Cattani, F. Cornolti, D. Del Sarto, T.V. Liseykina, A. Macchi, and F. Pegoraro. Fluid and kinetic simulation of inertial confinement fusion plasmas. *Computer Physics Communications*, 169(1-3):153 159, 2005.
- [14] V. Yu. Glebov, D. D. Meyerhofer, T. C. Sangster, C. Stoeckl, S. Roberts, C. A. Barrera, J. R. Celeste, C. J. Cerjan, L. S. Dauffy, D. C. Eder, R. L. Griffith, S. W. Haan, B. A. Hammel, S. P. Hatchett, N. Izumi, J. R. Kimbrough, J. A. Koch, O. L. Landen, R. A. Lerche, B. J. MacGowan, M. J. Moran, E. W. Ng, T. W. Phillips, P. M. Song, R. Tommasini, B. K. Young, S. E. Caldwell, G. P. Grim, S. C. Evans, J. M. Mack, T. J. Sedillo, M. D. Wilke, D. C. Wilson, C. S. Young, D. Casey, J. A. Frenje, C. K. Li, R. D. Petrasso, F. H. Sguin, J. L. Bourgade, L. Disdier, M. Houry,

- I. Lantuejoul, O. Landoas, G. A. Chandler, G. W. Cooper, R. J. Leeper, R. E. Olson, C. L. Ruiz, M. A. Sweeney, S. P. Padalino, C. Horsfield, and B. A. Davis. Development of nuclear diagnostics for the national ignition facility (invited). *Review of Scientific Instruments*, 77(10), 2006.
- [15] R.J. Hawryluk, D.J. Campbell, G. Janeschitz, P.R. Thomas, R. Albanese, R. Ambrosino, C. Bachmann, L. Baylor, M. Becoulet, I. Benfatto, J. Bialek, A. Boozer, A. Brooks, R. Budny, T. Casper, M. Cavinato, J.-J. Cordier, V. Chuyanov, E. Doyle, T. Evans, G. Federici, M. Fenstermacher, H. Fujieda, K. G'al, A. Garofalo, L. Garzotti, D. Gates, Y. Gribov, P. Heitzenroeder, T.C. Hender, N. Holtkamp, D. Humphreys, I. Hutchinson, K. Ioki, J. Johner, G. Johnson, Y. Kamada, A. Kavin, C. Kessel, R. Khayrutdinov, G. Kramer, A. Kukushkin, K. Lackner, I. Landman, P. Lang, Y. Liang, J. Linke, B. Lipschultz, A. Loarte, G.D. Loesser, C. Lowry, T. Luce, V. Lukash, S. Maruyama, M. Mattei, J. Menard, M. Merola, A. Mineev, N. Mitchell, E. Nardon, R. Nazikian, B. Nelson, C. Neumeyer, J.-K. Park, R. Pearce, R.A. Pitts, A. Polevoi, A. Portone, M. Okabayashi, P.H. Rebut, V. Riccardo, J. Roth, S. Sabbagh, G. Saibene, G. Sannazzaro, M. Schaffer, M. Shimada, A. Sen, A. Sips, C.H. Skinner, P. Snyder, R. Stambaugh, E. Strait, M. Sugihara, E. Tsitrone, J. Urano, M. Valovic, M. Wade, J. Wesley, R. White, D.G. Whyte, S. Wu, M. Wykes, and L. Zakharov. Principal physics developments evaluated in the iter design review. Nuclear Fusion, 49(6):065012, 2009.
- [16] U. Shumlak, R. Lilly, N. Reddell, E. Sousa, and B. Srinivasan. Advanced physics calculations using a multi-fluid plasma model. *Computer Physics Communications*, 182(9):1767 – 1770, 2011.
- [17] J. P. Freidberg. Ideal magnetohydrodynamic theory of magnetic fusion systems. Rev. Mod. Phys, 54(801), 1982.
- [18] Ammar Hakim. High-resolution Wave Propagation Schemer for Two-Fluid Plasma Simulations. PhD thesis, University of Washington, 2006.
- [19] A. Hakim, J. Loverich, and U. Shumlak. A high resolution wave propagation scheme

- for ideal two-fluid plasma equations. *Journal of Computational Physics*, 219:418–442, 2006.
- [20] B. Srinivasan, A. Hakim, and U. Shumlak. Numerical methods for two-fluid dispersive fast mhd phenomena. Commun. Comput. Phys., 10(1):183–215, 2011.
- [21] J. Loverich, A. Hakim, and U. Shumlak. A discontinuous galerkin method for ideal two-fluid plasma equations. Commun. Comput. Phys., 9(240), 2011.
- [22] B. Cockburn and C. W. Shu. Runge-Kutta discontinuous Galerkin methods for convection-dominated problems. *Journal of Scientific Computing*, 16(3):173–261, 2001.
- [23] B. Srinivasan. Numerical Methods for 3-dimensional Magnetic Confinement Configurations using Two-Fluid Plasma Equations. PhD thesis, University of Washington, 2010.
- [24] S. C. Jardin. A triangular finite element with first-derivative continuity applied to fusion mhd applications. *Journal of Computational Physics*, 200(1):133–152, 2004.
- [25] D. T. Casey, J. A. Frenje, M. Gatu Johnson, M. J. E. Manuel, H. G. Rinderknecht, N. Sinenian, F. H. Séguin, C. K. Li, R. D. Petrasso, P. B. Radha, J. A. Delettrez, V. Yu Glebov, D. D. Meyerhofer, T. C. Sangster, D. P. McNabb, P. A. Amendt, R. N. Boyd, J. R. Rygg, H. W. Herrmann, Y. H. Kim, and A. D. Bacher. Evidence for Stratification of Deuterium-Tritium Fuel in Inertial Confinement Fusion Implosions. *Physical Review Letters*, 108(075002), 2012.
- [26] M. B. Giles. Multilevel monte carlo path simulation. Operations Research, 56(3):981–986, 2008.
- [27] George Kuczera and Eric Parent. Monte carlo assessment of parameter uncertainty in conceptual catchment models: the metropolis algorithm. *Journal of Hydrology*, 211(1-4):69 – 85, 1998.

- [28] K. A. Cliffe, M. B. Giles, R. Scheichl, and A. L. Teckentrup. Multilevel monte carlo methods and applications to elliptic pdes with random coefficients. 2011.
- [29] S. V. Tsynkov. On the application of lacunae-based methods to maxwell's equations. J. Comput. Phys., (199):126–149, 2004.
- [30] J. P. Berenger. A perfectly matched layer for the absorption on electromagnetic waves. Journal of Computational Physics, 114:185–200, 1994.
- [31] S. Abarbanel, D. Gottlieb, and J. S. Hesthaven. Long time behavior of the perfectly matched layer equations in computational electromagnetics. *Journal of Scientific Computing*, 17:405–422, 2002.
- [32] U. Shumlak, R. Lilly, N. Reddell, E. Sousa, and B. Srinivasan. Advanced Physics Calculations using a Multi-Fluid Plasma Model. Computer Physics Communications, 18:1767–1770, 2011.
- [33] E.T. Meier and U. Shumlak. A general nonlinear fluid model for reacting plasmaneutral mixtures. *Physics of Plasmas*, 19(072508), 2012.
- [34] S.L. Braginskii. Transport processes in plasma. In Achad M. A. Leontovich, editor, Reviews of Plasma Physics, pages 205–311. Consultants Bureau, 1965.
- [35] H. Yemin and H. Xiwei. The properties and structure of a plasma non-neutral shock. *Physics of Plasmas*, 10(7), 2003.
- [36] D. R. Gray and J. D. Kilkenny. The measurement of ion acoustic turbulence and reduced thermal conductivity caused by a large temperature gradient in a laser heated plasma. *Plasma Physics*, 22:81–111, 1980.
- [37] R. Schneider C. D. Munz, P. Omnes, E. Sonnendruer, and U. Voss. Divergence correction techniques for maxwell solvers based n a hyperbolic model. *Journal of Computational Physics*, 161:484–511, 2000.
- [38] R. J. LeVeque. Finite Volume Methods for Hyperbolic Problems. Cambridge University Press, 1st edition, 2002.

- [39] R. J. LeVeque and D. L. George. High-resolution finite volume methods for the shallow water equations with bathymetry and dry states. In C. Synolakis P. L-F. Liu, H. Yeh, editor, Advanced Numerical Models for Simulationg Tsunami Waves and Runup, pages 43–73, 2007.
- [40] R. J. LeVeque. Finite volume methods for nonlinear elasticity in heterogeneous media. Int. J. Numer. Meth. Fluids, (93-104), 2002.
- [41] R. J. LeVeque. Tsunami modeling. to appear in the Princeton Companion to Applied Mathematics (N. J. Higham, Editor).
- [42] A. Hakim and U. Shumlak. High resolution wave propagation scheme for ideal two-fluid plasma equations. *Journal of Computational Physics*, 219(1):418–442, 2006.
- [43] C.R. Sovinec, A.H. Glasser, T.A. Gianakon, D.C. Barnes, R.A. Nebel, S.E. Kruger, D.D. Schnack, S.J. Plimpton, A. Tarditi, and M.S. Chu. Nonlinear magnetohydrodynamics simulation using high-order finite elements. *Journal of Computational Physics*, 195(1):355 386, 2004.
- [44] N.A. Murphy, A.K. Young, C. Shen, J. Lin, and L. Ni. The plasmoid instability during asymmetric inflow magnetic reconnection. *Physics of Plasmas*, 20(6), 2013.
- [45] V. A. Izzo. Impurity mixing and radiation asymmetry in massive gas injection simulations of diii-d. *Physics of Plasmas*, 20(5), 2013.
- [46] John Slough and Richard Milroy. High flux frc facility for stability and confinement studies. *Journal of Fusion Energy*, 29(6):567–570, 2010.
- [47] Angus I.D. Macnab and Simon Woodruff. Extended mhd simulations of the compression and stability of spheromaks for current drive. *Journal of Fusion Energy*, 28(2):183–186, 2009.
- [48] S.C. Jardin, J. Breslau, and N. Ferraro. A high-order implicit finite element method for integrating the two-fluid magnetohydrodynamic equations in two dimensions. *Journal* of Computational Physics, 226(2):2146 – 2174, 2007.

- [49] L. Chacón, D.A. Knoll, and J.M. Finn. An implicit, nonlinear reduced resistive MHD solver. *Journal of Computational Physics*, 178(1):15 36, 2002.
- [50] H. W. Reed and T. R. Hill. Triangular mesh methods for the neutron transport equation. Los Alamos Scientific Laboratory Report LA-UR-73-479, 1973.
- [51] B. Cockburn and C. W. Shu. Tvb runge-kutta local projection discontinuous galerkin finite element for conservation laws ii-general framework. *Math. Comput.*, 52(186):411– 435, 1989.
- [52] F. Bassi and S. Rebay. A high-order accurate discontinuous finite element method for the numerical solution of the compressible navierstokes equations. *Journal of Computational Physics*, 131:267–279, 1997.
- [53] F. Bassi, L. Botti, A. Colombo, and S. Rebay. Agglomeration based discontinuous galerkin discretization of the euler and navierstokes equations. *Computers and Fluids*, 61(0):77 – 85, 2012.
- [54] E. Ferrer and R.H.J. Willden. A high order discontinuous galerkin finite element solver for the incompressible navierstokes equations. Computers and Fluids, 46(1):224 – 230, 2011.
- [55] Philipp Birken, Gregor Gassner, and Mark. Preconditioning for modal discontinuous galerkin methods for unsteady 3d navierstokes equations. *Journal of Computational Physics*, 240(0):20 35, 2013.
- [56] Fengyan Li, Liwei Xu, and Sergey Yakovlev. Central discontinuous galerkin methods for ideal {MHD} equations with the exactly divergence-free magnetic field. *Journal* of Computational Physics, 230(12):4828 – 4847, 2011.
- [57] V. Wheatley, H. Kumar, and P. Huguenot. On the role of riemann solvers in discontinuous galerkin methods for magnetohydrodynamics. *Journal of Computational Physics*, 229(3):660 680, 2010.

- [58] James A. Rossmanith and David C. Seal. A positivity-preserving high-order semilagrangian discontinuous galerkin scheme for the vlasovpoisson equations. *Journal of Computational Physics*, 230(16):6203 – 6232, 2011.
- [59] J. Crank and P. Nicholson. A Partial Method for Numerical Evaluation of Solutions of Partial Differential Equations of the Heat-Conduction Type. Advances in Computational Mathemathics, 6:207–226, 1996.
- [60] J. N. Reddy. An Introduction to the Finite Element Method. McGraw-Hill, 3rd edition.
- [61] Satish Balay, Shrirang Abhyankar, Mark F. Adams, Jed Brown, Peter Brune, Kris Buschelman, Victor Eijkhout, William D. Gropp, Dinesh Kaushik, Matthew G. Knepley, Lois Curfman McInnes, Karl Rupp, Barry F. Smith, and Hong Zhang. PETSc users manual. Technical Report ANL-95/11 Revision 3.5, Argonne National Laboratory, 2014.
- [62] Assefaw Hadish Gebremedhin, Fredrik Manne, and Alex Pothen. What color is your jacobian? graph coloring for computing derivatives. SIAM Rev., 47(4):629–705, April 2005.
- [63] S. Baboolal. Finite-difference modeling of solitons induced by a density hump in a plasma multi-fluid. Mathematics and Computers in Simulation, 55:309–316, 2001.
- [64] M. Brio and C. C. Wu. An upwind differencing scheme for the equations of ideal magnetohydrodynamics. *Journal of Computational Physics*, 75:400–422, 1988.
- [65] P. A. Amendt, J. L. Milovich, S. C. Wilks, C. K. Li, R. D. Petrasso, and F. H. Séguin. Electric Field and Ionization-Gradient Effects on Inertial-Confinement-Fusion Implosions. *Plasma Phys. Control. Fusion*, 51(124048), 2009.
- [66] H. W. Herrmann, J. R. Langenbrunner, J. M. Mack, J. H. Cooley, D. C. Wilson, S. C. Evans, T. J. Sedillo, G. A. Kyrala, S. E. Caldwell, C. S. Young, A. Nobile, J. Wermer, S. Paglieri, A. M. McEvoy, Y. Kim, S. H. Batha, C. J. Horsfield, D. Drew, W. Garbett, M. Rubery, V. Yu. Glebov, S. Roberts, and J. A. Frenje. Anomalous

- yield reduction in direct-drive deuterium/tritium implosions due to h3e additiona). *Physics of Plasmas*, 16(5), 2009.
- [67] P. Amendt, S. C. Wilks, C. Bellei, C. K. Li, and R. D. Petrasso. The Potential Role of Electric Fields and Plasma Barodiffusion on the Inertial Confinement Fusion Database. *Physics of Plasma*, 18(056308), 2011.
- [68] G. Kagan and X. Z. Tang. Thermo-diffusion in inertially confined plasmas. arXiv:1310.8227v1 [physics.plasm-ph].
- [69] G. Kagan and X. Z. Tang. Electro-diffusion in a plasma with two ion species. *Physics of Plasmas*, 19(082709), 2012.
- [70] C. Bellei, P. A. Amendt, S. C. Wilks, M. G. Haines, D. T. Casey, C. K. Li, R. Petrasso, and D. R. Welch. Species separation in inertial confinement fusion fuels. *Physics of Plasmas*, 20(012701), 2013.
- [71] A. Inglebert, B. Canaud, and O. Larroche. Species separation and modification of neutron diagnostics in inertial-confinement fusion. EPL (Europhysics Letters), 107(6):65003, 2014.
- [72] M. Tatang and G. McRae. Direct treatment of uncertainty in models of reaction and transport. Technical report, MIT Tech. Rep., 1994.
- [73] D. Xiu and J. S. Hesthaven. High order collocation methods for differential equations with random inputs. SIAM J. Sci. Comput., 27(3):1118–1139, 2005.
- [74] E. Novak and K. Ritter. High dimensional integration of smooth funcions over cubes. Numer. Math., 75:79–97, 1996.
- [75] E. Novak and K. Ritter. Simple cubature formulas with high polynomial exactness. Constr. Approx., 15:499–522, 1999.
- [76] V. Barthelmann, E. Novak, and K. Ritter. High dimensional polynomial interpolation on sparse grids. Adv. Comput. Math., 12:273–288, 2000.

- [77] T. Gerstner and M. Griebel. Dimension-adaptive tensor-product quadrature. Computing, 71(1):65–87, 2003.
- [78] B. Ganapathysubramanian and N. Zabaras. Sparse grid collocation schemes for stochastic natural convection problems. J. Comput. Phys., 225(1):652–685, 2007.
- [79] M. Griebel. Adaptive sparse grid multilevel methods for elliptic pdes based on finite differences. Computing, 61(2):151–180, 1998.
- [80] X. Ma and N. Zabaras. An adaptive hierarchical sparse grid collocation algorithm for the solution of stochastic differential equations. J. Comput. Phys., 228(8):3084–3113, 2009.
- [81] G. Lin and G. E. Karniadakis. Sensitivity analysis and stochastic simulations of non-equilibrium plasma flow. Int. J. Numer. Meth. Engng, (80):738–766, March 2009.
- [82] M. A. Shay, J. F. Drake, B. N. Rogers, and R. E. Denton. Alvénic collisionless magnetic reconnection and the hall term. J. Geo. Res., 106(A3):3759–3772, March 2001.
- [83] U. Shumlak and J. Loverich. Approximate Riemann solver for the two-fluid plasma model. J. Comput. Phys., 187:620–638, 2003.
- [84] B. Srinivasan, A. Hakim, and U. Shumlak. Numerical methods for two-fluid dispersive fast MHD phenomena. Comm. Comput. Phys., 9, 2011.
- [85] W. Shin and S. Fan. Choice of the perfectly matched layer boundary condition for frequency-domain maxwells equations solvers. *Journal of Computational Physics*, 231:3406–3431, 2012.
- [86] S. D. Gedney. A anisotropic perfectly matched layer-absorbing for the truncation of FDTD lattices. IEEE transaction on antennas and propagation, 44(12), 1996.
- [87] S. Abarbanel, H. Qasimov, and S. Tsynkov. Long-time performance of unsplit PMLs with explicit second order schemes. *Journal of Scientific Computing*, 41:1–12, 2009.

- [88] E. T. Meier, A. H. Glasser, V. S. Lukin, and U. Shumlak. Modeling open boundaries in dissipative mhd simulation. *Journal of Computational Physics*, (231):2963–2976, 2012.
- [89] C.K. Birdsall and A.B Langdon. *Plasma Physics via Computer Simulation*. CRC Press.
- [90] S. W. Haan. Weakly nonlinear hydrodynamic instabilities in inertial fusion. *Physics of Fluids B: Plasma Physics* (1989-1993), 3(8):2349–2355, 1991.
- [91] Li Wang and Dimitri Mavriplis. Implicit solution of the unsteady euler equations for high-order accurate discontinuous galerkin discretizations. AIAA, (0109), 2006.
- [92] M. Yamada, Y. Ren, H. Ji, J. Breslau, S. Gerhardt, R. Kulsrud, and A. Kuritsyn. Experimental study of two-fluid effects on magnetic reconnection in a laboratory plasma with variable collisionality. *Phys. of Plasmas*, 13(052119), 2006.
- [93] A. Otto. Geospace environment modeling (gem) magnetic reconnection challenge: MHD and Hall MHD - constant and current dependent resitivity models. J. Geo. Res., 106:3751–3757, 2001.
- [94] J. D. Anderson. Computational Fluid Dynamics, The Basics with Applications. McGraw-Hill, 1995.
- [95] G. A. Sod. Survey of several finite difference methods for systems of nonlinear hyperbolic conservation laws. *Journal of Computational Physics*, 26(4), 1978.
- [96] C. Bellei, P. A. Amendt, S. C. Wilks, M. G. Haines, and D. T. Casey et al. Species separation in inertial confinement fusion fuels. *Phys. Plasma*, 20(012701), 2013.
- [97] A. Hakim, J. Loverich, and U. Shumlak. A high resolution wave propagation scheme for ideal two-fluid plasma equations. *Journal of Computational Physics*, 219:418–442, 2006.
- [98] S. Smolyak. Quadrature and interpolation formulas for tensor products of certain classes of functions. *Soviet Math. Dokl.*, 4:240–243, 1963.

- [99] G. Lin and A. M. Tartakovsky. Numerical studies of three-dimensional stochastic Darcy's equation and stochastic advection-diffusion-dispersion equation. J. Sci. Comput., 43(1):92–117, 2010.
- [100] G. Lin and A. M. Tartakovsky. An efficient, high-order probabilistic collocation method on sparse grids for three-dimensional flow and solute transport in randomly heterogeneous porous media. *Advances in Water Resources*, 32(5):712–722, 2009.
- [101] R. Cools. Monomial cubature rules since 'stroud': A compilation. J. Comput. Appl. Math., 48:309–326, 1993.
- [102] R. Cools. Monomial cubature rules since 'stroud': A compilation part 2. J. Comput. Appl. Math., 112:21–27, 1999.
- [103] A. Barth, C. Schwab, and N. Zollinger. Multilevel monte carlo finite element method for elliptic pde's with stochastic coefficients. Technical report, Swiss Federal Institute of Technology Zurich, June 2010. Research Report No. 2010-18.
- [104] W. G. Vincenti and C. H. Kruger. Introduction to Physical Gas Dynamics. Krieger Publishing Company, 2002.

Appendix A

PROBABILISTIC COLLOCATION METHOD

We compare the efficiency of the MMC method with other uncertainty quantification methods. In particular, we compare MMC with MC and PC methods. The general procedure for the PC method is similar to that of the MC method, except that different sampling points and corresponding weights are selected. The procedure consists of three main steps:

- 1. Generate N_c collocation points in a complete probability space, $(\Omega, \mathcal{A}, \mathcal{P})$ based on a quadrature formula based on the distribution of the random parameters (see details in Refs. [101, 102]), where Ω is the event space, $\mathcal{A} \in 2^{\Omega}$ the σ -algebra, and \mathcal{P} the probability measure;
- 2. Solve a deterministic problem at each collocation point;
- 3. Estimate the solution statistics using the corresponding quadrature rule;

$$\mathbb{E}[P(\boldsymbol{x},t)] = \int_{\Gamma} P(\boldsymbol{x},t,\xi)\rho(\xi)d\xi$$

$$\approx \sum_{k=1}^{N_c} P(\boldsymbol{x},t,\xi_k)\rho(\xi_k)w_k, \qquad (A.1)$$

$$V[P](\boldsymbol{x},t) = \int_{\Gamma} (P(\boldsymbol{x},t,\xi) - E[u])^2\rho(\xi)d\xi$$

$$\approx \sum_{k=1}^{N_c} P^2(\boldsymbol{x},t,\xi_k)\rho(\xi)w_k - E[v]^2, \qquad (A.2)$$

where x,t and ξ are the spatial coordinate vector, time and random variable. $\rho(\xi)$ is the probabilistic distribution function (PDF) of random variable ξ , N_c is the number of quadrature points, $\{\xi_k\}$ is the set of quadrature points, and $\{w_k\}$ is the corresponding set of

weights, which are the combination of quadrature weights in each random dimension. In the second step of the PC method approach, as for the MC method, any existing deterministic code can be used. Extensive reviews on the construction of quadrature formulas may be found in Refs. [101, 102]. In this work, the Smolyak formula [98] is used to construct the collocation point set, which is a linear combination of tensor product formulas and has a significantly smaller number of points than the full tensor product set. Recently, high order stochastic collocation methods [73, 100, 99] has been developed based on sparse grids using the Smolyak formula [98]. Such sparse grids do not depend as strongly on the dimensionality of the random space and as such are more suitable for applications with high-dimensional random inputs. Detailed descriptions on building the collocation point set can be found in Refs. [73, 100, 99].

Appendix B

WARPX DESCRIPTION

The simulations in the dissertation were performed using the Washington Approximate Riemann Plasma Solver (WARPX). The code is partial differential equation (PDE) solver, mainly for equations in balance law form as in Eq. (2.39). Fig. (B.1) describes the structure of an input file which can be applied to any PDE system.

Parallelization in done using the Message Passing Interface (MPI) which makes WARPX high performance, scalable, and portable. The Hierarchical Data Format version five (HDF5) library to output the data I/O, which can be done in parallel as well as in series. The output files can have multiple datasets, multidimensional arrays. The Portable Extensible Toolkit for Scientific Computation[61] (PETSc) function can also be called from WARPX. PETSc is PDE equation solver suite that allows for the solution of linear and nonlinear equations and has its own time integrators. PETSc uses MPI and is massively parallel, and has been execute in hundred of thousand of CPUs and GPUs.

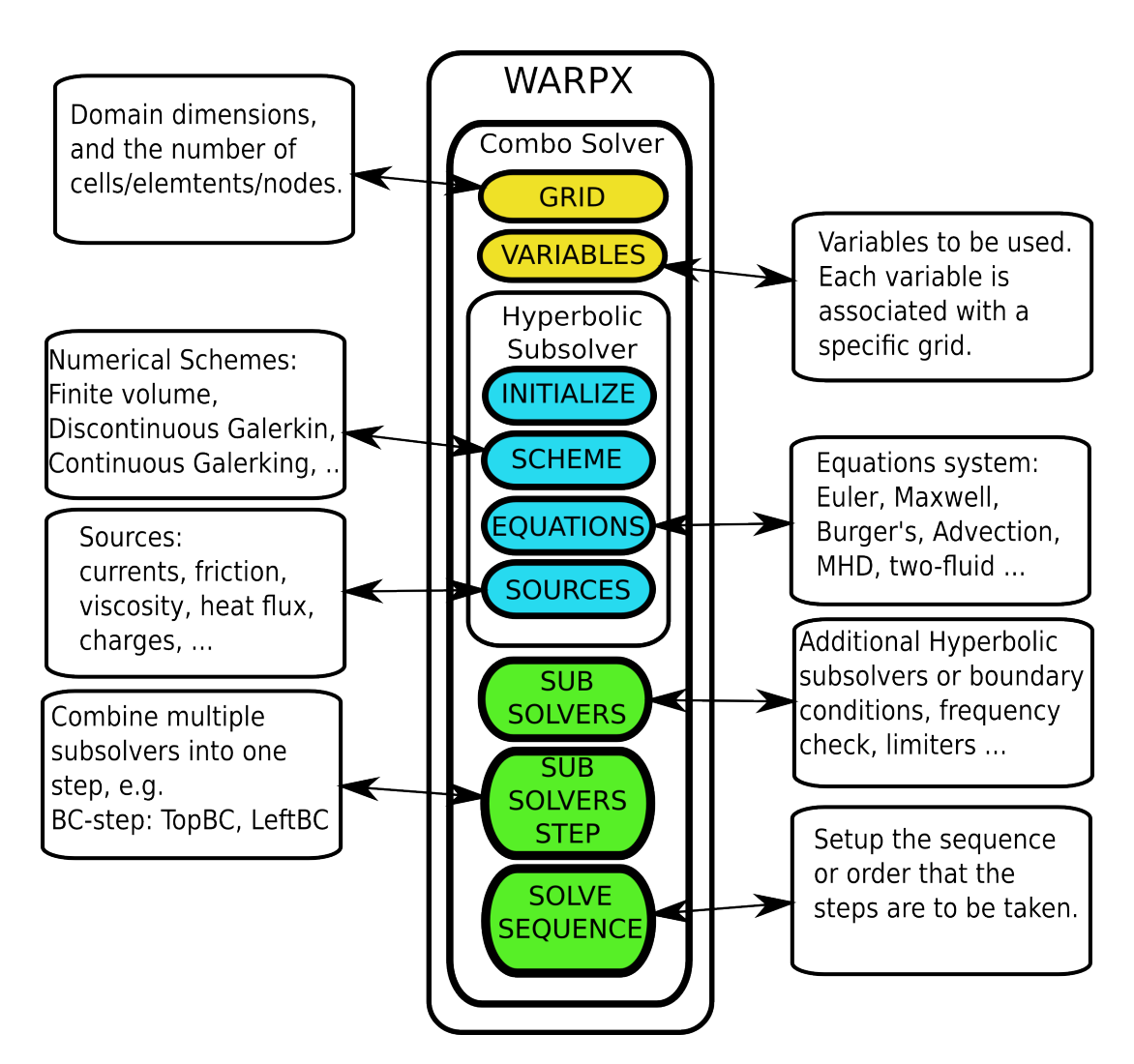


Figure B.1: Structure of a WARPX input file for any PDE type.

Appendix C

SPECIES SEPARATION INPUT FILE

	m
<warpx></warpx>	Type = WxVariable
Simulation = ssbriowu	Kind = parArray
Verbosity = debug	OnGrid = FEMgrid
	NumComponents = 13
<pre><ssbriowu></ssbriowu></pre>	GhostCells = [2, 2]
Type = WxSolver	
Kind = comboSolver	</qemnew>
Time = $[0.0, 0.0013]$	
Out = 500	<qionold></qionold>
Dt = 1.5e - 07	Type = WxVariable
	Kind = parArray
<dggrid></dggrid>	OnGrid = DGgrid
Type = WxGridBox	NumComponents = 20
Lower = [0.0]	GhostCells = [2, 2]
Upper = [0.001]	
Cells = [128]	
	<dqion $>$
	Type = WxVariable
<femgrid></femgrid>	Kind = parArray
Type = WxGridBox	OnGrid = DGgrid
Lower = [0.0]	NumComponents = 20
Upper = [0.001]	GhostCells = [2, 2]
Cells = [257]	
	<d $qion1>$
<qemold></qemold>	Type = WxVariable
Type = WxVariable	Kind = parArray
Kind = parArray	OnGrid = DGgrid
OnGrid = FEMgrid	NumComponents = 20
NumComponents = 13	GhostCells = [2, 2]
GhostCells = [2, 2]	
	<qion1></qion1>
<qemmid></qemmid>	Type = WxVariable
Type = WxVariable	Kind = parArray
Kind = parArray	OnGrid = DGgrid
OnGrid = FEMgrid	NumComponents = 20
NumComponents = 13	GhostCells = [2, 2]
$\frac{1}{2} \text{GhostCells} = \begin{bmatrix} 2 \\ 1 \end{bmatrix}$	[2, 2]
[2, 2]	
	\/ 4.011\/
() domina	<qionnew></qionnew>
<qemnew></qemnew>	Type = WxVariable
\qennew>	Type = wxvariable

```
Kind = parArray
                                                            Type = WxSubSolver
  OnGrid = DGgrid
                                                            Kind = funcDGArraySetter
  NumComponents = 20
                                                            {\tt WriteVars} \; = \; [\; {\tt qionold} \; , \; \; {\tt qionnew} \; ]
  GhostCells = [2, 2]
                                                            OnGrid = DGgrid
                                                            spatialOrder = 2
                                                            mean = 10
</aionnew>
<gtAux>
                                                            <func>
  Type = WxVariable
                                                              Type = WxFunction
  Kind = parArray
                                                              Kind = comboFunc
  OnGrid = DGgrid
                                                              functions = [ion2, ion3]
  NumComponents = 12
  GhostCells = [2, 2]
                                                              <ion2>
                                                                 Kind = eulerShock
</gtAux>
                                                                 sloc = 0.00075
                                                                 gas_gamma = 1.6666666667
<initialcond_elc_max>
                                                                 right = [1.0, 0.0, 0.0, 0.0, 0.5]
  Type = WxSubSolver
                                                                 left = [0.1, 0.0, 0.0, 0.0, 0.005]
  Kind = femArraySetter
  WriteVars = [qemold, qemnew]
                                                              </ion2>
  OnGrid = FEMgrid
  spatialOrder = 2
                                                              <ion3>
  meqn = 13
                                                                 Kind = eulerShock
                                                                 \mathrm{sloc}~=~0.00075
  <func>
                                                                 gas_gamma = 1.6666666667
                                                                 \mathtt{right} \; = \; [\, 1.5 \; , \;\; 0.0 \; , \;\; 0.0 \; , \;\; 0.0 \; , \;\; 0.5 \, ]
    Type = WxFunction
    Kind = comboFunc
                                                                 functions = [elc, maxwell, errPot]
                                                              </ion3>
    <elc>
      Kind = eulerShock
                                                            </func>
       sloc = 0.00075
       gas_gamma = 1.6666666667
                                                          </initialcond_ion>
       \mathtt{right} \, = \, [\, 0.000544 \, , \ 0.0 \, , \ 0.0 \, , \ 0.0 \, , \ 0.033333 ]
       left = [5.4466e-05, 0.0, 0.0, 0.0, 0.0]
                                                          <calcem>
                                                            Type = WxSubSolver
    </elc>
                                                            Kind = fem1dImplicit
                                                            ReadVars = [qemold, qionold]
    <maxwell>
                                                            WriteVars = [qemnew]
                                                            OnGrid = FEMgrid
      Kind = maxwellShock
       sloc = 0.00075
                                                            auxEqnNums = [10]
       left = [0.0, 0.0, 0.0, 0.0, 0.0, 0.0]
                                                            Cfl = 0.5
       right = [0.0, 0.0, 0.0, 0.0, 0.0, 0.0]
                                                            Cflm = 0.5
                                                            spatialOrder = 2
    </maxwell>
                                                            \mathrm{theta} \ = \ 0.5
                                                            Penalty = 10000.0
    <errPot>
                                                            Equations = [eulerElc, maxEqn]
      Kind = constVecFunc
                                                            Sources = [elcCurrents, ionCurrents, ionCurrents3,
       values = [0.0, 0.0]
                                                                       {\tt elcCharge}\;,\;\; {\tt ionCharge}\;,\;\; {\tt ionCharge3}\;,\;\; {\tt lorentzElc}\;,
                                                                       SplEuler, elecDeut, elecTrit]
    </errPot>
                                                            GradientSources = [elecHeatFlux]
                                                            Artificial Dissipation \, = \, [\, Euler dissip \, , \, \, Maxwell dissip \, ]
  </func>
                                                            <eulerElc>
</initialcond_elc_max>
                                                              {\rm Type} \ = \ {\rm WxHyperbolicEqn}
                                                              {\rm Kind} \; = \; {\rm eulerEqn}
<initialcond_ion>
                                                              gas_gamma = 1.6666666667
```

```
c0tov0 = 1120.0
  minPressure = 0.005
                                                            Larmor = 1.0
</eulerElc>
                                                            skin_depth = 0.00537
                                                            Z_alpha = -1.0
<maxEqn>
  {\rm Type} \ = \ {\rm WxHyperbolicEqn}
                                                          </elcCharge>
  Kind = phMaxwellEqn
  c0 = 1.0
                                                          <ionCharge>
  gamma = 0.0
                                                            Type = WxHyperbolicSrc
                                                            Kind = normExtCharges
  chi = 0.0
  normalized = true
                                                            AuxInpRange = [0]
  c0tov0 = 1120.0
                                                            OutRange = [11]
  Larmor = 1.0
                                                            mass = 1.0
                                                            chi = 0.0
  skin_depth = 0.00537
                                                            c0tov0 = 1120.0
</maxEqn>
                                                            Larmor = 1.0
                                                            skin_depth = 0.00537
<elcCurrents>
                                                            Z_alpha = 1.0
  Type = WxHyperbolicSrc
  Kind = currents
                                                          </ionCharge>
  InpRange = [1, 2, 3]
  OutRange = [5, 6, 7]
                                                          <ionCharge3>
  {\rm mass} \, = \, 0.000272331154684
                                                            Type = WxHyperbolicSrc
                                                            Kind = normExtCharges
  charge = -1.0
  epsilon0 = 1.0
                                                            AuxInpRange = [5]
                                                            OutRange \, = \, [\, 1\, 1\, ]
                                                            mass = 1.5
</elcCurrents>
                                                            chi = 0.0
<ionCurrents>
                                                            c0tov0 = 1120.0
  Type = WxHyperbolicSrc
                                                            Larmor = 1.0
  Kind = extCurrents
                                                            skin_depth = 0.00537
                                                            Z_alpha = 1.0
  AuxInpRange = [1, 2, 3]
  OutRange = [5, 6, 7]
  charge = 1.0
                                                          </ionCharge3>
  mass = 1.0
  epsilon0 = 1.0
                                                          <lorentzElc>
                                                            Type = WxHyperbolicSrc
</ionCurrents>
                                                            Kind = normLorentzForces
                                                            InpRange = [0, 1, 2, 3, 5, 6, 7, 8, 9, 10]
<ionCurrents3>
                                                            OutRange = [1, 2, 3, 4]
  Type = WxHyperbolicSrc
                                                            mass = 0.000272331154684
  Kind = extCurrents
                                                            Z_alpha = -1.0
  AuxInpRange = [6, 7, 8]
                                                            CtoV0\_ratio = 1120.0
  OutRange = [5, 6, 7]
                                                            Larmor = 1.0
  charge = 1.0
                                                            Skin\_depth = 0.00537
  {\rm mass} = 1.5
  epsilon0 = 1.0
                                                          </iorCurrents3>
                                                          <Eulerdissip>
                                                            {\tt Type} \, = \, {\tt WxHyperbolicSrc}
<elcCharge>
                                                            {\tt Kind} \; = \; {\tt eulerArtifDiss}
  Type = WxHyperbolicSrc
                                                            InpRange \, = \, [\, 0 \; , \; \ 1 \, , \; \ 2 \, , \; \ 3 \, , \; \ 4 \, ]
  Kind = normCharges
                                                            {\rm OutRange} \, = \, [\, 0 \; , \; \ 1 \, , \; \ 2 \, , \; \ 3 \, , \; \ 4 \, ]
                                                            {\tt dissipation} \ = \ 5\,{\tt e}\,{-}05
  InpRange = [0]
  OutRange = [11]
                                                            gas\_gamma = 1.66666666667
  mass = 0.000272331154684
  chi = 0.0
                                                          </Eulerdissip>
```

<maxwelldissip></maxwelldissip>	<elec $+$ eat $+$ lu $+$
Type = WxHyperbolicSrc	Type = WxHyperbolicSrc
Kind = phMaxwellArtifDiss	Kind = limitedHeatFlux
InpRange = [5, 6, 7, 8, 9, 10, 11, 12]	InpRange = [0, 1, 2, 3, 4]
OutRange = [5, 6, 7, 8, 9, 10, 11, 12]	OutRange = [4]
dissipation = $1e-05$	mass = 0.000272331154684
	gas_gamma = 1.66666666667
	flux_limiter = 0.2
	minPressure = 0.005
<spleuler></spleuler>	minDensity = 4.41176470588e-06
Type = WxHyperbolicSrc	
Kind = eulerSpherical	
InpRange = $[0, 1, 2, 3, 4]$	1,
OutRange = $[0, 1, 2, 3, 4]$	
gas_gamma = 1.6666666667	cy cureemy
88	<calavg></calavg>
	Type = WxSubSolver
(, Spillater)	Kind = linearCombiner
<splmaxwell></splmaxwell>	OnGrid = FEMgrid
Type = WxHyperbolicSrc	ReadVars = [qemold, qemnew]
Kind = phMaxwellNormSpherical	coeffs = [0.5, 0.5]
InpRange = $[5, 6, 7, 8, 9, 10, 11, 12]$	WriteVars = [qemmid]
OutRange = $\begin{bmatrix} 5, 6, 7, 8, 9, 10, 11, 12 \end{bmatrix}$	writevars = [qemmid]
cotivo = $[120.0]$	
Larmor = 1.0	
$skin_depth = 0.00537$	cat Aux gold
skin_depth = 0.00337	<gtaux_qold></gtaux_qold>
	Type = WxSubSolver
	Kind = dgAuxSolver1d
4.1. D. 48	ReadVars = [gtAux, qionold]
<elecdeut></elecdeut>	WriteVars = [gtAux]
Type = WxHyperbolicSrc	OnGrid = DGgrid
Kind = bragFrictionBFEMelec	Cfl = 0.15
InpRange = $[0, 1, 2, 3, 4]$	Cflm = 0.166666666667
AuxInpRange = $[0, 1, 2, 3, 4]$	spatialOrder = 2
OutRange = [1, 2, 3, 4]	auxEqnNums = [10]
mass_e = 0.000272331154684	Equations = [gtAuxEqn]
mass_i = 1.0	4.4A . To . S
Knudsen = 0.0083	<gtauxeqn></gtauxeqn>
gas_gamma = 1.6666666667	Type = WxHyperbolicEqn
ionization = 1	Kind = gradDensTemp
–	gas_gamma = 1.6666666667
	boltz = 1.0
	mi = 1.5
<pre><electrit></electrit></pre>	me = 1.0
Type = WxHyperbolicSrc	elcMinDensity = 0.01
Kind = bragFrictionBFEMelec	ionMinDensity = 0.0093
InpRange = $[0, 1, 2, 3, 4]$	elcMinPressure = 0.0031
AuxInpRange = [5, 6, 7, 8, 9]	ionMinPressure = 0.0031
OutRange = [1, 2, 3, 4]	
$mass_e = 0.000272331154684$	$$
$mass_i = 1.5$	
Knudsen = 0.0083	$$
$gas_gamma = 1.66666666667$	
ionization = 1	<gtaux_limit></gtaux_limit>
	$\mathrm{Type} \; = \; \mathrm{WxSubSolver}$
	Kind = dgLimiter1d

```
{\tt OnGrid} \, = \, {\tt DGgrid}
                                                             <eulerIon2>
  WriteVars = [gtAux]
                                                               {\rm Type} \ = \ {\rm WxHyperbolicEqn}
  spatialOrder = 2
                                                               {\rm Kind} \; = \; {\rm eulerEqn}
  limiter = component
                                                               gas\_gamma = 1.66666666667
                                                               minDensity = 0.01
  {\tt Equations} \; = \; [\, {\tt gtAuxEqn} \, ]
                                                               minPressure = 0.0031
  <gtAuxEan>
    Type = WxHyperbolicEqn
                                                             </eulerIon2>
    Kind = gradDensTemp
    gas_gamma = 1.6666666667
                                                             <eulerIon3>
    boltz = 1.0
                                                               Type = WxHyperbolicEqn
    mi = 1.5
                                                                Kind = eulerEqn
    me = 1.0
                                                               gas_gamma = 1.6666666667
    elcMinDensity = 0.01
                                                                minDensity = 0.0093
    ionMinDensity = 0.0093
                                                                minPressure = 0.0031
    elcMinPressure = 0.0031
    ionMinPressure = 0.0031
                                                             </eulerIon3>
  </gtAuxEqn>
                                                             <lorentzIon2>
                                                               Type = WxHyperbolicSrc
</gtAux_limit>
                                                                Kind = normExtLorentzForces
                                                               InpRange = [0, 1, 2, 3]
<calcionrk1>
                                                                AuxInpRange = [5, 6, 7, 8, 9, 10]
  Type = WxSubSolver
                                                               {\rm OutRange} \ = \ [\, 1 \; , \; \ 2 \; , \; \ 3 \; , \; \ 4 \, ]
  Kind = dgRhsCalc1dWithFem
                                                               mass = 1.0
                                                               Z_alpha = 1.0
  ReadVars = [qionold, qemold, gtAux]
  WriteVars = [dqion]
                                                                CtoV0\_ratio = 1120.0
  OnGrid = DGgrid
                                                               Larmor = 1.0
  auxEqnNums \ = \ [\,1\,3\,]
                                                                Skin\_depth = 0.00537
  auxGradEqnNums = [6]
  Cfl = 0.3
                                                             </lorentzIon2>
  Cflm = 0.3333333333333
  dgSpatialOrder = 2
                                                             <lorentzIon3>
  Equations = [eulerIon2, eulerIon3]
                                                               Type = WxHyperbolicSrc
  Sources = [lorentzIon2, lorentzIon3,
                                                               Kind = normExtLorentzForces
             SplEuler2, SplEuler3,
                                                               InpRange = [5, 6, 7, 8]
              elecDeut, elecTrit, deutTrit]
                                                               AuxInpRange = [5, 6, 7, 8, 9, 10]
  GradientSources = [heatFlux]
                                                               OutRange = [6, 7, 8, 9]
                                                               mass = 1.5
  <SplEuler2>
                                                                Z_alpha = 1.0
    Type = WxHyperbolicSrc
                                                                CtoV0\_ratio = 1120.0
    Kind = eulerSpherical
                                                               Larmor = 1.0
    InpRange = [0, 1, 2, 3, 4]
                                                                Skin\_depth = 0.00537
    OutRange = [0, 1, 2, 3, 4]
    gas_gamma = 1.6666666667
                                                             </SplEuler2>
                                                             <elecDeut>
                                                               {\tt Type} \, = \, {\tt WxHyperbolicSrc}
  <SplEuler3>
                                                               {\tt Kind} \ = \ {\tt bragFrictionBFEMion}
    Type = WxHyperbolicSrc
                                                               InpRange \, = \, [\, 0 \; , \; \ 1 \, , \; \ 2 \, , \; \ 3 \, , \; \ 4 \, ]
    Kind = eulerSpherical
                                                               AuxInpRange \, = \, \begin{bmatrix} 0 \; , \; 1 \; , \; 2 \; , \; 3 \; , \; 4 \end{bmatrix}
    InpRange = [5, 6, 7, 8, 9]
                                                               OutRange = [1, 2, 3, 4]
    OutRange = [5, 6, 7, 8, 9]
                                                               {\tt mass\_e} \ = \ 0.000272331154684
    gas_gamma = 1.6666666667
                                                               mass_i = 1.0
                                                               \rm Knudsen \, = \, 0.0083
  </SplEuler3>
                                                               gas\_gamma = 1.66666666667
                                                                ionization = 1
```

	WriteVars = [gtAux]
	OnGrid = DGgrid
	Cfl = 0.15
<electrit></electrit>	Cflm = 0.166666666667
Type = WxHyperbolicSrc	spatialOrder = 2
Kind = bragFrictionBFEMion	auxEqnNums = [10]
InpRange = [5, 6, 7, 8, 9]	Equations = [gtAuxEqn]
AuxInpRange = [0, 1, 2, 3, 4]	
OutRange = [6, 7, 8, 9]	<gt $AuxEqn>$
${\tt mass_e} \ = \ 0.000272331154684$	$\mathrm{Type} = \mathrm{WxHyperbolicEqn}$
$mass_i = 1.5$	Kind = gradDensTemp
Knudsen = 0.0083	$gas_gamma = 1.66666666667$
$gas_gamma = 1.66666666667$	boltz = 1.0
ionization = 1	mi = 1.5
	me = 1.0
	elcMinDensity = 0.01
	ionMinDensity = 0.0093
<deuttrit></deuttrit>	elcMinPressure = 0.0031
Type = WxHyperbolicSrc	ionMinPressure = 0.0031
Kind = bragFrictionBFEMionIon	
$InpRange = \left[0 \; , \; \; 1 \; , \; \; 2 \; , \; \; 3 \; , \; \; 4 \; , \; \; 5 \; , \; \; 6 \; , \; \; 7 \; , \; \; 8 \; , \; \; 9 \right]$	$$
OutRange = [1, 2, 3, 4, 6, 7, 8, 9]	
$mass_ip = 1.5$	$$
$mass_i = 1.0$	
Knudsen = 0.0107	<calcionrk2></calcionrk2>
$gas_gamma = 1.66666666667$	$\mathrm{Type} \ = \ \mathrm{WxSubSolver}$
ionization = 1	Kind = dgRhsCalc1dWithFem
	ReadVars = [qion1, qemnew, gtAux]
	WriteVars = [dqion1]
	OnGrid = DGgrid
<heatFlux $>$	auxEqnNums = [13]
Type = WxHyperbolicSrc	auxGradEqnNums = [6]
Kind = dgLimitedHeatFlux	Cfl = 0.3
AuxInpRange = [0, 3]	Cflm = 0.33333333333333333333333333333333333
OutRange = [4, 9]	dgSpatialOrder = 2
$mass_i = 1.5$	Equations = [eulerIon2, eulerIon3]
$mass_e = 1.0$	Sources = [lorentzIon2, lorentzIon3, SplEuler2
$flux_limiter = 0.2$	SplEuler3, elecDeut, elecTrit, deutTrit]
	GradientSources = [heatFlux]
	<spleuler2></spleuler2>
/calcionrk1>	Type = WxHyperbolicSrc
	Kind = eulerSpherical
rk_1_ion >	InpRange = [0, 1, 2, 3, 4]
Type = WxSubSolver	OutRange = [0, 1, 2, 3, 4]
Kind = linearCombiner	$gas_gamma = 1.66666666667$
OnGrid = DGgrid	
ReadVars = [qionold, dqion]	
coeffs = [1.0, 1.0]	
WriteVars = [qion1]	<spleuler3></spleuler3>
	Type = WxHyperbolicSrc
/rk_1_ion>	Kind = eulerSpherical
	InpRange = [5, 6, 7, 8, 9]
gtAux_q1>	OutRange = $[5, 6, 7, 8, 9]$
Type = WxSubSolver	$gas_gamma = 1.66666666667$
Kind = dgAuxSolver1d	
ReadVars = [gtAux. gion1]	

```
ionization = 1
<eulerIon2>
  {\rm Type} \ = \ {\rm WxHyperbolicEqn}
                                                     </elecDeut>
  Kind = eulerEqn
  gas\_gamma = 1.66666666667
                                                     <elecTrit>
                                                        Type = WxHyperbolicSrc
  minDensity = 0.01
  minPressure = 0.0031
                                                        Kind = bragFrictionBFEMion
                                                        InpRange = [5, 6, 7, 8, 9]
</eulerIon2>
                                                        AuxInpRange = [0, 1, 2, 3, 4]
                                                        OutRange = [6, 7, 8, 9]
<eulerIon3>
                                                        mass_e = 0.000272331154684
  Type = WxHyperbolicEqn
                                                        mass_i = 1.5
  Kind = eulerEqn
                                                        Knudsen = 0.0083
  gas_gamma = 1.6666666667
                                                        gas_gamma = 1.6666666667
  minDensity = 0.0093
                                                        ionization = 1
  minPressure = 0.0031
                                                      </elecTrit>
</eulerIon3>
                                                     <deutTrit>
<lorentzIon2>
                                                        Type = WxHyperbolicSrc
  Type = WxHyperbolicSrc
                                                        {\bf Kind} \ = \ {\bf bragFrictionBFEMionIon}
  Kind = normExtLorentzForces
                                                        InpRange = [0, 1, 2, 3, 4, 5, 6, 7, 8, 9]
  InpRange = [0, 1, 2, 3]
                                                        OutRange = [1, 2, 3, 4, 6, 7, 8, 9]
  AuxInpRange = [5, 6, 7, 8, 9, 10]
                                                        mass_ip = 1.5
                                                        mass_i = 1.0
  OutRange = [1, 2, 3, 4]
  mass = 1.0
                                                        Knudsen = 0.0107
  Z_alpha = 1.0
                                                        gas gamma = 1.66666666667
  CtoV0\_ratio = 1120.0
                                                        ionization = 1
  Larmor = 1.0
  {\tt Skin\_depth} \,=\, 0.00537
                                                     </deutTrit>
<heatFlux>
                                                        Type = WxHyperbolicSrc
<lorentzIon3>
                                                        Kind = dgLimitedHeatFlux
  Type = WxHyperbolicSrc
                                                        AuxInpRange = [0, 3]
                                                        OutRange = [4, 9]
  Kind = normExtLorentzForces
  InpRange = [5, 6, 7, 8]
                                                        mass_i = 1.5
  AuxInpRange = [5, 6, 7, 8, 9, 10]
                                                        mass_e = 1.0
                                                        flux_limiter = 0.2
  OutRange = [6, 7, 8, 9]
  mass = 1.5
  Z_{alpha} = 1.0
                                                      </heatFlux>
  CtoV0\_ratio = 1120.0
  Larmor = 1.0
                                                    </calcionrk2>
  Skin\_depth = 0.00537
                                                   <rk_2_ion>
Type = WxSubSolver
                                                     Kind = linearCombiner
<elecDeut>
                                                     OnGrid = DGgrid
  Type = WxHyperbolicSrc
                                                     ReadVars = [qionold, qion1, dqion1]
  Kind = bragFrictionBFEMion
                                                     coeffs = [0.5, 0.5, 0.5]
  InpRange = [0, 1, 2, 3, 4]
                                                     WriteVars = [qionnew]
  AuxInpRange = [0, 1, 2, 3, 4]
  OutRange = [1, 2, 3, 4]
                                                    </{
m r}\,{
m k}\,{}_{-}2\,{}_{-}{
m i}\,{
m o}\,{
m n}>
  {\tt mass\_e} \ = \ 0.000272331154684
  mass_i = 1.0
                                                   < anew_limit_ion >
                                                     Type = WxSubSolver
  Knudsen = 0.0083
  gas_gamma = 1.6666666667
                                                     Kind = dgLimiter1d
```

OnGrid = DGgrid	Kind = bcSphericalDGions
WriteVars = [qionnew]	OnGrid = DGgrid
spatialOrder = 2	WriteVars = [qionold]
limiter = component	direction = 0
${\tt Equations} = [{\tt euler2} \; , \; \; {\tt euler3}]$	edge = lower
<euler2></euler2>	
Type = WxHyperbolicEqn	
Kind = eulerLaxEqn	$<$ leftBCq1_ion $>$
$gas_gamma = 1.66666666667$	Type = WxSubSolver
minDensity = 0.01	Kind = bcSphericalDGions
minPressure = 0.0031	OnGrid = DGgrid
	WriteVars = [qion1]
	direction = 0
7. 1. 2S	edge = lower
<pre><euler3> Type = WyHypeyholicFen</euler3></pre>	//left P.Callian
Type = WxHyperbolicEqn Kind = eulerLaxEqn	
gas_gamma = 1.66666666667	<left _ion="" b="" c="" e="" n="" q="" w=""></left>
minDensity = 0.0093	Type = WxSubSolver
minPressure = 0.0033	Kind = bcSphericalDGions
mini lessure = 0.0031	OnGrid = DGgrid
	WriteVars = [qionnew]
(, 64.6.0)	direction = 0
	edge = lower
<q1_limit_ion></q1_limit_ion>	
Type = WxSubSolver	
Kind = dgLimiter1d	<rightbc_ion></rightbc_ion>
OnGrid = DGgrid	Type = WxSubSolver
WriteVars = [qion1]	Kind = bcCopy
spatialOrder = 2	OnGrid = DGgrid
limiter = component	WriteVars = [qionold]
Equations = [euler2, euler3]	direction = 0 edge = upper
<euler2></euler2>	0
Type = WxHyperbolicEqn	
Kind = eulerLaxEqn	
gas_gamma = 1.6666666667	<ri>d t B C q 1 _i o n ></ri>
minDensity = 0.01	Type = WxSubSolver
minPressure = 0.0031	Kind = bcCopy
	OnGrid = DGgrid
	WriteVars = [qion1]
	direction = 0
<euler3></euler3>	edge = upper
Type = WxHyperbolicEqn	
Kind = eulerLaxEqn	$$
$gas_gamma = 1.66666666667$	
minDensity = 0.0093	<rightbcqnew_ion></rightbcqnew_ion>
minPressure = 0.0031	Type = WxSubSolver
./. 1. 0.	Kind = bcCopy
	OnGrid = DGgrid
Z/-1 1::4 :>	WriteVars = [qionnew] direction = 0
	$\begin{array}{l} \text{direction} = 0 \\ \text{edge} = \text{upper} \end{array}$
<leftbc_ion></leftbc_ion>	euge – upper
Type = WxSubSolver	

	edge = lower
$<$ leftBCq1_em $>$	
Type = WxSubSolver	$$
Kind = SphericalCenter	
OnGrid = FEMgrid	<leftbcqnew_em></leftbcqnew_em>
WriteVars = [qemmid]	Type = WxSubSolver
direction = 0	Kind = bcCopy
edge = lower 	OnGrid = FEMgrid
	WriteVars = [qemnew]
	direction = 0
	edge = lower
<leftbcq1_em></leftbcq1_em>	
Type = WxSubSolver	
Kind = bcCopy	
OnGrid = FEMgrid	$<$ rightBCqnew_em $>$
WriteVars = [qemmid]	Type = WxSubSolver
direction = 0	Kind = bcCopy
edge = lower	OnGrid = FEMgrid
	WriteVars = [qemnew]
	direction = 0
	edge = upper
<rightbcq1_em></rightbcq1_em>	
Type = WxSubSolver	
Kind = bcCopy	
OnGrid = FEMgrid	$<$ leftBCqold_em $>$
WriteVars = [qemmid]	Type = WxSubSolver
direction = 0	Kind = SphericalCenter
edge = upper	OnGrid = FEMgrid
	WriteVars = [qemold]
	direction = 0
	edge = lower
<leftbc_gtaux></leftbc_gtaux>	
Type = WxSubSolver	$$
Kind = bcCopy	
OnGrid = DGgrid	<rightbcqold_em></rightbcqold_em>
WriteVars = [gtAux]	Type = WxSubSolver
direction = 0	Kind = bcCopy
edge = lower	OnGrid = FEMgrid
	WriteVars = [qemold]
	direction = 0
	edge = upper
<rightbc_gtaux></rightbc_gtaux>	
Type = WxSubSolver	
Kind = bcCopy	
OnGrid = DGgrid	<copier_em></copier_em>
WriteVars = [gtAux]	Type = WxSubSolver
direction = 0	Kind = linearCombiner
edge = upper	OnGrid = FEMgrid
	ReadVars = [qemnew]
$$	coeffs = [1.0]
	WriteVars = [qemold]
<leftbcqnew_em></leftbcqnew_em>	
Type = WxSubSolver	
Kind = SphericalCenter	
OnGrid = FEMgrid	<pre><copier_ion></copier_ion></pre>
WriteVars = [qemnew]	Type = WxSubSolver
direction = 0	Kind = linearCombiner

```
OnGrid = DGgrid
  ReadVars = [qionnew]
                                                                <\!\operatorname{grad} T \operatorname{\_stage} 1\!>
  coeffs = [1.0]
                                                                   {\tt Type} \; = \; {\tt WxSubSolverStep}
  {\tt WriteVars} \, = \, [\, {\tt qionold} \, ]
                                                                   {\tt SubSolvers} \, = \, [\, {\tt gtAux\_qold} \, , \, \, {\tt gtAux\_limit} \, ]
                                                                   SyncVars = [gtAux]
                                                                   DtFrac = 1.0
</copier_ion>
< c h k _ freq >
                                                                 </gradT_stage1>
  Type = WxSubSolver
                                                                 <ionRK1>
  Kind = checkFreqTimeStepMixedFemDg
                                                                   Type = WxSubSolverStep
  charge = 1.0
  ionmass = 1.0
                                                                   SubSolvers \, = \, [\, calcionrk1 \,\, , \,\, rk\_1\_ion \,\, , \,\, q1\_limit\_ion \,]
  \mathtt{elcmass} \; = \; 0.000272331154684
                                                                   DtFrac = 1.0
  epsilon0 = 1e-07
  spatialOrder = 2
                                                                 </ionRK1>
  OnGrid = FEMgrid
  ReadVars = [qemold, qionold]
                                                                 <emRK1>
                                                                   Type = WxSubSolverStep
</chk_freq>
                                                                   SubSolvers = [calcem, calAvg]
                                                                   DtFrac = 1.0
<nancheckem>
  Type = WxSubSolver
                                                                 </emRK1>
  Kind = isNANCheck
  OnGrid = FEMgrid
                                                                 <gradT_stage2>
  {\tt ReadVars} \ = \ [\, {\tt qemnew} \, ]
                                                                   {\tt Type} \; = \; {\tt WxSubSolverStep}
                                                                   {\tt SubSolvers} \; = \; [\; {\tt gtAux\_q1} \; , \;\; {\tt gtAux\_limit} \; ]
</nancheckem>
                                                                   SyncVars = [gtAux]
                                                                   DtFrac = 1.0
<nancheckq1>
  Type = WxSubSolver
                                                                 </gradT_stage2>
  Kind = isNANCheck
  OnGrid = DGgrid
                                                                 <ionRK2>
  ReadVars = [dqion]
                                                                   {\tt Type} \ = \ {\tt WxSubSolverStep}
                                                                   {\tt SubSolvers} \ = \ [\ {\tt calcionrk2}\ , \ \ {\tt rk-2\_ion}\ , \ \ {\tt qnew\_limit\_ion}\ ]
                                                                   DtFrac = 1.0
</nancheckq1>
<isNANq1>
                                                                 </ionRK2>
  Type = WxSubSolverStep
  SubSolvers = [nancheckq1]
                                                                 <emRK2>
  DtFrac = 1.0
                                                                   Type = WxSubSolverStep
                                                                   SubSolvers = [calcemrk2, rk_2_em]
</isNANq1>
                                                                   DtFrac = 1.0
\langle isNANqem \rangle
                                                                 </emRK2>
  {\tt Type} \, = \, {\tt WxSubSolverStep}
  SubSolvers = [nancheckem]
                                                                 <applyBC_ion>
  DtFrac = 1.0
                                                                   Type = WxSubSolverStep
                                                                   SubSolvers = [leftBC\_ion, rightBC\_ion]
</isNANqem>
                                                                   DtFrac = 1.0
<i n i t Arrays>
                                                                 </\operatorname{applyBC\_ion}>
  Type = WxSubSolverStep
  SubSolvers = [initialcond\_elc\_max,
                                                                 <applyBCq1_ion>
                                                                   {\tt Type} \ = \ {\tt WxSubSolverStep}
                                   initialcond_ion]
  DtFrac = 1.0
                                                                   SubSolvers \, = \, [\, leftBCq1\_ion \, , \, \, rightBCq1\_ion \, ]
                                                                   DtFrac = 1.0
</initArrays>
```

```
</applyBCq1_ion>
                                                                <copy>
<\!{\rm applyBCq1\_em}\!>
                                                                   {\tt Type} \ = \ {\tt WxSubSolverStep}
  {\tt Type} \ = \ {\tt WxSubSolverStep}
                                                                   {\tt SubSolvers} \, = \, [\, {\tt copier\_em} \, \, , \, \, \, {\tt copier\_ion} \, ]
  {\tt SubSolvers} \; = \; [\, {\tt leftBCq1\_em} \; , \; \; {\tt rightBCq1\_em} \, ]
                                                                   {\tt SyncVars} \; = \; [\, {\tt qemold} \; , \; \; {\tt qionold} \, ]
                                                                   DtFrac = 1.0
  {\tt DtFrac} \, = \, 1.0
</applyBCq1_em>
                                                                </copy>
<applyBCqnew_ion>
                                                                <chkFreqDt>
  Type = WxSubSolverStep
                                                                   Type = WxSubSolverStep
  SubSolvers = [leftBCqnew_ion, rightBCqnew_ion]
                                                                   SubSolvers = [chk\_freq]
                                                                   DtFrac = 1.0
  DtFrac = 1.0
</applyBCqnew_ion>
                                                                </chkFreqDt>
<applyBCqnew_em>
                                                                <SolverSequence>
  Type = WxSubSolverStep
                                                                   Type = WxSolverSequence
  SubSolvers = [leftBCqnew_em, rightBCqnew_em,
                                                                   StartOnly = [initArrays, applyBC_ion, applyBCq1_em]
              leftBCqold_em , rightBCqold_em]
                                                                   PerStep = [chkFreqDt, gradT_stage1, applyBCgt, emRK1,
  DtFrac = 1.0
                                                                      applyBCqnew_em, ionRK1, applyBCq1_ion,
                                                                      gradT_stage2, applyBCgt, ionRK2,
</applyBCqnew_em>
                                                                      {\tt applyBCqnew\_ion}\;,\;\;{\tt copy}\;]
<applyBCgt>
                                                                 </SolverSequence>
  {\tt Type} \; = \; {\tt WxSubSolverStep}
  SubSolvers \, = \, \left[ \, leftBC\_gtAux \, , \, \, rightBC\_gtAux \, \right]
                                                              </ssbriowu>
  DtFrac = 1.0
                                                           </warpx>
</applyBCgt>
```

VITA

Éder grew up in the Mindelo, Cabo Verde island in the west coast of Africa before moving to Boston in 2001. He earned his B.S. and Masters degree in Aerospace engineering at Embry-Riddle Aeronautical University in Daytona Beach, FL and PhD in Aerospace and Energetics at the University of Washington in Seattle, WA. He currently works as an ERC, Inc contractor for the Air Force Research Lab at Edwards Air Force Base. While in graduate school he played volleyball way too much, basketball not enough, and canoed just about the right amount at UW's WAC.